# Thermal and photoinduced transport in 2D materials

Thermischer und fotoinduzierter Transport in 2D Materialen


DISSERTATION ZUR ERLANGUNG DES DOKTORGRADES DER NATURWISSEN-
SCHAFTEN (DR. RER. NAT.) DER FAKULTÄT FÜR PHYSIK

DER UNIVERSITÄT REGENSBURG

vorgelegt von

Sofia Blanter aus

Moskau, Russland

im Jahr 2020

Auf der Innenseite des Titelblattes:

Promotionsgesuch eingereicht am:
Die Arbeit wurde angeleitet von: Prof. Dr. Christoph Strunk

Prüfungsausschuss:

Vorsitzender: Prof. Dr. Jaroslav Fabian

1. Gutachter: Prof. Dr. Christoph Strunk
2. Gutachter: Prof. Dr. Jascha Repp

Weitere Prüfer: Prof. Dr. Sergey Ganichev

Datum Promotionskolloquium: 09-06-2020

UNIVERSITY OF REGENSBURG

# *Abstract*

Faculty of Physics
Department of Experimental Physics

Doctor of Philosophy

**Thermal and photoinduced transport in 2D materials**

by Sofia BLANTER

The discovery of graphene has opened a new field of 2D materials. Those layered materials can be easily exfoliated down to a few-layer form and show remarkable physical properties, not present in their bulk counterpart. Yet many of them are still uncharacterised, despite the growing need for novel materials in the modern small-size electronic devices.

In this thesis we characterise the optoelectronic properties of a few-layer $In_2Se_3$ bases phototransducer. We study the current in dark and under illumination and determine the dominant photocurrent generating mechanism at different gate voltages. We find that this mechanism can be tuned: from the photoconduction in the OFF state to the photogating in the ON state. We measure a responsivity of 100 A/W in the ON state at a small bias voltage of 50 mV, and a detectivity of $3{\cdot}10^{13}$ Jones. Those high values make $In_2Se_3$ a good candidate for future optoelectronic applications.

We also characterise the thermal properties of four few-layer suspended h-BN flakes. We introduce a new method for measuring the thermal properties of the 2D materials by modifying the $3\omega$ method and adding a thermometer at the edge of the suspended flake. We measure the thermal conductivity and the thermal diffusivity of h-BN independently. We obtain values of thermal conductivity in the order of 100 $W\ m^{-1}\ K^{-1}$, which is in agreement with the literature. We calculate the phonon mean free path to be 80 nm for 50 K and 8.5 nm for 250 K, and find that its temperature dependence is dominated by the umklapp scattering mechanism. We confirm our findings with a 2D COMSOL simulation at zero frequency. We use the high-frequency part (200 Hz < f < 1000 Hz) of our phase shift curves to calculate the thermal diffusivity values of our samples. We obtain values of thermal diffusivity of 1 $mm^2/s$, which is three to four orders lower than the literature values. We can only partly reproduce our phase shift measurements with a 1D diffusion model, which suggests that we are observing a different type of thermal transport than purely diffusive in our phase shift measurements.

Die Entdeckung von Graphen hat ein neues Feld von 2D-Materialien eröffnet. Diese Schichtmaterialien lassen sich leicht bis auf wenige Schichten abblättern und weisen bemerkenswerte physikalische Eigenschaften auf, die bei ihrem 3D-Pendant nicht vorhanden sind. Dennoch sind viele von ihnen noch immer nicht charakterisiert, trotz des wachsenden Bedarfs an neuartigen Materialien in den modernen elektronischen Kleingeräten.

In dieser Arbeit charakterisieren wir die optoelektronischen Eigenschaften eines mehrschichtigen $In_2Se_3$-Basis-Photowandlers. Wir untersuchen den Strom im Dunkeln und unter Beleuchtung und bestimmen den dominanten Erzeugungsmechanismus des Photostroms bei verschiedenen Gatterspannungen. Wir stellen fest, dass dieser Mechanismus abstimmbar ist: von der Photoleitung im AUS-Zustand bis zum Photogating im EIN-Zustand. Wir messen eine Empfindlichkeit von 100 A/W im EIN-Zustand bei einer kleinen Vorspannung von 50 mV und einer Detektivität von $3{\cdot}10^{13}$ Jones. Diese hohen Werte machen $In_2Se_3$ zu einem guten Kandidaten für zukünftige optoelektronische Anwendungen.

Wir charakterisieren auch die thermischen Eigenschaften von vier dünnschichtig aufgehängten h-BN-Flocken. Wir führen eine neue Methode zur Messung der thermischen Eigenschaften der 2D-Materialien ein, indem wir die 3ω-Methode modifizieren und ein Thermometer am Rand der aufgehängten Flocke hinzufügen. Wir messen die Wärmeleitfähigkeit und das thermische Diffusionsvermögen von h-BN unabhängig voneinander. Wir erhalten Werte der Wärmeleitfähigkeit in der Größenordnung von 100 $W\ m^{-1}\ K^{-1}$, was mit der Literatur übereinstimmt. Wir berechnen die mittlere freie Weglänge der Phononen für 50 K auf 80 nm und für 250 K auf 8,5 nm und stellen fest, dass die Temperaturabhängigkeit von h-BN durch den Mechanismus der Umklapp-Streuung dominiert wird. Wir bestätigen unsere Ergebnisse mit einer 2D-COMSOL-Simulation bei Nullfrequenz. Wir verwenden den Hochfrequenzteil ($200\ Hz < f < 1000\ Hz$) unserer Phasenverschiebungskurven, um die Temperaturleitfähigkeitswerte unserer Proben zu berechnen. Wir erhalten Wärmediffusionsvermögenswerte von 1 $mm^2/s$, die um drei bis vier Ordnungen niedriger sind als die Literaturwerte. Wir können unsere Phasenverschiebungsmessungen nur teilweise mit einem 1D-Diffusionsmodell reproduzieren, was darauf hindeutet, dass wir bei unseren Phasenverschiebungsmessungen eine andere Art des Wärmetransports beobachten als einen rein diffusiven.

# *Acknowledgements*

I would like to thank the following people for the enourmous help and support during my PhD:

My supervisor Christoph Strunk for the opportunity to carry out my PhD in his group and to work on the complicated topic of thermal transport. But also for his continuous guidance, mentorship, motivation to dig deeper and to not give up and the infinite amount of patience.

Nicola Paradiso for the many fruitful discussions and the needed amount of humour to handle the most depressing moments in my PhD, when everything would break or stop working. A significant fabrication bug would not be solved without Nicola's help, and many times his practical knowledge and advice helped me out with most obscure fabrication and measurement artefacts.

Christian Bäuml for being the truest friend and helping me out in most stupid of problems, like babysitting during bonding sessions (because the bonder was systematically allergic to me, breaking down every single time) and carrying the heavy transfer line to the workshop. As the officially "most trained person", Christian helped me many times to handle the flow cryostat, whenever I was building in another most-likely-not-to-work sample or changing the helium can. And as "the king of the office" he was responsible for all the office events, including pancake eating sessions and the one very forgotten poker game.

Sasmita Srichandan, for being there every time I had to talk through any of my frustrations with the progress or fabrication. For showing me most of the clean room tricks for the fabrication and leading the way at the beginning of my PhD.

Denis Kochan, for being very patient with us and our ever non-confirming data. For learning COMSOL specifically for our data and for developing the theoretical models to explain our measurements.

David Disterheft for multiple times when he helped me out with the new bonder and the tilted SEM holder in the Auriga. And for passing by my office when I needed cheering up after another day full of breaking devices.

Claudia Moser and Elke Haushalter for helping out with all the bureaucratic questions, whenever I had them and clearing up many misunderstandings I had with the official letters due to language problems.

Andreas Eller, Julian Heger, Simon Reinhardt, Lorenz Bauriedl and Alexander Weitzel for being wonderful office mates and creating a nice and friendly atmosphere.

Alexey Chernikov and Andreas Hüttel for many fruitful discussions and the very healthy amount of humour that always cheered me up whenever we talked.

Tobias Korn for providing the needed help with building the 2D setup, for the inside-info on the exfoliation techniques from his group and the occasionally borrowed 2D material crystals.

Olivier Bourgeois for the very fruitful visit to Grenoble and the help with the $3\omega$ method and its practical limitations.

Dieter Riedl, Josef Haberkorn and Maik Weyer from the electronic workshop for all the help with building my complicated setup, its sample holders and grounding cables. For being friendly and helpful every time I would come with my questions and broken instruments.

The rest of the Strunk research group for the wonderful atmosphere and always being ready to help or explain something when I needed it.

And finally my friends and family for the continuous support during those hard times, when I was close to the breaking point, every time I came home and found people still rooting for me and believing in me.

# Contents

# List of Figures

# List of Tables

# List of Abbreviations

| | |
|---|---|
| **AFM** | Atomic Force Microscope |
| **ADC** | Analog to Digital Converter |
| **BNC** | Bayonet Neill-Concelman connector |
| **DAC** | Digital to Analog Converter |
| **h-BN** | Hexagonal Boron Nitride |
| **IVC** | Inner Vacuum Chamber |
| **MIBK** | Methyl Isobutyl Ketone |
| **PDMS** | Polydimethylsiloxane |
| **PMMA** | Poly(methyl methacrylate) |
| **RIE** | Reactive Ion Etching |
| **RMS** | Root Mean Square |
| **SEM** | Scanning Electron Microscope |
| **TMDC** | Transition Metal Dichalcogenide |

# List of Symbols

**$In_2Se_3$ phototransistors**

| | |
|---|---|
| $A$ | absorbtion |
| $A_{device}$ | surface area of the device |
| $A_{laserspot}$ | surface area of the laserspot |
| $B$ | bandwidth |
| $C$ | capacitance to the backgate per unit area |
| $C_{ox}$ | parallel plate capacitance to the gate |
| $d$ | thickness of the measured material |
| $D$ | absorbtion depth |
| $D^*$ | detectivity |
| $E$ | energy |
| $E_f$ | electrical field in the channel |
| $g$ | transconductance |
| $I$ | electrical current |
| $I_{dark}$ | electrical current in the dark |
| $I_{light}$ | electrical current under illumination |
| $I_{PC}$ | current induced by the photoconductive effect |
| $I_{ph}$ | photocurrent |
| $I_{PV}$ | current induced by the photogating effect |
| $L$ | channel length |
| $n$ | excess carrier density |
| $P_{eff}$ | effective laser power |
| $P_{in}$ | incoming laser power |
| $q$ | charge per particle |
| $R$ | responsivity |
| $R_c$ | contact resistance |
| $R_{tot}$ | total measured resistance |
| $S$ | Seebeck coefficient |
| $\Delta T$ | temperature increase caused by the laser |
| $t_{resp}$ | rise and fall response time |
| $\Delta V$ | induced voltage difference due to Seebeck effect |
| $V_b$ | bias voltage |
| $V_g$ | gate voltage |
| $V_t$ | threshold voltage |
| $\Delta V_t$ | gate voltage difference due to trapped charges |
| $W$ | channel width |
| | |
| $\alpha$ | exponent of the correlation between $I_{ph}$ and $P_{eff}$ |
| $\lambda$ | laser wavelength |
| $\mu$ | carrier mobility |

**Thermal transport in suspended h-BN**

| | |
|---|---|
| $A$ | cross section area of the heater |
| $a_{hBN}$ | h-BN atomic spacing |
| $b_{flake}$ | width of the flake |
| $b_h$ | width of the heater |
| $b_{hBN}$ | width of the suspended h-BN |
| $b_{mem}$ | width of the membrane |
| $c_h$ | specific heat per mass of the heater |
| $C'_h$ | heat capacity of the heater |
| $c_{hBN}$ | specific heat per mass of the h-BN |
| $c_{mem}$ | specific heat per mass of the membrane |
| $C'_{st}$ | heat capacity of the strip below the heater |
| $c_p$ | specific heat per mass |
| $c_v$ | specific heat per volume |
| $D$ | thermal diffusivity |
| $D_{1Dmodel}$ | thermal diffusivity obtained from 1D model |
| $D_{hBN}$ | thermal diffusivity of the h-BN |
| $D_{region}$ | thermal diffusivity of the region between heater and second thermometer |
| $f$ | frequency |
| $G_{kink}$ | thermal conductance of the flake kink |
| $h$ | Planck's constant |
| $\hbar$ | reduced Planck's constant |
| $I_h$ | electrical current through the heater |
| $I_t$ | electrical current through the thermometer |
| $I_{th}$ | thermal current |
| $k$ | wave number |
| $k_B$ | Boltzmann constant |
| $K_{mem}$ | thermal conductance of membrane |
| $K_{th}$ | thermal conductance of the sample |
| $L_1$ | distance between heater and thermometer |
| $L_2$ | distance between thermometer and the edge of the $Si_3N_4$ membrane |
| $l_{flake}$ | length of the flake |
| $l_h$ | length of the heater |
| $l_{hBN}$ | length of the suspended h-BN |
| $l_{mat}$ | length of the material |
| $l_{mem}$ | length of the membrane |
| $L_{th}$ | thermal penetration depth |
| $N_{heater}$ | amount of atoms in the heater |
| $P$ | power |
| $P_h$ | power applied to the heater |
| $P_{hBN}$ | power applied to the suspended h-BN |
| $Pr_{slit}$ | perimeter of the slit |
| $\vec{q}$ | energy current density |
| $R_0$ | resistance of the heater in the non-heated state |
| $R_1$, $R_2$, $R_3$, $R_4$ | constant resistances in the Wheatstone bridges |
| $\Delta R_{av}$ | heater resistance increase due to Joule heating |
| $R_c$ | thermal contact resistance |
| $R_c^*$ | estimated thermal contact resistance from $R_{th,fit}$ |

| | |
|---|---|
| $R_h$ | electrical resistance of the heater |
| $\Delta R_h$ | time-dependent heater resistance increase |
| $R_{pre}$ | pre-resistor |
| $R_{sheet}$ | electrical sheet resistance |
| $R_{strip}$ | electrical resistance of heater/thermometer |
| $R_t$ | electrical resistance of the thermometer |
| $R_{t0}$ | electrical resistance of the thermometer in the non-heated state |
| $\Delta R_t$ | time-dependent thermometer resistance increase |
| $\Delta R_{t,av}$ | thermometer resistance increase due to Joule heating |
| $R_{th}$ | thermal resistance of the sample |
| $R_{th,fit}$ | linear approximation of sample thermal resistance |
| $R_{th,hBN}$ | thermal resistance of the suspended h-BN |
| $R_{v1}, R_{v2}$ | variable resistances in the Wheatstone bridges |
| $R_x$ | sample resistance in the Wheatstone bridge |
| $s_0$ | square root coefficient from low-frequency $\Delta\phi$ |
| $t$ | time |
| $T$ | temperature |
| $\mathcal{T}$ | transmission probability |
| $t_0$ | average time for the temperature increase to travel from heater to thermometer |
| $T_0$ | umklapp temperature limit |
| $t_{Au}$ | thickness gold |
| $\Delta T_{av}$ | temperature increase due to Joule heating |
| $T_{bath}$ | bath temperature |
| $T_{cold}$ | temperature at the cold end |
| $T_D$ | Debye temperature |
| $T_{D,Au}$ | Debye temperature gold |
| $T_{D,h}$ | Debye temperature of the heater |
| $T_{D,Ti}$ | Debye temperature titanium |
| $t_{flake}$ | thickness of the flake |
| $\Delta T_h$ | temperature increase at the heater |
| $\Delta T_{h-t}$ | temperature drop between heater and thermometer |
| $T_{hot}$ | temperature at the hot end |
| $t_i$ | thickness of the $i^{th}$ material |
| $t_{mat}$ | thickness of the material |
| $t_{mem}$ | thickness of the membrane |
| $t_{ab}$ | thickness absorbates layer |
| $\Delta T_{Rc}$ | temperature increase due to $R_c$ |
| $t_{SiN}$ | thickness of the $Si_3N_4$ membrane |
| $\Delta T_{th}$ | temperature increase at the thermometer |
| $t_{Ti}$ | thickness titanium |
| $u$ | speed of sound |
| $u_h$ | speed of sound of the heater |
| $u_{hBN}$ | speed of sound of the h-BN |
| $V_\omega$ | $1\omega$ component of $V_h$ |
| $V_{3\omega}$ | $3\omega$ component of $V_h$ |
| $v_{eff}$ | effective speed of the phonons |
| $V_h$ | voltage drop over the heater |
| $V_{heater}$ | volume of the heater |

| | |
|---|---|
| $v_p(k)$ | phonon group velocity |
| $V_s$ | source voltage |
| $V_t$ | voltage drop over the thermometer |
| $V_{t,2\omega}$ | $2\omega$ component of $V_t$ |
| $W_1, W_2$ | Wheatstone voltages |
| $W_{3\omega}$ | $3\omega$ component of the Wheatstone voltage |
| | |
| $\alpha_x$ | absolute statistical error of x |
| $\beta_x$ | absolute systematic error of x |
| $\epsilon$ | phonon energy |
| $\epsilon_x$ | absolute error of x |
| $\eta$ | power input per volume |
| $\kappa_i$ | thermal sheet conductance of $i^{th}$ material |
| $\lambda$ | thermal conductivity |
| $\lambda_i$ | thermal conductivity of the $i^{th}$ material |
| $\lambda_{bilayer}$ | thermal conductivity of the bilayer |
| $\lambda_{eff}$ | effective thermal conductivity used in COMSOL simulation |
| $\lambda_{flake}$ | thermal conductivity of the flake |
| $\lambda_{hBN}$ | thermal conductivity of the h-BN |
| $\lambda^*_{hBN}$ | estimated thermal conductivity from the linear approximation of $R_{th}$ |
| $\lambda_{mat}$ | thermal conductivity of the material |
| $\lambda_{mem}$ | thermal conductivity of the membrane |
| $\Lambda_{ph}$ | phonon mean free path |
| $\lambda_{SiN,fit}$ | thermal conductivity $\lambda_{SiN}$ obtained from 1D diffusion model |
| $\rho$ | mass density |
| $\rho_h$ | mass density of the heater |
| $\rho_{hBN}$ | mass density of the h-BN |
| $\rho_{mem}$ | mass density of the membrane |
| $\tau$ | thermal RC-time |
| $\tau_0$ | scattering time |
| $\tau_D$ | diffusion time |
| $\tau_{kink}$ | thermal RC-time of the flake kink |
| $\tau_{R_c}$ | thermal RC-time of the $R_c$ |
| $\tau_{th}$ | thermal cut-off time |
| $\Delta\phi$ | phase shift between the heater and the thermometer |
| $\omega$ | angular frequency |
| $\omega_p$ | phonon frequency |

*Dedicated to my family*

# Chapter 1

# Motivation

The size of our electronics is getting smaller as we are improving and scaling down the electrical components. Already in 1965 Moore predicted that the increase in component density and performance would double with every year [1]. In 1975 this emperical law was changed to doubling every two years [2], and so far Moore's law has remained valid: the size of a transistor was reduced from 10 µm to 30 nm in the past 40 years [3]. Yet we seem to be hitting the limits with the traditional silicon-based devices and to keep scaling down one needs to employ different, novel materials.

With the discovery of graphene [4,5] a new field of 2D materials has been created. Those layered materials have strong covalent in-plane bonding within the layers, but are hold together by weak van der Waals forces between those layers, making it easy to isolate sheets of only few atoms thick. Not only does their reduced size make them a good candidate for novel flat electronic devices, they also show remarkable properties, not present in their bulk counterpart [6–20].

There have been many experimental studies on optoelectronic properties of different 2D materials [6,13,14], searching for new alternatives for solar cells and more effective energy harvesting devices. Multiple studies have shown systematically better optical responsitivities than the traditional silicon-based devices [21–31], but many 2D materials are still uncharacterized as possible building blocks for optoelectronic devices. In Chapter 3 we characterize one of those new materials, $In_2Se_3$, measuring its optical and electronic properties and comparing our findings to other 2D materials in literature. We investigate the dominant photogeneration mechanism in $In_2Se_3$ and study how it changes with the gate voltage.

Significantly fewer experimental studies [32–36] have been dedicated to thermal properties of the 2D materials, despite the increasing need for cooling and handling of the heat generated in the small devices. Moreover, the currently employed thermal measuring techniques either cannot be easily used to measure the 2D materials due to size restrictions, or have significant limitations [37–40]. In Chapter 4 we introduce a new thermal measurement technique and use it to investigate the thermal properties of few-layer h-BN. We do a systematic study by varying the length and thickness of our samples and observe how the thermal properties vary with those parameters.

# Chapter 2

# Stamping technique

This chapter describes the experimental stamping technique that is used for all of our devices in further chapters. The method was first introduced by Castellanos-Gomez et al. [41] and allows to deterministically transfer a 2D material flake onto a specific spot on the substrate. Since it is a dry technique, it also avoids any PMMA residues or contamination due to use of liquid chemicals. This section describes each step of the exfoliation and stamping process in detail.

## 2.1 Exfoliation

To isolate our two-dimensional flake from the bulk we use adhesive tape and exfoliate the material from the bulk crystal onto a thin viscoelastic stamp. The stamp is made from PDMS, we use a commercially available version: Gel-Film WF 6.0 mil × 4 films.

### 2.1.1 Exfoliating the material onto adhesive tape

In this process we use two types of adhesive tape. First we use white tape to peel off some of the material from the original crystal. This type of tape is more sticky and allows us to break the original crystal into smaller parts. Then we transfer the contents of the white tape onto a blue tape, which is less adhesive. This is to make sure the newly exfoliated flakes will not be contaminated by the glue. If needed, one can repeat the process, by transferring the material onto another blue tape. This can be done several times. Finally we again exfoliate, this time from the blue tape onto a PDMS stamp.

Using optical microscopy we can determine the approximate thickness of the flakes on the tape by optical contrast. The thinner the flake, the more transparent it will be. Generally, by increasing the amount of exfoliations one can reduce the average thickness, but will also reduce the average size of the flake. Those parameters might also depend on the speed of the peeling and the amount of times the tape has been re-used.

### 2.1.2 Exfoliating the flake onto the viscoelastic stamp

Once we have optimized the exfoliation process, we can transfer the material from our last blue tape onto the PDMS stamp. For our purposes a stamp of approximately 1 by 1 cm yields the best results. If one increases the size, the stamp tends to form bubbles due to the dust between the stamp and the glass, which causes problems during stamping (see Section 2.2). If one uses a smaller size, the probability of finding the right flake will decrease, since less material will fit onto the stamp surface.

In Figure 2.1 one can see the overview of the transfer process. One puts the blue tape on top of the PDMS and then retracts it, leaving some of the materials behind. By varying the speed with which one peels off the tape and the contact time between the tape and the stamp, one can influence the amount and the size of the transfered flakes.

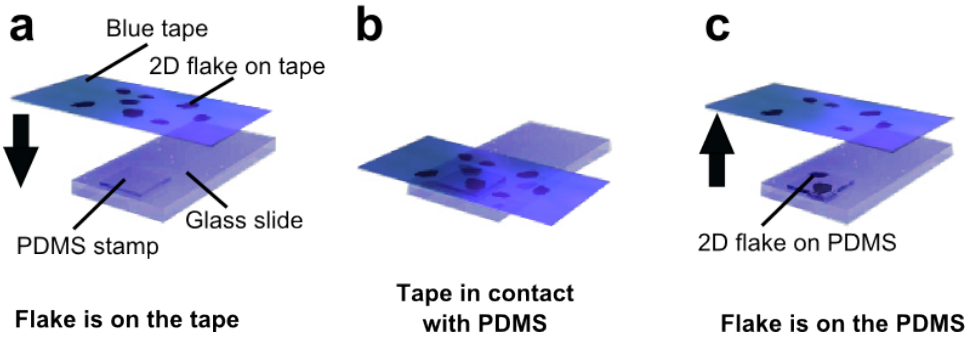


FIGURE 2.1: Schematic depiction of exfoliating a flake from the blue tape to the PDMS stamp. (a) The flake is on the blue tape. The tape is going towards the PDMS stamp. (b) The tape is put in contact with the PDMS stamp (c) The flake is exfoliated (either transferred completely or partly) onto the stamp. The blue tape is retracted.

Using optical microscopy one can select a suitable flake by optical contrast. For our purposes we preferred uniform flakes with little bulk attached, with a thin part of at least 20 by 10 µm big. The flake should not have any cracks or folds in the region of interest and should be big enough for the planned device. In Figure 2.2 one can see an example of such a flake, on top of a PDMS (Figure 2.2a) and after stamping on top of a SiN membrane substrate (Figure 2.2b). In this example the flake was stamped on top of a square slit in the membrane.

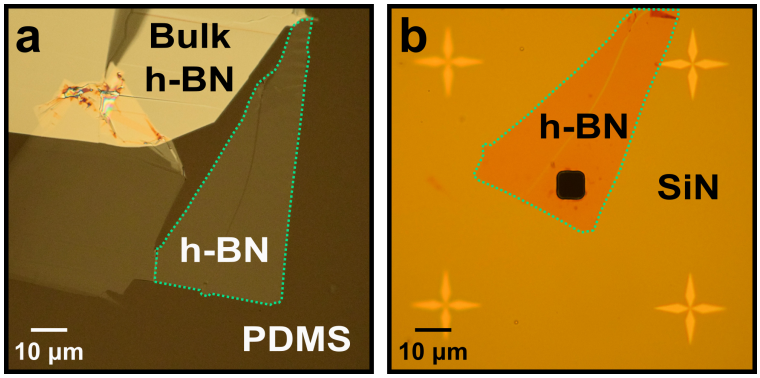


FIGURE 2.2: Optical images of the same flake before and after stamping. (a) h-BN flake on PDMS, 100x magnification (mirrored). The region of interest is highlighted by a green dashed line. (b) The same flake as in (a), highlighted by a green dashed line, after transfer on a SiN membrane with a 7 by 7 µm slit (black square in the middle), 100x magnification.

To make sure one can find the flake back during the stamping, we make several pictures of the flake with different lens magnifications. This way we can capture both the flake and its environment.

## 2.2 Stamping

After finding a suitable flake on the PDMS surface using optical microscopy, we stamp it onto the substrate.

### 2.2.1 Transferring the flake onto the substrate

As the third step, we transfer our preferred flake from the PDMS onto the prepared substrate. We do so, by using the dry stamping method, as proposed by Castellanos-Gomez [41].

Figure 2.3 shows the schematic of our stamping setup. The prepared substrate is fixed on top of the sample stage. This is done by either gluing the sample by the sides to a small thin glass plate using FixoGum glue and then fixing the glass plate on top of the sample stage using three layers of double sided tape (if the substrate is a membrane) or by simply gluing the substrate directly using three layers of double sided tape (if the substrate is a simple silicon/silicon dioxide chip). Those three layers will act as a buffer during the stamping, by indenting when the PDMS glass plate will touch the stage. As our experience showed, this allows all of the viscoelastic stamp to come in touch with the sample. In other configurations, when the sample is fixed by screws or vacuum, only a part of the stamp would touch the substrate. This would become a problem, if one's flake was located on the "non-touching" side.

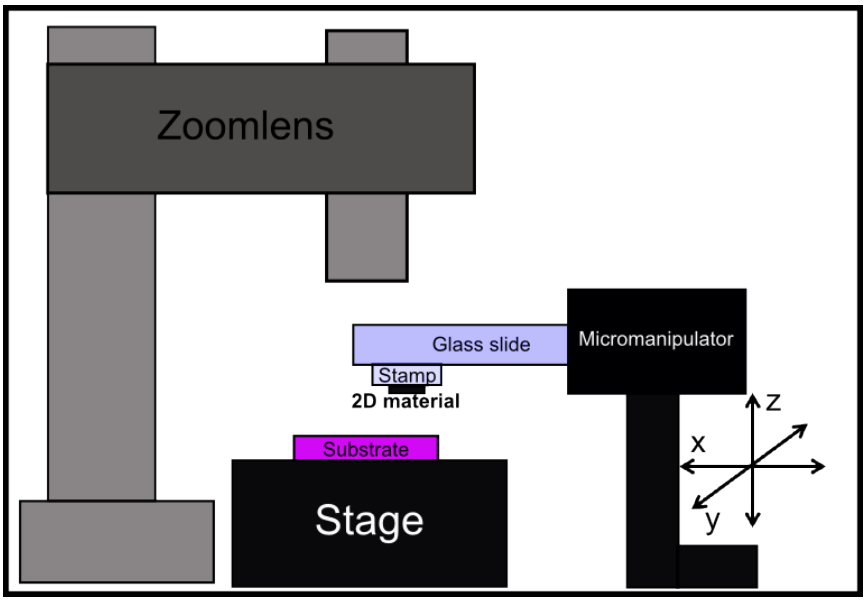


FIGURE 2.3: Schematic depiction of the stamping setup. The substrate is placed on top of a movable stage (x,y), below the zoomlens (up to 12x magnification). The glass slide with the PDMS stamp facing down is clamped in the micromanipulator (x,y,z).

The glass plate with the PDMS stamp on top of it would be fixed in the micromanipulator, facing with the PDMS down. To fix the glass plate properly, both on top and bottom of it is a layer of rubber. This layer will also act as a buffer and make sure the glass plate would not rotate during stamping.

The sample stage can move in the (x,y,z) plane and rotate around its axis. This is done using a micromanipulator, which can be moved manually in the (x,y,z) direction.

To find and align the flake with the slit, a zoomlens is used on top of the sample stage. The magnification is 12x. But using a camera and a big tv screen, one can enhance the visibility of the flake by making a big projection and using the digital zoom (5x to 10x) of the camera. This magnification would allow us to find most of the flakes of our size of interest. In case of doubt, the pictures made in Section 2.1.2 could be used to locate the flake by locating the bigger flakes around it.

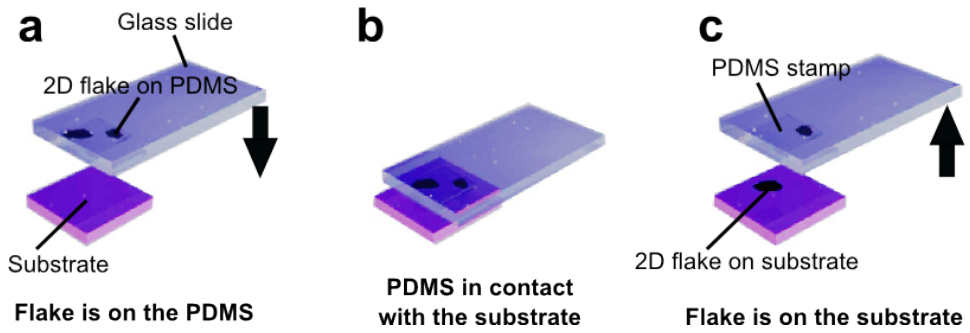


FIGURE 2.4: Schematic depiction of the stamping process. (a) The flake is on the PDMS stamp. The stamp is attached to the glass plate and is facing down. The glass slide is lowered toward the substrate. (b) The PDMS stamp is fully in contact with the substrate. (c) The flake is transferred from the PDMS to the substrate, the stamp and the glass slide are retracted.

Figure 2.4 shows a schematic depiction of the stamping procedure.

Once the flake is found and roughly aligned, we lower the glass slide with the PDMS towards the sample using either the piezo or the manual micromanipulator (Figure 2.4a). Right before touching the substrate, one has to make sure the alignment is still intact. Then one can slowly start to go down. When the stamp will touch the surface, it will become visible by optical contrast between the touching and non-touching part. The edge, the so called miniscus, will slowly roll over the flake (Figure 2.4b)

When we have made sure, that the flake is touching the substrate, we can begin to gently retract the PDMS from the sample. One can see if the flake is sticking to the surface, by optical contrast. If the flake sticks, it will remain roughly the same color. If it does not stick, the color will change. By playing with the (x,y) screws of the micromanipulator one can change the direction from which the miniscus will approach the flake, which sometimes would allow to increase the chance of the flake sticking if it would not stick in the first place.

Once it was clear, that the flake was fully transferred onto the surface, we retracted the PDMS completely at a higher speed (Figure 2.4c).

### 2.2.2 Preparing for lithography

Right after the stamping we make pictures of the flake at different magnifications, to make sure that the contacts would not go over other flakes in the surrounding. Usually at least one or two additional flakes would transfer onto the substrate during the stamping, and one should make sure the electrical contacts will go around those flakes, instead of crossing them.

If necessary and additional annealing step can be taken to avoid the flake shifting or detaching during spincoating. This step differs from device to device and (if present) is described in each chapter separately.

# Chapter 3

# $In_2Se_3$ phototransistors

## 3.1 Introduction

In many of daily life devices we are actively using photo-detector components. The possibility to transform a informational light signal into an electrical one, harvest the energy stored in the light or use photo-detection for optical imagining are all necessary processes that require photo-detectors.

Currently the most used material for such devices is bulk silicon. Although silicon-based photo-detectors can profit from scalability, low cost and miniaturization possibilities, they have multiple limitations. Due to the bandgap of 1.1 eV the light absorption range is limited to visible and near infrared, which reduces the efficiency. The need to employ thick bulk channels to achieve reasonable responsivities makes those devices brittle, non-transparent and non-flexible, which is why they are not suited for thin and bendable applications. Most of the 3D material alternatives to silicon suffer from the same limitations, despite a wider detection range, and usually add to the fabrication process complexity.

The discovery of graphene in 2004 [4,5] has introduced a completely new field of 2D layered materials [6,23–26,28–30,42–50,59], which might serve as a very good alternative to the current limited silicon-based photo-detectors. In those 2D materials the atoms are forming sheets with strong in-plane bonds and weak van der Waals forces between the layers. This allows to isolate thin flakes from the bulk crystal using the exfoliation method, reducing the device thickness down to few or even one single atom [5].

Those novel 2D materials show several advantages as compared to the traditional bulk silicon. Their few atomic layers make them almost transparent, which would allow them to be implemented in novel devices such as wearable electronics and stacking photovoltaics. Their thickness would also allow them to be used in flexible applications, including bendable solar cells and rollable displays. Finally the atomic thickness leads to quantum confinement effects in the out-of-plane direction, which could lead to strongly bound excitons and increased absorption efficiency [51–53] or bandgap dependence on the amount of layers, both effects particularly strongly present in transition metal dichalcogenides (TMDCs) [54–57].

Several photodectors based on 2D layered materials have been studied so far [42–47, 58–62], showing high optical gains ($MoS_2$, $TiS_3$, GaTe) and fast response (graphene). Yet the photogeneration mechanism is often unclear in those devices, usually being a mix of several processes. For example $MoS_2$ devices show a combination of photoconductive, photoelectric, photothermoelectric and photovoltaic effects [48–50]. Due to the high amount of influence factors that ensure contributions from those processes it is often hard to distinguish between those mechanisms, yet they define most of the detector properties, like responsivity, response time and dectivity.

In this chapter we present two devices based on few-layer $In_2Se_3$, in which we were able to not only characterize the dominant photogeneration mechanism, but also to control it using the gate voltage. We fabricated an $In_2Se_3$ phototransistor and characterized it in dark and under illumination. Our photodector shows one of the highest photoresponsivities ($9.8 \cdot 10^4$ A/W) and detectivities ($3 \cdot 10^{11}$ Jones) reported for 2D materials . We also demonstrate the possibility to control the dominant photogeneration mechanism switching between photovoltaic and photoconductive effects. Our second device supports our findings from the first one.

## 3.2 Sample characterization and setup

Two types of samples were fabricated in this work.

One consisted of a few-layer $In_2Se_3$ flake stamped using the dry transfer method [41] on the $Si/SiO_2$ chip, after which we fabricated Ti/Au contacts on top using e-beam lithography and evaporation. This sample served as our main device.

For the second sample we transferred our flake on top of pre-made Ti/Au contacts on top of the same type $Si/SiO_2$ chip. This device showed slightly different behavior as compared to the first one, due to the lack of PMMA contamination and less good electrical contact with the gold.

### 3.2.1 Crystal characterization

A monolayer of $In_2Se_3$ consists of five sheets of covalently bonded indium and selenium atoms, as shown in Figure 3.1a. The layers are held together by van der Waals forces. Different arrangements of indium and selenium within those five layers can lead to different crystal phases. Currently five such phases are known ($\alpha$, $\beta$, $\gamma$, $\delta$ and $\kappa$) [63, 64].

Our original $In_2Se_3$ crystal was ordered from 2dsemiconductors.com. In this work we have characterized an isolated $In_2Se_3$ multilayer exfoliated from that crystal using Raman spectroscopy and absorption spectroscopy, to determine its crystal phase. Raman spectra would allow us to distinguish the $\alpha$ and $\gamma$ phases from the other three. Then we use absorption spectra to determine the flake's bandgap, which would be 1.453 eV for the $\alpha$-phase [65] and 1.812 eV for the $\gamma$-phase [66].

First, we exfoliated a few-layer $In_2Se_3$ on top of the $Si/SiO_2$ chip. In Figure 3.1b one can see the optical image of the characterized flake with the blue laser spot where the Raman spectra were taken. In the next panel, Figure 3.1c, one can see the measured Raman spectrum. Raman peaks can be observed at 181 $cm^{-1}$ and 200 $cm^{-1}$, which correspond to the $A_1$ modes of the $\alpha$-phase of $In_2Se_3$ [67].

Then we transfer an $In_2Se_3$ flake onto a core of a multimode optical fiber by using the all-dry viscoelastic stamping technique [41]. In Figure 3.2a and 3.2b one can see the optical images of the flake with and without the lighted region. Figure 3.2c shows the absorption spectra of the flake. We plot the spectrum as $(A \cdot E)^2$ vs $E$, where $A$ is the measured absorption and $E$ is the energy in eV. This allows us to determine the bandgap by using a linear fit to the first slope of the spectrum and extrapolating it (extrapolation shown as the red dotted line). This gives us a value of 1.43 eV for the bandgap, which agrees with the reported values of 1.453 eV [65] for the $\alpha$-phase of $In_2Se_3$.

We can therefore safely conclude, that we are dealing with $\alpha$-phase $In_2Se_3$.

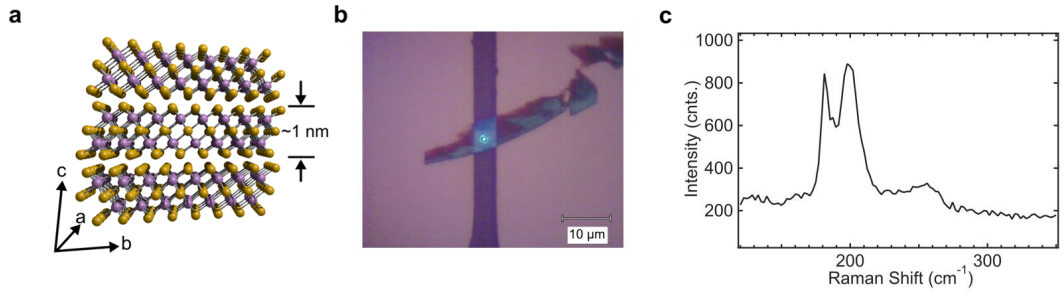


FIGURE 3.1: (a) Atom structure of $In_2Se_3$. (b) Optical image of a $In_2Se_3$ flake, with the laserspot at the position, where the Raman spectrum was taken. (c) Raman spectrum of the flake from panel b. The spectrum shows peaks at the location of $A_1$ modes of $\alpha$-$In_2Se_3$ (vibration along the a-axis in (a)).

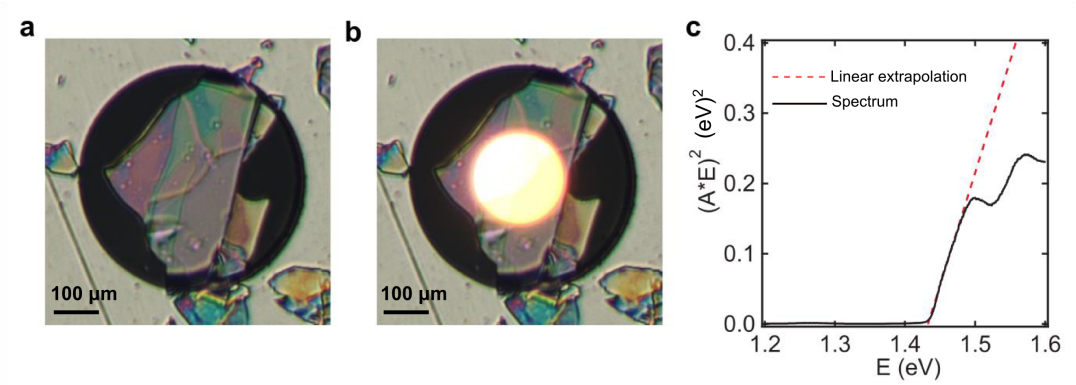


FIGURE 3.2: (a) Optical image of an $In_2Se_3$ flake transferred onto a multimode optical fiber. (b) The same flake with the lighted region indicating the core of the fiber (the core is 200 µm in diameter). (c) Absorption spectra of the flake used to determine the bandgap. The solid black line shows the spectra, and the red dotted line shows the linear extrapolation of the first slope.

### 3.2.2 Sample fabrication

In both types of devices we use highly p-doped silicon chips with a 285 nm thick oxide layer. This allowed us to use the doped Si as a backgate for our phototransistors, while the $SiO_2$ serves as a dielectric.

We fabricate our contacts (both top contacts for the first type of devices and prepatterned contacts for the second type) using e-beam lithography, thin metal deposition (5 nm of sticking layer Ti, and 60 nm of Au) and lift-off in warm acetone.

#### 3.2.2.1 Top contacts device

In the first type of device we start by exfoliating an $In_2Se_3$ flake on a PDMS stamp and then transferring it onto our $Si/SiO_2$ chip. This is done using the all-dry viscoelastic stamping method [41], as described in detail in Chapter 2. After the transfer, we deposit the metal contacts on top of the flake.

Figure 3.3a shows an optical image of our type one device. There are four contacts with a varying channel length (distance between two consecutive leads) from 1 to 3 µm. Figure 3.3b and 3.3c show an AFM picture of the same flake and its height

profile. The thickness of the contacted part is $14 \pm 5$ nm. This would correspond to $15 \pm 5$ layers of $In_2Se_3$ [66].

We also measured the transfer curves, as shown in Figure 3.3d, for contacts 1 to 2. The black curve is the forward sweep and the red curve the reverse sweep. The hysteresis is most likely caused by the trapped charges at the interface between the flake and the substrate [68, 69], and the gate voltage difference ($\Delta V_t$ = 11 V) allows us to estimate the trap density: $C \cdot \Delta V_t \approx 10^{12} cm^{-2}$. Here $C$ is the capacitance to the back gate per unit area.

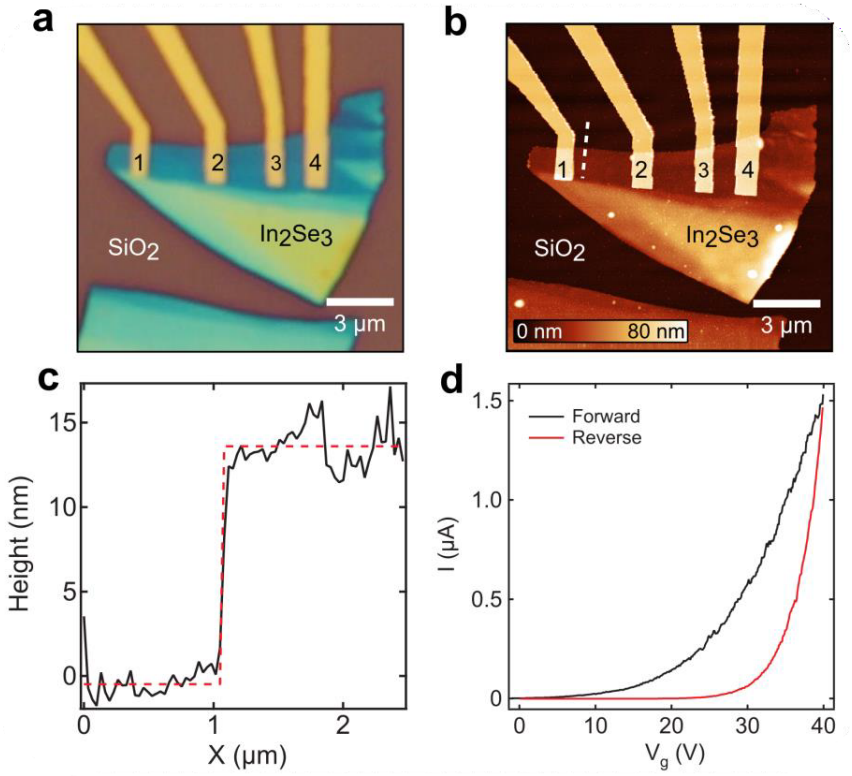


FIGURE 3.3: (a) Optical image of the top contacts device. (b) AFM image of the top contacts device from panel a. The white dotted line indicated the location of the height scan. (c) Height profile taken at the dotted line in panel b. (d) Gate trace for contacts 1-2. Black curve indicates a forward sweep, and the red one the reverse.

#### 3.2.2.2 Pre-patterned contacts device

In the second type we reverse the order. We start by depositing the pre-patterned contacts, and then transfer the flake on top. Since the stamping is not done in vacuum, the electrical contact will be not as good as in the first type of device. The advantage is that this process keeps the flake clean of possible PMMA residues, since it does not require an extra lithography step after the transfer.

Figure 3.4 shows an AFM image of the flake transferred onto the pre-patterned contacts. The inset shows a height profile.

### 3.2.3 Measurement setup

We perform our measurements in a *Lakeshore Cryogenics* probestation at a pressure below $10^{-5}$ mbar and room temperature. We used eight diode pumped solid state

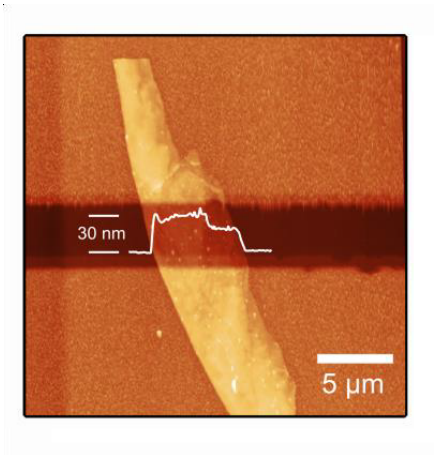


FIGURE 3.4: AFM image of the pre-patterned contacts device. The inset shows the height profile of the flake.

lasers that were operated in continuous wave mode (CNI Lasers), each with a different wavelength. The laser wavelength range is between 405 and 940 nm, going from purple into near infrared.

Figure 3.5 shows a schematic depiction of the setup. Each laser beam is led through two adjustable and two stationary parabolic mirrors into a multimode optical fiber. At the end of the fiber another parabolic mirror collimates the light exiting the fiber. The laser beam is then going through the zoomlens on top of the probe station and onto the sample. The beam spot is 200 µm for all wavelenghts.

For adjusting the laser power, a variable density filter is put in front of the beam, allowing to vary the power density between 0 and 100 % of the original laser power. For time-dependent measurement we use a chopper with adjustable rotation speed and three different chopper blades, for different frequency ranges. Figure 3.6 shows a photo of the setup, the insets showing the power filter and the chopper with its blades.

Figure 3.7 shows a photo of the electrical setup (Figure 3.7a) and the probe station (Figure 3.7b), and a schematic depiction of the setup (Figure 3.7c). We use an IV-rack to apply the voltage to the probes and measure the current. An AdWin unit serves as an DAC/ADC converter to connect the rack to the computer. The bias and gate voltage are sweeped using a LabView script.

On top of the probe station a zoomlens and a camera are positioned, with the optical fiber connected to the zoomlens and a screen attached to the camera. This allows us to position the probes and focus the laser beam on the right spot.

For time-resolved measurement we do not use the AdWin unit, but send the signal directly to an oscilloscope, to avoid unnecessary capacitance in the system. This allows us to keep the RC cutoff frequency of the setup high and measure short rise and fall times.

## 3.3 Photoelectric characterization

Most of our measurements were performed at 640 nm laser wavelength. We measured the current in dark and under illumination, varying the applied laser power between 0 and 5 mW. We also varied the gate voltage, with an ON state between -20 and 50 Volts and an OFF state in the -40 to -20 volts, since few-layer $In_2Se_3$ proved

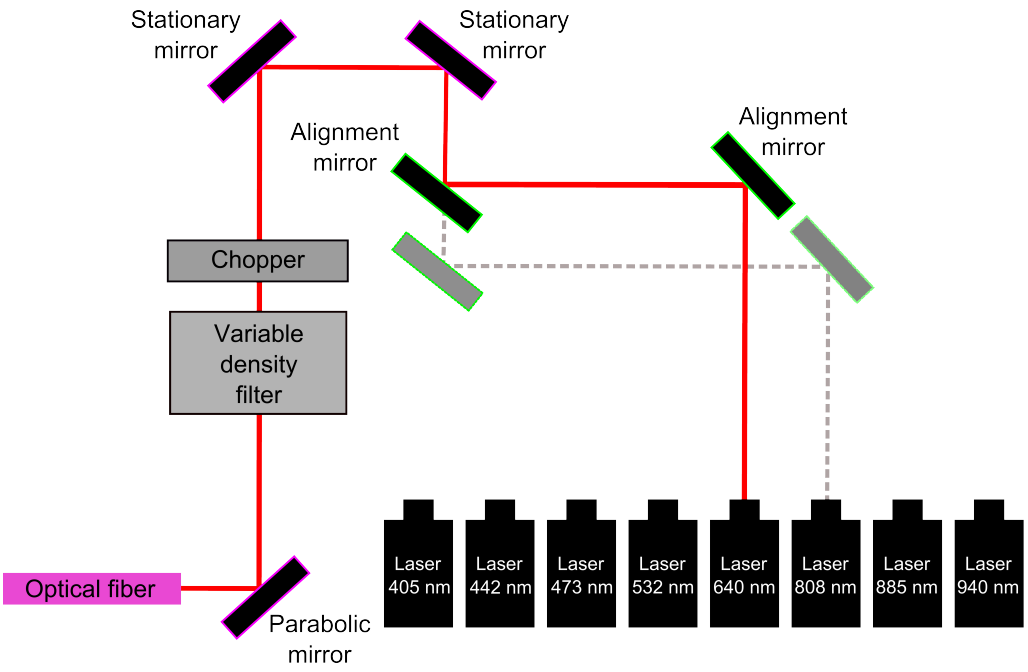


FIGURE 3.5: Schematic depiction of the laser setup, with the red (640 nm) laser on. The grayed out laser beam and mirrors indicate a setup for the infrared (808 nm) laser.

to be n-type. From those measurements we were able to calculate the responsivity $R$, detectivity $D^*$ and the exponent $\alpha$ that defines the correlation between the photocurrent and laser power, which is important for determining the dominating photogeneration mechanism.

We also did time-resolved measurement using a chopper in front of our laser, to characterize the speed of the optical response of our device. We found two different signals overlapping, with a slow and fast component present for the ON state and only the fast one present for the OFF state.

Finally we made a set of wavelength dependent measurements, that showed a broadband photoresponse of $In_2Se_3$ and a peak in photocurrent around 532-808 nm.

All of those measurements allowed us to properly characterize the optoelectrical response of our device and gain insight in its photogeneration mechanisms.

### 3.3.1 Measurements at different laser powers

#### 3.3.1.1 Top contact device

We start by characterizing our flake in the dark. In Figure 3.8a one can see a gate sweep, current plotted vs gate voltage, in both linear scale (black line) and logarithmic scale (orange line). The curves show a typical n-type behaviour, with an ON state between -20 V and 40 V and an OFF state from -40 V and -20 V. From this graph we can calculate the ON/OFF ratio, which is about $10^5$. This allows us to estimate the field-effect mobility $\mu$ using the transmission line model [70,71]:

$$R_{tot} = R_c + \frac{L}{W \cdot C_{ox} \cdot \mu \cdot (V_g - V_t)} \tag{3.1}$$

Where $R_{tot}$ is the total measured resistance, $R_c$ is the contact resistance (which we can estimate using a linear fit to the resistance versus channel length), $L$ and $W$ are

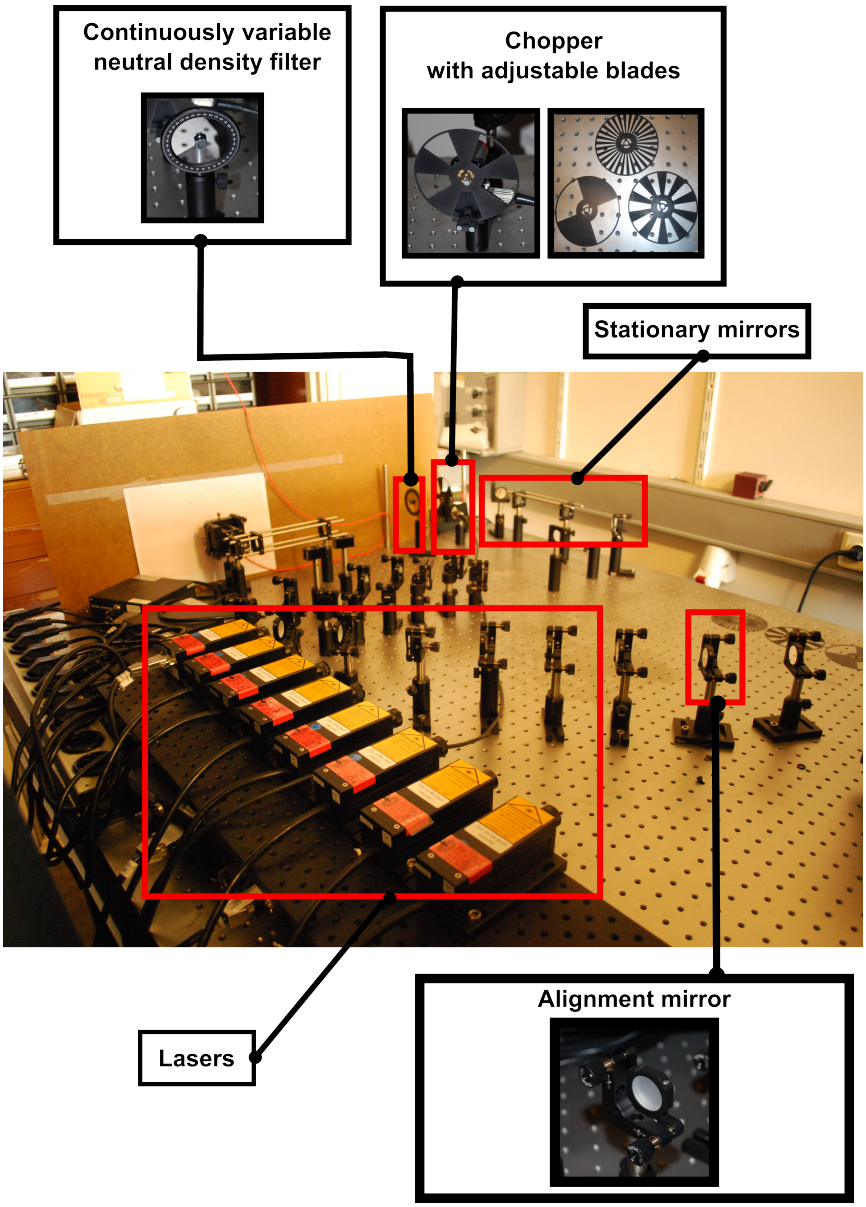


FIGURE 3.6: Photo of the laser setup. The insets show different parts of the setup.

the channel length and width respectively, and $C_{ox}$ is the parallel plate capacitance to the gate. In this case the length of the channel is the distance between the two contacts and the width is the overlap region of the contact lead and the flake.

In an effort to contact only the thinnest homogeneous part of the flake, the overlap of the contact leads is only partial. Therefore we have included an error of 25 % in our estimation of the channel width. This error propagates further in our calculation of mobility, responsivity and detectivity.

At the gate voltage of 40V we estimate the field-effect mobility to be $30 \pm 8$ cm$^2$ V$^{-1}$ s$^{-1}$.

Figure 3.8b shows the IV-characteristics of the device, measured in the dark. The current is plotted against the bias voltage at different gate voltages. The curves all look linear, showing no sign of Shottky barriers at the lead-flake interface. This indicates a good electrical contact.

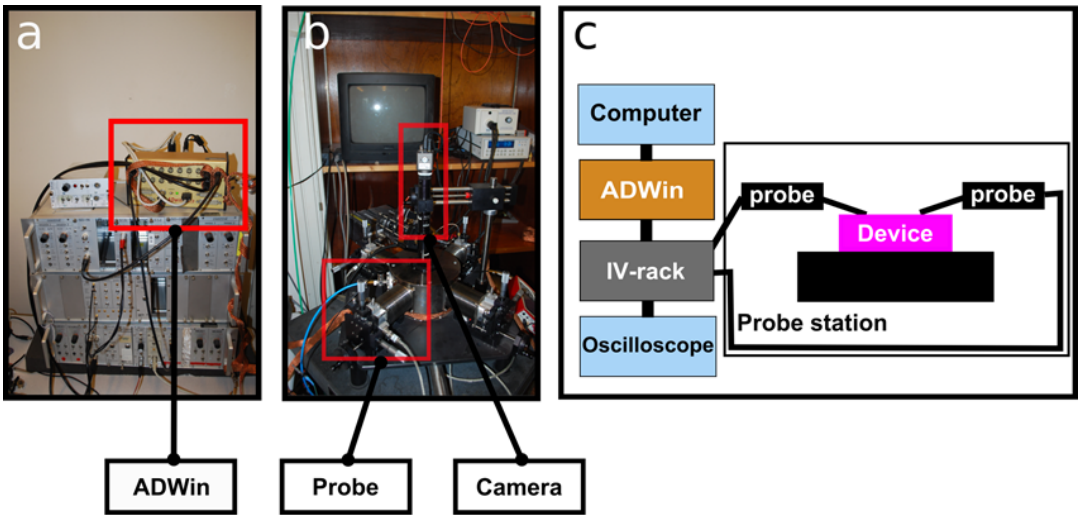


FIGURE 3.7: (a) Photo of the IV-rack. (b) Photo of the probe station. (c) Schematic depiction of the electrical setup.

Next, we characterize the device under illumination. Figure 3.9a shows the current $I$ measured as function of the gate voltage $V_g$ at different laser powers. The power ranges from 0 to 5 mW, the bias voltage is kept at 50 mV, the laser wavelength is 640 nm. By extrapolating the linear part of the curves one can obtain the threshold voltage $V_t$ from the point where the linear fit goes to zero. One can clearly see the shift in $V_t$ towards the lower gate voltages with increasing laser power.

The inset shows the difference in threshold voltage $\Delta V_t$ due to the photoelectric effect as function of the laser power. There is a sharp decrease towards lower laser powers, but at higher powers the curve saturates.

By subtracting the current measured in dark $I_{dark}$ from the current measured at illumination $I_{light}$, we can calculate the photocurrent $I_{ph}$:

$$I_{ph} = I_{light} - I_{dark} \tag{3.2}$$

The photocurrent is plotted as function of the effective laser power $P_{eff}$ in a log-log plot for different gate voltages in Figure 3.9b, with dotted lines showing the linear fits to the data curves. We calculate the effective laser power by taking into account the ratio of the laser spot and the actual device size:

$$P_{eff} = P_{in} \cdot \frac{A_{device}}{A_{laserspot}} \tag{3.3}$$

With $P_{in}$ the incoming laser power, $A_{device}$ the area of the device and $A_{laserspot}$ the area of the laser spot. $P_{eff}$ is the amount of laser power absorbed by the device.

Using the calculated photocurrent $I_{ph}$ and the effective power $P_{eff}$ we can obtain the responsivity $R$:

$$R = I_{ph}/P_{eff} \tag{3.4}$$

Figure 3.9c shows the responsivity plotted as function of the effective power for different gate voltages. Even at low bias of 50 mV, $R$ reaches a value of $9.8 \pm 2.5\ 10^4$ A/W at the gate voltage of 30 V.

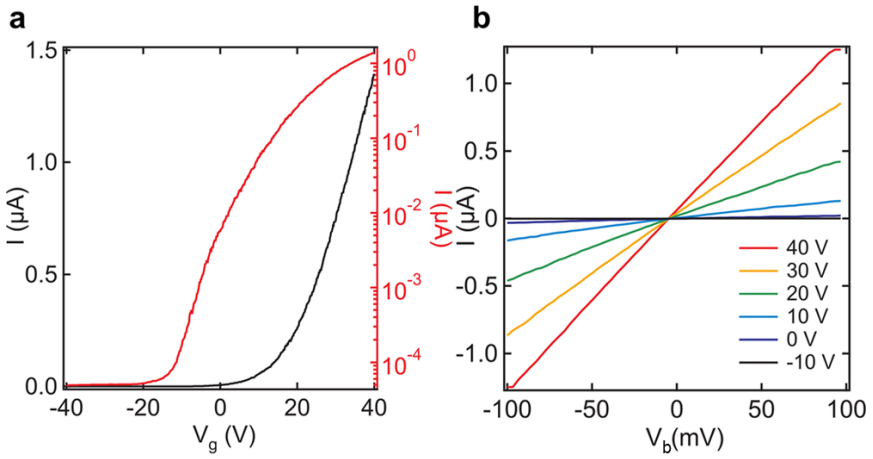


FIGURE 3.8: (a) Transfer curve of the top contact device, measured between contacts 3 and 4, in dark. The black curve is plotted in linear scale, the red curve on a logarithmic scale. (b) I-V curves for different gate voltages of the top contact device, measured between contacts 3 and 4, in dark.

#### 3.3.1.2 Pre-patterned contacts device

We also performed the same type of measurements on our flake with pre-patterned contacts.

In Figure 3.10a one can see the gate trace of the sample taken in the dark for different bias voltages. Similar n-type behaviour is observed, but as one can see, with a much higher bias voltage (1 to 5 V) than the top contact device (100 mV) one can reach only a small current.

Figure 3.10b shows the current $I$ plotted as function of the bias voltage. Again, the current values are several orders of magnitude lower and the curves show non-linear behaviour for higher gate voltages.

Figure 3.11 shows the characterization of the flake at different laser powers. Similar behaviour is observed as shown by the top contact device, except for an order of magnitude lower values of responsivity (see Figure 3.11c).

### 3.3.2 Time-resolved measurements

As our next step, we did time-resolved measurements to see how fast our system would respond to a modulated signal. For that purpose we use a chopper, that blocks and unblocks the laser at a set frequency. We turn on the laser with the chopper for a period of 10 seconds, and then turn the laser off. In the ON state ($V_g$ = 0 V) we see two types of responses. Figure 3.12a shows a slow response of the measured current, obtained in this single on/off cycle. The fall time (taken between 90 % and 10 % of the total current) is $\approx$ 9 s.

Yet, on top of the slow signal, we also discovered a much faster response, induced by the chopper modulation, as can be seen in the inset of Figure 3.12a. These data are taken from the top of the peak in the main panel of Figure 3.12a, with the average level of the peak ( $\approx$ 300 nA) subtracted. Figure 3.12b shows one period (smoothed with an averaging filter) of this faster signal. As one can see, it has a fall time of $\approx$ 30 ms.

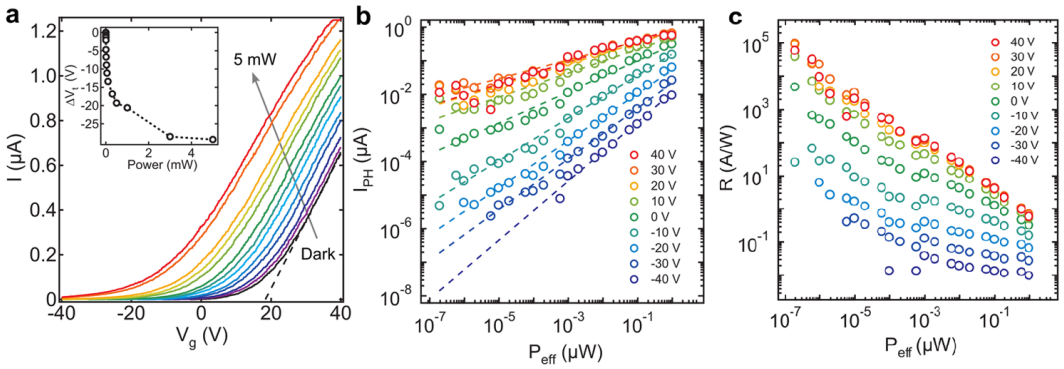


FIGURE 3.9: (a) Transfer curves of the top contact device, measured between contacts 3 and 4, at different laser powers (1 nW to 5 mW). All are measured at the wavelength of 640 nm and bias voltage of 50 mV. Inset shows the shift of the threshold voltage for increasing laser power. (b) Photocurrent as function of laser power for different gate voltages. Wavelength is 640 nm, bias voltage is 50 mV. Circles indicate the data points, dotted lines show linear fits to the data curves. (c) Responsivity calculated from the photocurrent in panel b.

We repeated the measurement in the OFF state ($V_g$ = -40 V), and found that the slow response disappeared, but the fast component remained, see Figure 3.12b. Again the modulation frequency was 10 Hz.

In Figure 3.13 one can also see the response of the pre-patterned contacts device. The measurement is again done at 640 nm, 10 Hz chopper modulation, in the OFF state ($V_g$ = -40 V). The fall time is $\approx$ 2 ms, which is an order of magnitude faster than our main device.

### 3.3.3 Measurements at different wavelengths

As our last step we do a set of measurements at different laser wavelengths. The result can be seen in Figure 3.14. The first panel shows the current as function of the gate voltage for different laser wavelengths. A wide broadband response can be observed.

The next panel shows the photocurrent plotted versus the wavelength. We observe a clear peak around 532-808 nm. Figure 3.14c shows the same measurement for the pre-patterned contacts device, showing a similar behaviour with a peak around 640 nm.

It has been proposed that the native oxide that forms at the surface of $In_2Se_3$ in ambient conditions and the intrinsic defects in the material can also contribute to the photoresponse by absorbing incident light [65]. Since the oxide layer has a bandgap around 569 nm (2.18 eV) this could explain the peak shown in Figure 3.14b and 3.14c. In this wavelength range the oxide contributes to the response and light absorption, which enhances the overall photogain.

## 3.4 Discussion

### 3.4.1 Photocurrent generation mechanisms

There are several known photocurrent generation mechanisms possible [6], with the main ones for the layered phototransistors being:

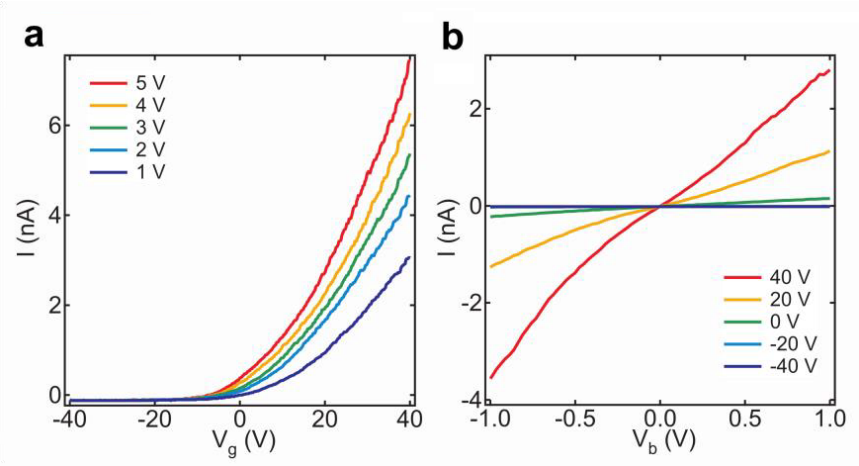


FIGURE 3.10: (a) Transfer curves of the pre-patterned contacts device for different bias voltages. (b) I-V curves for different gate voltages of the pre-patterned contacts device.

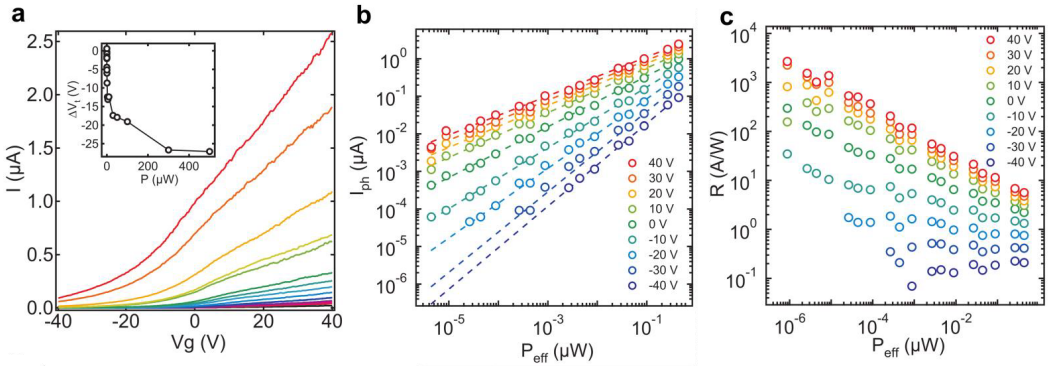


FIGURE 3.11: (a) Transfer curves of the pre-patterned contacts device at different laser powers (1 nW to 500 μW). All are measured at the wavelength of 640 nm. Inset shows the shift of the threshold voltage for increasing laser power. (b) Photocurrent as function of the laser power at different gate voltages. (c) Responsivity calculated from the photocurrent in panel b.

1. Photoconductive effect
2. Photovoltaic effect
3. Photothermoelectic effect
4. Bolometric effect

We employ a relatively large laser spot (200 μm in diameter), so we do not expect the last two mechanisms to contribute due to the lack of big thermal gradients and temperature differences. At our highest laser power ($\approx$ 1 μW/μm$^2$) we estimate the temperature gradient to be less than 0.1 K [48]. From that we can calculate the expected induced voltage difference $\Delta V$:

$$\Delta V = \Delta T \cdot S \tag{3.5}$$

With $\Delta T$ being the temperature difference due to the gradient and $S$ being the Seebeck coefficient, in our case 200 μV/K [72]. This gives us a $\Delta V$ of 20 μV, which is negligible compared to our bias voltage of 50 mV.

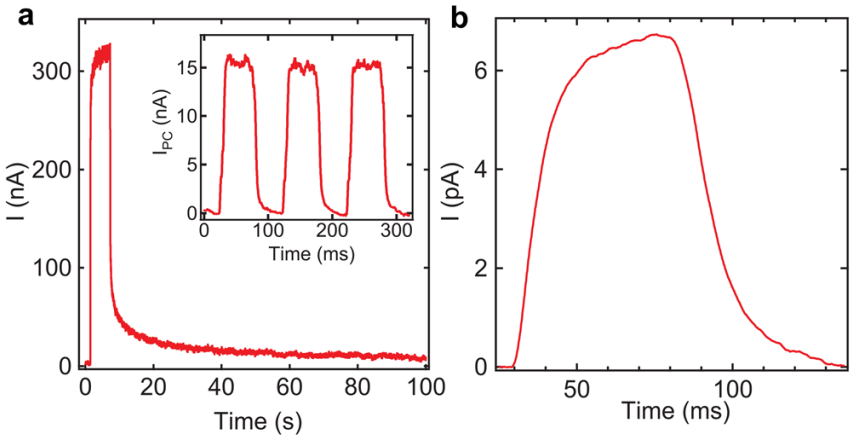


FIGURE 3.12: (a) Drain current measured for the top contact device as a function of time at zero gate voltage. The rise and fall times are determined by turning the laser (5 mW) on and off for 10 seconds once, while modulating a chopper at a frequency of 10 Hz. The inset shows the fast response on top of the higher gain, slow response (at 1 mW power), with the average level ($\approx$ 300 nA) subtracted. (b) Single (smoothed with an averaging filter) illumination cycle at the gate voltage of -40 V and laser power of 1 mW. The chopper frequency is 10 Hz.

This leaves us with the first two mechanisms: the photoconductive effect and the photovoltaic effect.

Photoconductive effect generates photocurrent due to the increase of extra free carriers. By absorbing light with energy higher than the bandgap, electron-hole pairs are created, that can contribute to the drain current. This increase, $I_{PC}$, can be calculated the following way:

$$I_{PC} = q \cdot \mu \cdot n \cdot E_f \cdot W \cdot D \tag{3.6}$$

With $q$ the charge per carrier, $\mu$ the carrier mobility, $n$ the excess carrier density, $E_f$ the electric field in the channel, $W$ the width of the channel and $D$ the absorption depth [73].

In case of photoconductive effect, the photocurrent will increase linearly with the applied effective laser power: $I_{ph} \propto P_{eff}$ [73,74].

The photogating effect, on the other hand, creates photocurrent by increasing the threshold voltage, which in turn gives rise to an additional drain current:

$$I_{PV} = g \cdot \Delta V_t \tag{3.7}$$

Where $g$ is the transconductance and $\Delta V_t$ the shift in the threshold voltage. Generally this drain current $I_{PV}$ increases sublinearly with the increasing laser power, which leads to a different exponent: $I_{PV} \propto P_{eff}^{\alpha}, \alpha < 1$ [74,75].

In case of van der Waals materials phototransistors, due to the large surface to volume ratio, the photogating effect increases the gate voltage, by occupying long-lived surface and interface trap states [47, 50, 76]. In our case the traps are most likely formed at the interface of natural oxide, which forms because of the vacancies in the bottom plane layers of the $In_2Se_3$ [65]. It has been shown before that surface oxides can give rise to photogating effects in ZnO and GaN nanowire photodetectors [77,78].

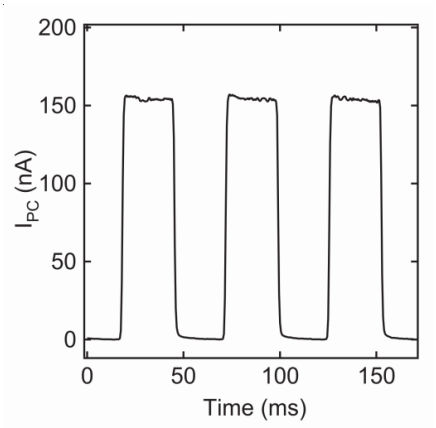


FIGURE 3.13: Drain current of the pre-patterned contacts device measured as function of time at gate voltage of -40 V. The rise and fall times are determined by blocking the laser (1 mW) with a chopper.

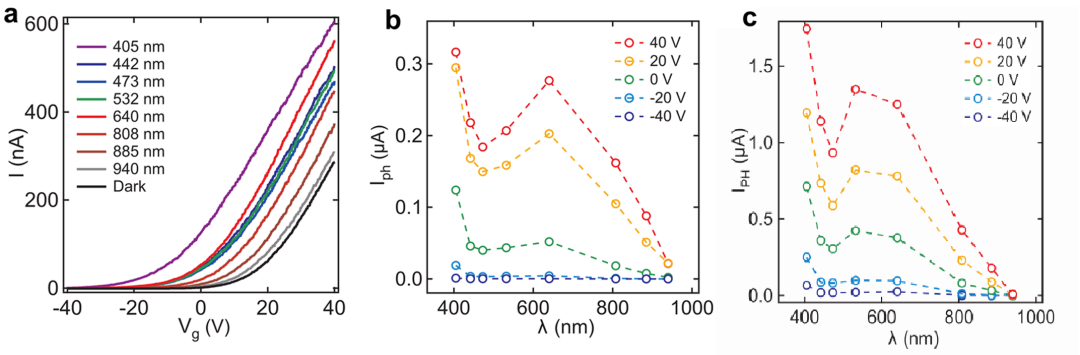


FIGURE 3.14: (a) Transfer curves of the top-contact device at different illumination wavelengths. (b) Photocurrent of the top contact device extracted from panel a at different gate voltages. (c) Photocurrent of the pre-patterned contact device at different gate voltages.

One can also see the presence of trap states from the hysteresis shown in Figure 3.3d. Additionally, trap saturation is evident from the way the threshold voltage shift (inset in Figure 3.9a) is saturating with the increasing laser power. The same can be observed in Figure 3.9c, where the responsivity $R$ decreases with the $P_{eff}$. By applying a higher laser power, one fills all the trap states, monotonically decreasing the gain [47, 76, 79, 80].

Therefore we can interpret the shift in the threshold voltage, observed in figures 4.8a and 4.10 as the photogating effect due to the trap states. Since the pre-patterned contacts device has no PMMA residues, this can also explain why the current is less compared to the top contacts device. Lack of residues and less direct contact with the silicon dioxide of the substrate leads to less trap states, lowering the photogating effect and the gain.

By fitting the curves in Figure 3.9b, we are able to extract the exponent $\alpha$, which defines the correlation of the photocurrent $I_{ph}$ and the effective laser power $P_{eff}$:

$$log(I_{ph}) = \alpha \cdot log(P_{eff}) + \beta \tag{3.8}$$

$$I_{ph} = P_{eff}^{\alpha} \cdot exp(\beta) \tag{3.9}$$

We calculate $\alpha$ for different contact pairs of our main device and plot them as function of the gate voltage in Figure 3.15a. One can see that the curve starts at ≈1 for the OFF state and then goes to <1 for the ON state.

This indicates, that in the OFF state the photocurrent is dominated by the photoconductive effect ($\alpha = 1$), while in the ON state the photogating effect comes into play, causing a sublinear behaviour of the current versus the laser power ($\alpha < 1$) [6].

Figure 3.15b shows the extracted alpha's for the pre-patterned contacts device. As we can see a similar behaviour as in our main device is observed: the coeffiecient is around 1 in the OFF state and goes significantly down for the ON state. Yet, the lowest values in this flake are higher than the top contact flake, which supports the theory that lack of residues reduces the amount of trapped stated on the surface and decreases the photovoltaic effect.

The time-resolved measurements (Figures 3.12 and 3.13) also support this explanation. The photovoltaic effect leads to a slow response due tot the slow decay of the long-lived trapped states, while the photoconducting effect is responsible for the fast response on top. This is supported by the fact that the slow response disappears in the OFF state. This is also supported by the comparison of the two types of devices: by reducing the trap states in the pre-patterned contacts sample, one increases the over-all speed of the system by lowering the slow photovoltaic contribution.

This means, that by varying the gate voltage and going from ON to OFF state, we can either bring the device into a slow and high-gain mode (ON, photovoltaic effect dominating) or in a fast and low-gain mode (OFF, photoconducting effect dominating).

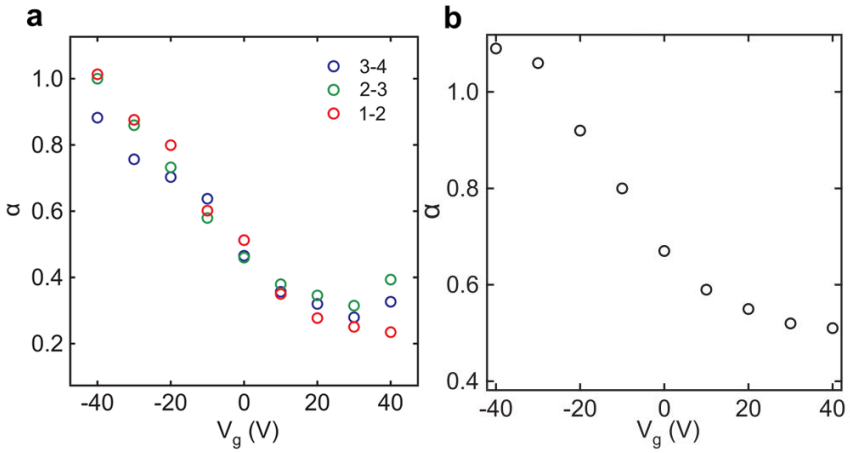


FIGURE 3.15: (a) Calculated exponent $\alpha$ for the top contact device as function of gate voltage, for different contact pairs (1-2, 2-3 and 3-4). (b) Calculated exponent $\alpha$ for the pre-patterned contact device as function of gate voltage.

### 3.4.2 Comparison to other 2D materials

In order to compare $In_2Se_3$ as a possible photodector to other 2D materials, we calculated the inferred detectivity $D^*$. This quantity allows to compare photodetectors of different size and bandwidth. We can calculate it in the following way:

$$D^* = R \cdot \frac{\sqrt{A_{device} \cdot B}}{\sqrt{2 \cdot e \cdot I_{dark}}} \tag{3.10}$$

With $R$ the responsivity, $A_{device}$ the surface area of the device, $B$ the bandwith and $I_{dark}$ the dark current.

In the OFF state (-40 V to -20 V), where the fast photoconducting regime is dominating, we use a bandwidth of 30 Hz, and in the ON state (-20 V to 40 V), where the slow photovoltaic effect is limiting the response time, we use 0.1 Hz for bandwidth.

In Figure 3.16 one can see the calculated detectivity, the highest value reaching $3.3 \pm 0.8 \cdot 10^{13}$ Jones at the gate voltage of 20 V.

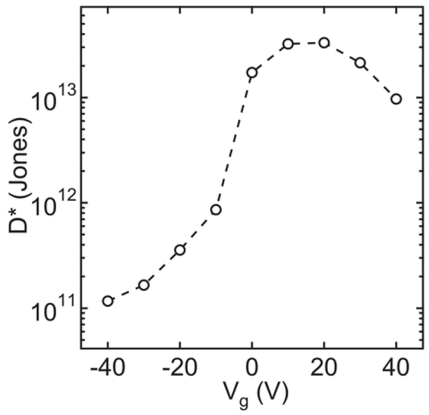


FIGURE 3.16: Calculated detectivity for the top contact device as function of gate voltage.

In Table 3.1 one we compare our results with the value from literature for other multilayer 2D materials. We list the type of material, its thickness $d$, the responsivity $R$, the gate voltage $V_g$ and bias voltage $V_b$ at which $R$ was calculated, the detectivity $D^*$ and the rise and fall response time $t_{resp}$. Our results are shown in bold.

At the time of our publication [81] our photoresponsivity was considered the highest ever reported [6] for a 2D multilayer. As you can see from Table 3.1, only a few 2D materials based devices managed to surpass it in the last three years.

Note that the three cases with higher responsivity all use two orders of magnitude higher bias voltage.

In case of Graphene nanoribbons [27] a smaller effective laser power is employed ( $10^{-9}$ µW) than in our case. When we compare the responsivity at the same laser power ($10^{-7}$ µW), we get a value of $10^5$ A/W which is comparable to our result of 9.8 $\cdot$ $10^4$ A/W.

Admittedly, the few-layer Black Phosphorus [30] and the few-layer $MoSe_2$ [29] both show a higher photoresponsivity and faster response times than our device. The latter also shows a better detectivity, although the same order of magnitude as the one we obtained for our multilayer $In_2Se_3$.

TABLE 3.1: Comparison of photoresponsivity $R$, with gate voltage $V_g$ and source-drain voltage $V_b$ at which it was calculated, detectivity $D^*$ and response times $t_{resp}$ of different 2D materials with thickness $d$ indicated.

| Material | d (nm) | R (A/W) | $V_g$ (V) | $V_b$ (V) | $D^*$ (Jones) | $t_{resp}$ (rise/fall) | ref |
|---|---|---|---|---|---|---|---|
| few-layer BP | 8 | 670 000 | -15 | 1 | - | 5 ms/ - | [30] |
| Graphene nanoribbons | 4 | 500 000 | 0 | 1 | $3{\cdot}10^{11}$ | 25 ms/ 75 ms | [27] |
| multilayer $MoSe_2$ | 25 | 140 000 | 40 | 1 | $5.5\cdot10^{13}$ | 1.7 ms/ 2.2 ms | [29] |
| **multilayer $In_2Se_3$** | **14** | **98 000** | **40** | **0.05** | **$3.3{\cdot}\ 10^{13}$** | **1 s / 9 s** | [81] |
| few-layer $ReS_2$ | 2.5 - 4.5 | 88 600 | -50 | 4 | $1.2{\cdot}10^{11}$ | 1-10 s | [28] |
| β-InSe nanosheets | 4 - 60 | 56 800 | 40 | 5 | $1{\cdot}10^{13}$ | 5 ms/ 8 ms | [23] |
| multilayer $MoS_2$ | 80 | 342.6 | 8 | 1 | - | - | [31] |
| multilayer $HfSe_2$ | 15.8 | 252 | 80 | 2 | $1{\cdot}10^{11}$ | 7.8 ms | [26] |
| multilayer $\alpha$-$I_2Te_3$ | 22 | 44 | 0 | 5 | $6\cdot10^{12}$ | 15 ms/ 15 ms | [25] |
| multilayer GaSe | 72 | 0.57 | 0 | 10 | $4.05\cdot10^{10}$ | - | [24] |

# Chapter 4

# Thermal transport in suspended h-BN

## 4.1 Introduction

Since the discovery of graphene in 2005 [4, 5] the research field of 2D materials, layered materials with covalent in-plane bonding and weak van der Waals forces between the layers, has been steadily growing. In the last 14 years multiple works have been published, showing remarkable electrical [7–12], optoelectronic [6, 13, 14, 81] and optical [15–20, 82] properties of those materials, not present in their bulk counterparts. Examples include high electrical mobilities [4,9], indirect-to-direct bandgap transition [13] and unconventional superconductivity [12]. Many of those materials form attractive candidates for low-dimensional devices, allowing to further reduce the size of our electronics. Yet only several experimental works [32–36] have been published on their thermal properties, and our knowledge on the possibility to implement 2D materials as cooling and thermal isolation components remains limited.

In many of the 2D materials the thermal transport is governed by phonons [32, 36]. One of the key properties of the thermal phonon transport is the phonon mean free path ($\Lambda_{ph}$), the average length that a phonon can travel through the medium without collision. The length of $\Lambda_{ph}$ compared to the size of the measured sample determines the type of thermal transport in the material. Graphene has been reported to have an unusually long mean free path [37, 83] and three different thermal transport regimes. In addition to the usual ballistic ($\Lambda_{ph}$ longer than sample length) and diffusive ($\Lambda_{ph}$smaller than sample length) regime, a second sound regime has been recently measured in graphite samples [84]. Additionally a systematic study on the thermal conductivity dependence on the sample size in graphene has been conducted, showing a clear influence of the flake dimension on the thermal transport [85].

Several theoretical studies suggest that similar properties could be observed in few-layer hexagonal boron nitride (h-BN) flakes as well [84,86,87] due to comparable disorder in the material. Yet the predictions for the $\Lambda_{ph}$ of h-BN have been inconsistent so far, mentioning values from 30 nm up to 550 nm at room temperature in different studies [32, 88–91]. No experimental studies have yet been conducted to investigate the influence of the sample size on the thermal transport of h-BN. Nor have there been any time-resolved measurements that could investigate the type of thermal transport in h-BN few-layer flakes.

So far, two experimental methods have been employed to measure the thermal properties of the 2D materials. The confocal micro-Raman method [37, 92] and the thermal bridge method [37,38]. Unfortunately both methods have certain disadvantages. The Raman method has reportedly shown to have high measurement uncertainty for the measured temperature increase (reported relative uncertainty values

of 30% and 50%) [37, 39, 40], which increases at lower bath temperatures. Moreover the accuracy of the method highly depends on the intensity of the Raman signal of the material, therefore almost excluding the possibility to measure materials with weak response, such as h-BN [34]. The thermal bridge on the contrary has relatively high measurement precision for the temperature difference and can be employed to measure at cryogenic bath temperatures, but was so far limited by a steady state configuration.

A third method, $3\omega$ technique [93], gives a good alternative to those two, combining their advantages - high precision, even at low temperatures, and possibility to perform time-resolved measurements. Unlike the Raman method, it does not require a small optical bandgap and can be used for measuring all possible materials, including optically transparent ones. So far it has not been yet used for 2D materials, but has been successfully employed previously to measure other types of thin films [94, 95].

In this chapter we show it is possible to implement a setup based on this method that allows to measure both thermal conductivity and thermal diffusivity of suspended 2D flakes. As compared to the thin films, for which the original method is normally used, the 2D flakes have the disadvantage of a relatively small surface area and an irregular shape. Moreover, since the flakes are only several atomic layers thick, they need a supporting substrate and can not be measured completely isolated from it. To compensate for those factors we have modified the original $3\omega$ setup and used the improved technique to measure the thermal conductivity and diffusivity of few layer h-BN.

We measure several samples, with different flake lengths and thicknesses, and show how the size of the flake influences the thermal properties of the sample.

## 4.2 Theory

### 4.2.1 Fourier's law

In this chapter we study thermal transport in solids, where the energy is transferred from one spot to another through conduction. The heat can be carried by electrons, lattice vibrations (phonons) or other quasiparticles (like magnons and excitons) that spread their energy through collisions.

One of the most fundamental relations in the conduction heat transport is the Fourier heat conduction law [96]:

$$\vec{q} = -\lambda \cdot \vec{\nabla} T, \tag{4.1}$$

with $\vec{q}$ being the energy current density, $\lambda$ the thermal conductivity and $\vec{\nabla} T$ the gradient of the temperature.

For the one-dimensional case one can write Equation 4.1 in the following form:

$$\frac{\Delta Q}{\Delta t} = -\lambda \cdot A \cdot \frac{dT}{dx}, \tag{4.2}$$

with $\frac{\Delta Q}{\Delta t}$ being the amount of heat flowing per second, $A$ the surface area through which it flows, $\lambda$ the thermal conductivity in and $dT/dx$ the derivative of the temperature along the heat flow axis.

This law states that if a certain power is applied to the material in order to heat it, then the temperature difference caused by this heating will be proportional to it,

with the thermal conductivity $\lambda$ of the material and the dimensions of the measured geometry serving as the proportionality constant.

Fourier's law was originally formulated as a simple, intuitive emperical relation [96], but has been experimentally shown to be valid in many of macroscopic systems and forms of thermal transport. It is generally assumed that for significantly low thermal gradients the linear relationship almost always holds, since many functions become linear when approaching zero. Moreover, no reports of deviations in low power regime have been made so far. But there have been several reports of the violation of Fourier's law in nanoscale systems [84,86,87,97–105], when the temperature gradient becomes high enough for Equation 4.1 not to be valid anymore due to nonlinear effects.

When exactly the system will leave the low power regime in which the Fourier's law is valid depends highly on the scale and the material in question. For some systems it is almost impossible to reach such high gradients, while for others it is the other way around. The reported deviations in nanoscale systems could be explained by the very small cross-section area $A$, as well as the possibility to reach higher gradients due to 2D physics coming into play [106]. So far several reports of such deviations have been published for ballistic systems, while most of the diffusive thermal transport stays within the prediction of the Fourier's law [107]. However, even for diffusive systems there have been reports of violations [101, 102]. In those works the predicted linear relation between thermal resistance of a nanotube and its length by Fourier's law was not confirmed. The nanotubes showed an above-linear behavior.

Therefore it is of high importance to study whether the measurements are within the linear regime and the linear relation still applies. When it applies one could use Fourier's law to obtain the thermal conductance of the system. In case of a diffusive system one could also calculate the system's thermal conductivity.

Combining Fourier's law and the law of conservation of energy, one can also derive the famous heat diffusion equation:

$$\frac{\partial T}{\partial t} = D \cdot \nabla^2 T, \tag{4.3}$$

with $T$ the space- and time-dependent temperature, and $D$ the thermal diffusivity, which can be written as:

$$D = \frac{\lambda}{c_p \cdot \rho}, \tag{4.4}$$

with $\lambda$ the thermal conductivity, $c_p$ specific heat per mass and $\rho$ the mass density of the material.

One can also express the thermal diffusivity $D$ in the following way:

$$D = F_0 \cdot u^2 \cdot \tau_0 = F_0 \cdot u \cdot \Lambda_{ph}, \tag{4.5}$$

with $u$ the speed of phonons between collisions, $\tau_0$ the so called scattering time and $\Lambda_{ph}$ the phonon mean free path. The time $\tau_0$ is the average time between collisions that restore thermal equilibrium. $\Lambda_{ph}$ is the average distance a phonon travels between two scattering events. $F_0$ is a dimensionless geometrical pre-factor. It is equal to 1 for 1D, 1/2 for 2D and 1/3 for 3D geometry.

While $\lambda$ defines how well the material conducts heat under stationary conditions, $D$ defines the efficiency of the diffusion, in other words - how fast will the heat travel through the material and how fast the thermal equilibrium will be reached.

### 4.2.2 Characteristic time and length scales

Within the solutions of the diffusion equation (see Equation 4.3) one can speak of the characteristic length and time scales.

The characteristic length $L_{th}$ is defined as [108]:

$$L_{th} = \sqrt{\frac{D}{\omega}}. \tag{4.6}$$

The characteristic length is the distance from the heat source, at which the original heat flux $q(x = 0)$ is reduced by the factor $\exp(1)$. It is also called the thermal penetration depth or the thermal diffusion length [108, 109].

Through $L_{th}$ one can also define the characteristic time $\tau_D$, also called the diffusion time [108]:

$$\tau_D = \frac{L_{th}^2}{D}. \tag{4.7}$$

In this chapter we mention many different time scales, only several of which are explained in this section. One can see an overview of all different symbols and definitions in Table 4.1.

### 4.2.3 1D diffusion equation solution for 2 materials

Using a harmonic heating source to measure thermal conductivity and thermal diffusivity of the specimen is the basis of the $3\omega$ method. Yet for small specimen, like 2D material flakes, which can not be isolated from the environment effectively due to their size and small thickness, a solution that takes into account only one material is not enough. One always needs to also put the substrate material into the equation.

For that purpose we asked our theoretician Denis Kochan to develop a solution for a 1D diffusion equation with a harmonic source and two materials. The first material represents the specimen, in our case a h-BN flake, and the second material represents the substrate on which the specimen is suspended, in our case a SiN membrane. The two materials are in series: the heat travels through the suspended flake and then through the substrate.

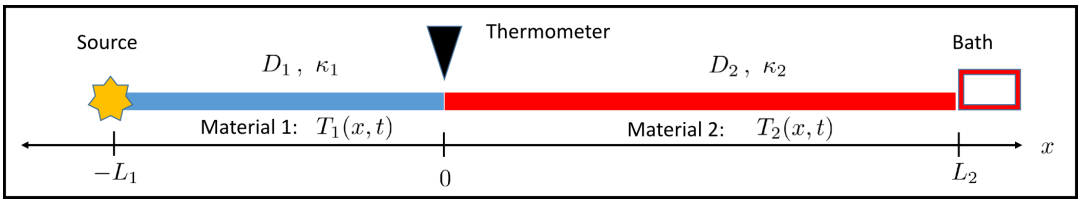


FIGURE 4.1: Schematic illustration of the model geometry. The first and second material in series are joined at $x = 0$, extending towards $x = -L_1$ and $x = L_2$ respectively. The heat flow comes from $x = -L_1$ and the bath temperature is reached at $x = L_2$. The thermometer is at $x = 0$. Each material is defined by its sheet conductance $\kappa_i$ and its thermal diffusivity $D_i$.

In Figure 4.1 one can see a sketch of the geometry. The coordinate system puts the thermometer at $x = 0$, the heater at $x = -L_1$ and the boundary of the substrate at $x = L_2$, presuming bath temperature $T(x, t) = T_{bath}$ there. This way the size (along the heat flow) of the suspended flake will be equal to $L_1$ and the size of the substrate will be equal to $L_2$.

TABLE 4.1: A list of all different time scales, their symbols and meanings in this chapter, in order of appearance.

| Symbol | Name | Definition |
|---|---|---|
| $\tau_0$ (See Equation 4.5) | Scattering time | Average time between collisions. |
| $\tau_D$ (See Equation 4.7) | Diffusion time | Time the heat flow travels over the distance of the thermal penetration depth $L_{th}$. |
| $\tau$ (See Equation 4.24) | Thermal RC-time | Time it takes to heat up the heater and the strip of the material (in our case h-BN) right below the heater. |
| $\tau_{th}$ (See Equation 4.30) | Thermal cut-off time | The inverse of the thermal cut-off frequency, the frequency at which $\Delta T_h$ starts to go to zero. |
| $t_0$ (See Equation 4.38) | - | The average time it takes for the temperature increase to travel from the heater to the thermometer at the edge of the slit in our samples. |
| $\tau_{kink}$ (See Equation 4.55) | - | The time delay caused by the kink in the 2D flake at the edge of the slit. Thermal RC-time of the kink. |
| $\tau_{R_c}$ (See Equation 4.66) | - | The time delay caused by the thermal contact resistance $R_c$. Thermal RC-time of the thermal contact resistance. |

Each of the two materials in the model is defined by two properties: the thermal conductance times length $\kappa$ and the thermal diffusivity $D$. From $\kappa$ one can calculate the thermal conductivity $\lambda$ of the material:

$$\kappa = \lambda \cdot l_{mat} \cdot t_{mat}, \tag{4.8}$$

with $\lambda$ the thermal conductivity of the material and $l_{mat}$ and $t_{mat}$ the length (orthogonal to the heat flow) and the thickness of the material respectively.

The temperature at the heater $T(x = -L_1, t)$ is defined as:

$$T(x = -L_1, t) = T_{bath} + \Delta T_{av} + \Delta T_h \cdot cos(2\omega t), \tag{4.9}$$

with $T(x = -L_1, t)$ the temperature at the heater, where $x = -L_1$, $T_{bath}$ the bath temperature, $\Delta T_{av}$ the time-independent temperature increase due to Joule heating and $\Delta T_h$ the amplitude of the time-dependent temperature increase.

Using the measured temperature rise at the thermometer $\Delta T_h$, we can obtain both the phase difference between the thermometer and the heater $\Delta\phi$ and the temperature increase at the thermometer $\Delta T_{th}$:

$$\Delta\phi = \arctan\left[\frac{\frac{\kappa_1}{L_1}\cdot M_-(\epsilon_1)+\frac{\kappa_2}{L_2}\cdot M_-(\epsilon_2)}{\frac{\kappa_1}{L_1}\cdot M_+(\epsilon_1)+\frac{\kappa_2}{L_2}\cdot M_+(\epsilon_2)}\right] - \arctan\left[\frac{N_-(\epsilon_1)}{N_+(\epsilon_1)}\right], \tag{4.10}$$

$$\Delta T_{th} = \frac{\kappa_1}{L_1}\cdot\Delta T_h \cdot \frac{N_+(\epsilon_1)\cos(\Delta\phi) - N_-(\epsilon_1)\cos(\Delta\phi)}{\frac{\kappa_1}{L_1}\cdot M_+(\epsilon_1)+\frac{\kappa_2}{L_2}\cdot M_+(\epsilon_2)}, \tag{4.11}$$

with $\Delta\phi$ the phase difference between the heater and the thermometer, $\kappa_1$ and $\kappa_2$ the thermal conductance times length of the 1st and 2nd materials respectively, $L_1$ and $L_2$ the lengths of the two materials along the heat flow and $\Delta T_h$ the temperature increase at the heater.

The dimensionless quantities $\epsilon_i$, $M_\pm(\epsilon_i)$ and $N_\pm(\epsilon_i)$ are defined in the following way:

$$\epsilon_i = \sqrt{\frac{\omega\cdot(L_i)^2}{D_i}} = \sqrt{\omega\cdot\tau_{D,i}}, \tag{4.12}$$

$$M_\pm(\epsilon) = \epsilon\cdot\frac{\sinh(2\epsilon)\pm\sin(2\epsilon)}{\cosh(2\epsilon)-\cos(2\epsilon)}, \tag{4.13}$$

$$N_\pm(\epsilon) = 2\epsilon\cdot\frac{\cos(\epsilon)\sinh(\epsilon)\pm\cosh(\epsilon)\sin(\epsilon)}{\cosh(2\epsilon)-\cos(2\epsilon)}, \tag{4.14}$$

with $D_i$ the thermal diffusivity of the corresponding material, $L_i$ the length of that material (along the heat flow), $\tau_{D,i}$ the diffusion time of the material and $\omega$ the angular modulation frequency.

This analytical solution was checked against numerical 1D simulation using COMSOL, and was in perfect agreement with the simulation.

## 4.3 3ω method

The basis of our new measurement technique is the 3ω method, that was first introduced by D. Cahill and R. Pohl in 1986 [110]. The method allows to measure thermal conductivity and diffusivity of a material with high precision and for a big range of temperatures using a harmonic heat source. There are several geometries (1D, 2D and 3D) and corresponding models that allow to use this method for different sample configurations. Yet, all of them require at least one of the measured specimen dimensions to be sufficiently big to ensure the boundary condition of $T(x,t) = T_{bath}$ at the edge of the measured material. The 3ω method is designed to measure only one material at a time, and does not allow to separate the thermal properties of two different materials if they are measured simultaneously, parallel or in series.

Due to this limitation it is not possible to measure the 2D materials with the original method. The small thickness of the 2D flakes does not allow to suspend a big enough region to ensure the boundary condition ($T(x,t) = T_{bath}$) at the edge of the flake. Therefore even the 1D approach to the 3ω method cannot describe a system with a small suspended 2D flake and the substrate accurately.

In this section we will discuss two topics: the general working principle of the 3ω method and its 1D approach and why the original method is not applicable for our samples. We will not discuss the 3D model [93, 110] of the 3ω method, since it is not applicable to two-dimensional systems. Details on the 2D model [111] can be read in Appendix D.

### 4.3.1 General principle

To measure the thermal properties of a material, one puts a narrow and thin metal strip on top of the material, making sure that there is no electrical short between the two, but a good thermal contact is present.

The metal strip, a so called transducer, will act as both a heater and a thermometer in the measurement. By sending a high AC current through the transducer, it will generate heat and send it through the material. On the other hand, its change of electrical resistance due to the temperature increase will allow to probe the temperature difference in the material below the strip, using the strip as a thermometer.

The electrical current $I_h$ that is send through the heater oscillates with a certain angular frequency $\omega$:

$$I_h(t) = I_0 \cdot \cos(\omega t). \tag{4.15}$$

If the heater has the resistance $R_h$, then the power dissipated inside the heater will then be:

$$P_h(t) = I_h^2 \cdot R_h = \frac{{I_0}^2 \cdot R_h}{2} \cdot (1 + \cos(2\omega t)). \tag{4.16}$$

For low powers the temperature difference is proportional to the dissipated power [96] and therefore the heater temperature will be the sum of the bath temperature $T_{bath}$, an average temperature difference $\Delta T_{av}$ due to Joule heating and an oscillating component $\Delta T_h$:

$$T_h(t) = T_{bath} + \Delta T_{av} + \Delta T_h \cdot \cos(2\omega t). \tag{4.17}$$

For small frequencies the two temperature differences become equal ($\Delta T_{av} = \Delta T_h$).

Since we can write the electrical resistance of the heater in the following way:

$$R_h(t) = \frac{dR_h}{dT_h} \cdot T_h(t), \tag{4.18}$$

we can write:

$$\begin{aligned} R_h(t) &= R_0(T_{bath}) + \frac{dR_h}{dT_h} \cdot [\Delta T_{av} + \Delta T_h \cdot \cos(2\omega t)] \\ &= R_0(T_{bath}) + \frac{dR_h}{dT_h} \cdot \Delta T_{av} + \frac{dR_h}{dT_h} \cdot \Delta T_h \cdot \cos(2\omega t) \\ &= R_0 + \Delta R_{av} + \Delta R_h \cdot \cos(2\omega t). \end{aligned} \tag{4.19}$$

This shows us, that also the resistance of the heater will have a DC-part $R_0 + \Delta R_{av}$ and an AC-part $\Delta R_h$. If we then calculate the voltage drop $V_h(t)$ over the heater, we can write:

$$\begin{aligned} V_h(t) &= R_h(t) \cdot I_h(t) \\ &= (R_0 + \Delta R_{av}) \cdot I_0 \cdot \cos(\omega t) + \frac{\Delta R_h \cdot I_0}{2} \cdot [cos(3\omega t) + \cos(\omega t)]. \end{aligned} \tag{4.20}$$

The last line shows that the measured voltage drop over the heater will have a component that will oscillate with a frequency $3\omega$ and the following amplitude:

$$V_{3\omega} = \frac{\Delta R_h \cdot I_0}{2} = \frac{dR_h}{dT_h} \cdot \frac{\Delta T_h \cdot I_0}{2}, \tag{4.21}$$

therefore, if one measures $V_{3\omega}$, one can calculate the temperature difference $\Delta T_h$ at the heater.

### 4.3.2 1D geometry

A 1D model was proposed in a paper by Sikora et al. in 2012 [95]. There they used thin, elongated membranes. Since the width to length ratio ($b_{mem}/l_{mem} < 0.1$) is small for those membranes, the edge effects affect only a small part of the heat flow profile and can be neglected. This justifies the 1D approach.

Figure 4.2 shows the schematic of a typical geometry used by Sikora and his colleagues for their measurements. A metal heater with width $b_h$ and thickness $t_h$ is deposited on a thin membrane with length $l_{mem}$ (along the heater), width $b_{mem}$ (orthogonal to the heater) and thickness $t_{mem}$. The heater is as long as the membrane ($l_h = l_{mem}$).

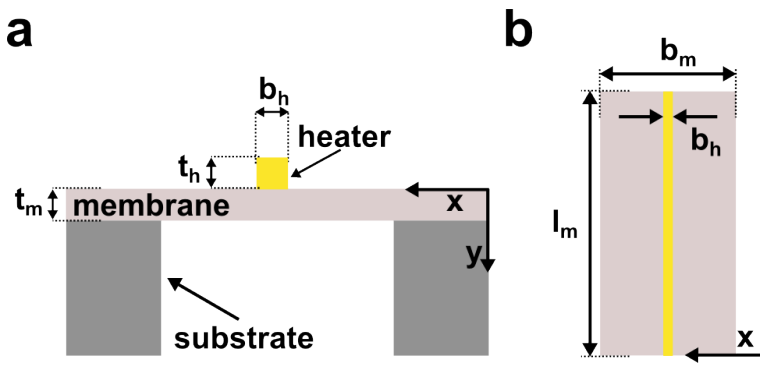


FIGURE 4.2: Schematic side (a) and top view (b) of the sample. The heater line of length $l_{mem}$, thickness $t_h$ and width $b_h$ crosses the suspended membrane in the middle of thickness $t_{mem}$, $b_{mem}/2$ distance away from the border of the membrane.

Sikora et al. derived the following expression for the temperature difference at the heater $\Delta T_h$:

$$\Delta T_h = \frac{1}{4 \cdot K_{mem}} \frac{V_s^2 \cdot R_1 \cdot R_h}{(R_h + R_1)^3} \cdot \frac{1}{\left[1 + \omega^2 \left( \underbrace{4 \cdot \tau^2 + \frac{(b_{mem})^4}{12 \cdot D^2} + \frac{\tau \cdot (b_{mem})^2}{3D}}_{\tau_{th}^2} \right)\right]^{1/2}}, \tag{4.22}$$

with $R_1$ a constant resistance in the Wheatstone bridge, $R_h$ the resistance of the heater, $V_s$ the applied source voltage and $K_{mem}$ being the thermal conductance of the membrane, defined as:

$$K_{mem} = \frac{\lambda_{mem} \cdot t_{mem} \cdot l_{mem}}{b_{mem}}, \tag{4.23}$$

and $\tau$ being the time it takes to heat the heater and the strip below it to a certain temperature difference $\Delta T_h$, defined as:

$$\tau = \frac{1}{2} \cdot \frac{C' \cdot b_{mem}}{\lambda_{mem} \cdot t_{mem} \cdot l_h} = \frac{1}{2} \cdot \frac{C'}{K_{mem}}, \tag{4.24}$$

with $\lambda_{mem}$ the thermal conductivity of the membrane. $b_{mem}$ the width of the membrane, $t_{mem}$ the thickness of the membrane and $l_{mem}$ the length of the membrane. $C'$ is the combined heat capacity of the heater and the membrane strip right below the heater, defined as:

$$C' = \rho_h \cdot c_h \cdot l_{mem} \cdot t_h \cdot \frac{b_h}{2} + \rho_{mem} \cdot c_{mem} \cdot l_{mem} \cdot t_{mem} \cdot \frac{b_h}{2} = \frac{C'_h + C'_{st}}{2}, \tag{4.25}$$

with $\rho_h$ the density of the heater material, $c_h$ the specific heat per mass of the heater material, $\rho_{mem}$ the mass density of the membrane, $c_{mem}$ the specific heat per mass of the membrane, $t_h$ the thickness of the heater and $b_h$ the width of the heater. $l_{mem}$ is the length of the membrane, the same as the length of the heater. $C'_h$ is the heat capacity of the heater and $C'_{st}$ is the heat capacity of the membrane strip right below the heater.

Using Equation 4.22 one can fit the measured temperature difference at the heater $\Delta T_h$ and obtain the thermal conductivity from using the low frequency range, where the signal is relatively constant. In Figure 4.3 one can see an example of such a measurement and the corresponding fit, showing a constant signal up to a certain critical frequency (≈ 3 Hz), when the signal starts to go to zero.

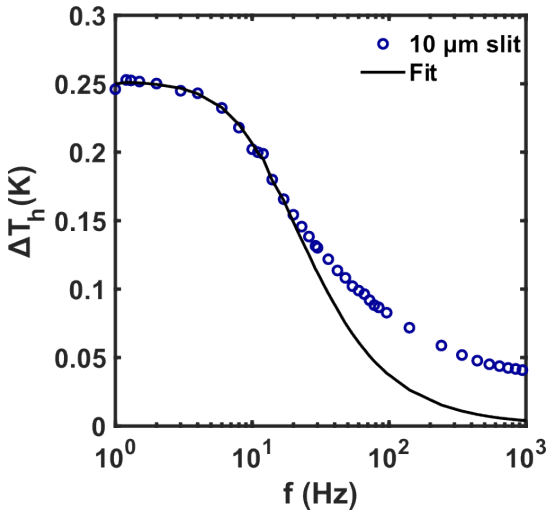


FIGURE 4.3: An example of a typical $\Delta T_h$ as function of the frequency curve. The low-frequency regime (1 Hz till 3 Hz) shows a constant behavior, while after the thermal cutoff (≈ 3 Hz) the $\Delta T_h$ goes to zero. The data shown (blue hollow circles) is measured for a suspended h-BN flake, the 10 µm slit sample, at bath temperature of 210 K. The fit (black line) is calculated with Equation 4.22, using as parameters $\lambda_{hBN}$ = 8.7 W m$^{-1}$ K$^{-1}$ and $\tau_{th}$ = 8.9 ms.

Equation 4.22 can also partly fit the tail of the $\Delta T_h$ signal curve, which allows to obtain the thermal diffusivity of the material, once we have a value for the thermal conductivity.

We define three parameters $Y_1$, $Y_2$ and $\tau_{th}^2$ in the following way:

$$Y_1 = \rho_h \cdot c_h \cdot t_h, \tag{4.26}$$

$$Y_2 = \frac{b_{mem} \cdot b_h}{4 \cdot \lambda_{mem} \cdot t_h}, \tag{4.27}$$

$$\tau_{th}^2 = 4 \cdot \tau^2 + \frac{(b_{mem})^4}{12 \cdot D^2} + \frac{\tau \cdot (b_{mem})^2}{3D}. \tag{4.28}$$

The value $\tau_{th}^2$ in Equation 4.28 serves as a second fitting parameter in Equation 4.22, as a multiplying factor in the last fraction. It defines how fast $\Delta T_h$ decays with the frequency, while $\lambda_{mem}$ is simply an overall prefactor. $\tau_{th}$ is the thermal cut-off time, the inverse of the critical cut-off frequency, when $\Delta T_h$ starts to go to zero (see Figure 4.3). By fitting the measured $\Delta T_h$ (see Figure 4.3), one can obtain both $\lambda_{mem}$ and $\tau_{th}^2$.

Then we can plug $Y_1$ and $Y_2$ into Equation 4.24 and write it as:

$$\tau(D, \lambda) = Y_1 \cdot \left( Y_2 + \frac{\lambda_{mem} \cdot t_{mem}}{D} \right). \tag{4.29}$$

By doing that, we can also write $\tau_{th}^2 \cdot D$ in the following way:

$$\begin{aligned} &\tau_{th}^2 \cdot D^2 = D^2 [2 Y_1 Y_2]^2 + \\ &+ D \left[ 4 Y_1 Y_2 \cdot \left( 2 \cdot Y_2 \cdot \lambda_{mem} \cdot t_{mem} + \frac{(b_{mem})^2}{12} \right) \right] + \\ &+ \left[ 4 \cdot (Y_2 \cdot \lambda_{mem} \cdot t_{mem})^2 + \frac{(b_{mem})^4}{24} + \frac{Y_2 \cdot \lambda_{mem} \cdot t_{mem} \cdot (b_{mem})^2}{3} \right]. \end{aligned} \tag{4.30}$$

As you can see, Equation 4.30 is a quadratic equation in $D$. Solving it and taking the positive solution will yield a value for the thermal diffusivity $D$.

Despite being a good model for big suspended membranes, like $Si_3N_4$, the 1D solution proposed by Sikora et al. [95] does not describe accurately small suspended 2D flakes. The value for thermal conductivity $\lambda$ that we can obtain using Equation 4.3 to fit our data in Figure 4.3 would be 8.7 W $m^{-1}$ $K^{-1}$, which is an order of magnitude lower than the values in literature for few-layer h-BN [32] and higher than the literature values of thermal conductivity for the SiN membranes [112]. Similarly, values in the order of 10 $Wm^{-1}K^{-1}$ are obtained for all our samples and bath temperatures. This shows that the 1D model proposed by Sikora et al. is not reliable in case of small specimen. In our case it predicts a mixed thermal conductivity, which is dependent both on the conductivity of the flake and the substrate.

## 4.4 Adaptation of the 3ω method for few-layer flakes

As mentioned in the previous section, we have encountered several difficulties while trying to measure our samples with the method proposed by Sikora et al. [95]. Our sample design puts the suspended h-BN flake in series with the $Si_3N_4$ membrane on which the flake is suspended. This creates a system of two materials, rather than only one, and the 3ω method is designed to measure only one material at a time. The boundary condition assumes that at the edge of this one material the temperature $T(x, t)$ is equal to $T_{bath}$, which is not the case with the edge of the h-BN flake.

This problem can be solved in one of the two standard ways:

The first solution is to increase the size of the material of interest, in our case the h-BN flake. With a big enough area one could ensure that only a negligible part of

the temperature drop would happen outside of the suspended flake. Unfortunately the small thickness of the few-layer flakes (5-12 nm) does not allow the flakes to be suspended over an area bigger than 100-150 $\mu m^2$. A flake with a bigger suspended area would either become very distorted or collapse due to the tension. The biggest suspended area in our samples is 100 $\mu m^2$ (10 by 10 µm) and we were not able to suspend a bigger area without breaking or distorting the flake. According to our measurements 30% of the temperature drop still happens outside of the flake. This means that we cannot avoid to take the substrate into account when modeling our measurements.

The second solution is to measure the substrate prior to putting the material of interest on top of the substrate. That way one can perform two separate measurements: one with the substrate only and one with both the substrate and the h-BN flake. Using the obtained thermal conductivity of the substrate from the first measurement one could obtain the h-BN thermal conductivity from the second measurement, which would give a mixed thermal conductivity. For us this solution does not work for two reasons. Firstly, because this method requires to put the heater on top of the substrate before stamping the flake. Even if we would refrain from suspending the flake and would measure a supported flake, with the heater being 40 nm thick and the h-BN flakes being 5-12 nm thick, stamping a flake on top of a heater four times thicker than the flake would create a significant bending and distortion in the flake. Secondly, this method only allows to extract the thermal conductivity of h-BN, but not the thermal diffusivity. With h-BN and the substrate being in series, the slower material will completely dominate the time response, making it hard to separate the thermal diffusivities of the two materials.

Not being able to use either of the two standard solutions to this problem, we have come up with our own solution. We have introduced a reference thermometer at the edge of the suspended part of the flake. This allows us to measure the temperature drop over the flake only. This also allows us to use the phase shift between the measured temperature increase at the heater and at the thermometer to estimate the time it takes the heat to travel the distance between the heater and thermometer. From those numbers we expect to determine the thermal diffusivity of the flake.

Additionally, we use a new analytical solution derived by Denis Kochan of the 1D diffusion equation (see Section 4.2.3). This one differs from the one introduced by Sikora et al. [95]: we solve for both the flake and the substrate in series, rather than only for the flake. This way we can take into account both the 2D flake and the substrate on which it is suspended.

### 4.4.1 Reference thermometers

We use a thermometer to measure the temperature difference $\Delta T_{th}$ a certain distance away from the heater. To do that one can apply a DC probing current $I_t$ to the thermometer. Since the thermometer will be heated by the main heater, it will still have a frequency dependent resistance modulation $\Delta R_t$ on top of its normal resistance $R_{t0}$ due to the temperature increase:

$$R_t(t) = R_{t0}(T_{bath}) + \Delta R_{t,av} + \Delta R_t \cdot \cos(2\omega t + \Delta\phi), \tag{4.31}$$

with $R_t(t)$ the time-dependent resistance of the thermometer, $R_{t0}$ the resistance of the thermometer at bath temperature without heating, $\Delta R_{t,av}$ the time-independent resistance increase due to Joule heating, $\Delta R_t$ the time-dependent resistance increase,

$\omega$ the modulation frequency and $\Delta\phi$ the phase shift between the temperature modulation $\Delta T_{th}(t)$ of the thermometer and the temperature modulation $\Delta T_h(t)$ at the heater.

Part of the voltage drop over the thermometer $V_t$ will be also proportional to $2\omega$, since the current $I_t$ through the thermometer is not frequency dependent:

$$V_t(t) = I_t \cdot R_t(t) = I_t \cdot (R_{t0} + \Delta R_{t,av}) + I_t \cdot \Delta R_t \cdot \cos(2\omega t + \Delta\phi). \tag{4.32}$$

From this frequency dependent part we can calculate $\Delta T_{th}$:

$$\Delta T_{th} = \left(\frac{dR_t}{dT_{th}}\right)^{-1} \cdot \Delta R_t = \left(\frac{dR_t}{dT_{th}}\right)^{-1} \cdot \frac{V_{t,2\omega}}{I_t}, \tag{4.33}$$

with $\Delta T_{th}$ the temperature increase at the thermometer, $V_{t,2\omega}$ the second harmonic of the voltage drop over the thermometer $V_t$ and $l_t$ the length of the thermometer.

### 4.4.2 Thermal conductivity

We use Fourier's law 4.1 to extract the thermal conductivity from our measurements. By keeping the applied power low, we can ensure that the linearity of the temperature increase is valid and obtain the thermal conductivity in the following way:

$$\lambda_{flake} = \frac{P \cdot b_{flake}}{2 \cdot \Delta T_{h-t} \cdot l_{flake} \cdot t_{flake}}, \tag{4.34}$$

with $\lambda_{flake}$ the thermal conductivity of the flake, $P$ the applied power, $\Delta T_{h-t}$ the temperature drop between heater and thermometer (therefore excluding the substrate) and $l_{flake}$, $b_{flake}$ and $t_{flake}$ the length, width and thickness of the flake respectively, as defined in Figure 4.2.

We confirm the values obtained this way using our 1D diffusion model (see Section 4.2.3).

### 4.4.3 Thermal diffusivity

Since we are sending an AC current through our heater, according to Equation 4.17, we can write $\Delta T_h$ in the following way:

$$\Delta T_h(\omega) = \Delta T_0 \cdot cos(2\omega t). \tag{4.35}$$

Then if there is a phase difference between the heater and thermometer, it is logical to write $\Delta T_{th}$ in a similar way:

$$\Delta T_{th}(\omega) = \Delta T_0^* \cdot cos(2\omega t + \Delta\phi), \tag{4.36}$$

with the phase shift $\Delta\phi$ expressed in terms of a time delay $t_0$ in the following way:

$$\Delta\phi(\omega) = 2\omega t_0 = 4\pi f t_0, \tag{4.37}$$

with $t_0$ the average time it takes for the change in temperature to propagate from the heater to the thermometer. By fitting the $\Delta\phi$ as function of frequency linearly we can obtain this value:

$$t_0 = \frac{\Delta\phi}{4\pi f}. \tag{4.38}$$

Since we know the exact distance between the heater and the thermometer $b_{flake}/2$, and we know the time $t_0$ it takes for the heat to cross it, we are now able to calculate the thermal diffusivity $D$ using Equation 4.7 under the assumption that $t_0 \approx \tau_D$. This assumption is justified by the 1D model (see Section 4.2.3 and Equations 4.10 and 4.11). We can then write $D$ in the following way:

$$D = \frac{b_{flake}^2}{4t_0}, \tag{4.39}$$

with $D$ the thermal diffusivity, $b_{flake}/2$ the distance between the heater and the thermometer and $t_0$ the time heat needs to travel that distance.

## 4.5 Sample characterization and setup

### 4.5.1 Sample Fabrication

In order to measure thermal properties of our h-BN flakes, the flake has to be suspended, to isolate it from the substrate, and a heater is deposited on top of the flake to perform the $3\omega$ measurement.

This section describes the sequence of the fabrication steps. First, we prepare the substrate on which the 2D flakes will be suspended, a $Si_3N_4$ membrane, by etching a hole in it using e-beam lithography and reactive ion etching (RIE). After that we exfoliate and stamp a few-layer h-BN flake on top of the substrate using the all-dry PDMS stamping method [41]. Finally, we deposit a metal heater on top of the flake using e-beam lithography and thermal evaporation.

#### 4.5.1.1 Substrate

As a substrate for our flakes we use low-stress $Si_3N_4$ membranes. In Figure 4.4 one sees the schematics of the side and top view (Figures 4.4a and 4.4b) and an optical image of such a membrane (Figure 4.4c). Those substrates consist of a 200 µm thick silicon frame, on top of which a layer of 200 nm thick $Si_3N_4$ is grown. The frame is circular, 3 mm in diameter. By using chemical etching, part of the silicon frame is removed, leaving a square of 500 by 500 µm of $Si_3N_4$ suspended. All membranes are ordered from Ted Pella inc. (product number 21520). The small thickness of 200 nm is chosen deliberately: we have noticed, that when the $Si_3N_4$ membranes are thicker (500 nm), the suspended flake is pulled by van der Waals forces into the slit. When using thinner $Si_3N_4$ membranes (200 nm), this does not happen.

After cleaning the substrate in acetone and isopropanol, we pattern it with a set of eight optical markers. Figure 4.5 shows an optical image of a membrane patterned with such markers. Four bigger markers are placed right outside of the membrane and are used for general alignment during e-beam lithography. Four smaller markers are written inside the membrane, and are used for a second, more precise alignment procedure. This design allows us to limit the exposure of the smaller markers and therefore avoid destroying them during the etching step. The markers are made using e-beam lithography and Ti/Au evaporation and are 35 nm thick (5 nm Ti sticking layer and 30 nm Au).

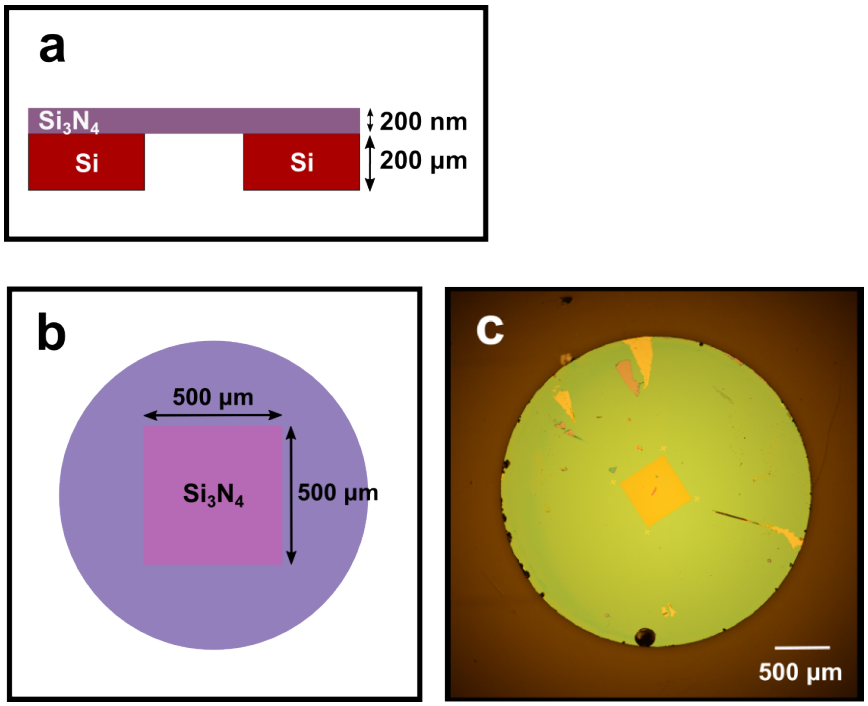


FIGURE 4.4: An example of a pre-made substrate we used to fabricate our devices. (a) A schematic side view of the substrate. (b) A schematic top view of the substrate. (c) Optical image of one of our samples, with a 5x magnification.

Once we have patterned the substrate with the optical markers, we write a slit in the middle of the small marker field using e-beam lithography. We have used four different slit dimensions for our samples: 2 by 20 µm, 5 by 5 µm, 7 by 7 µm and 10 by 10 µm. Those slit dimensions were chosen as an optimum between the needed sample size to observe diffusive thermal transport in the flakes and the average distance over which we could suspend our flakes, without breaking them during fabrication. To make sure the rest of the membrane would not become affected by the etching, we use three layers of e-beam resist (200k 9%) for this lithography step. The slit is then created using reactive ion etching (5 ccm $O_2$ and 50 ccm $CHF_3$).

After etching we leave the sample for one night in warm acetone (at 60 °C) and then clean it for 1 minute in oxygen plasma. The last step is to remove the residues of cross-linked PMMA. After that the sample is ready for stamping.

We exfoliate and transfer the h-BN flake using the dry viscoelastic transfer method [41]. This process is described in detail in Chapter 2. We use the hexagonal boron nitride crystals from Taniguchi and Watanabe [113], which allow us to exfoliate high quality thin flakes with a relatively big surface area.

#### 4.5.1.2 Annealing

As our practice showed, an annealing step is necessary right after stamping to make sure the flake will not shift during spincoating of the resist. Therefore we bake our samples for 10 minutes at 300 °C in air, to make sure the h-BN flake properly relaxes onto the surface, increasing the adhesion, and to remove any water or air bubbles between the flake and the substrate.

After baking the $Si_3N_4$ membranes usually show hydrophobic behavior, which is highly problematic when one needs to spincoat liquid resist, since the resist would

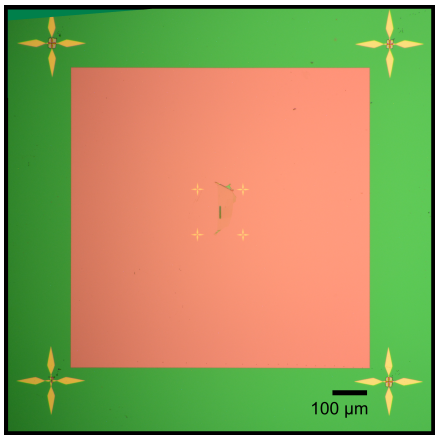


FIGURE 4.5: An optical image showing a $Si_3N_4$ membrane patterned with 8 optical markers.

not stick to the surface. We solve this by putting the sample for 20 seconds in oxygen plasma.

#### 4.5.1.3 Heater and thermometers

As the last fabrication step we write and deposit three metal strips on top of our flake, that will serve as the heater and two thermometers for our modified 3ω measurement. By using the optical markers, we can achieve at least 100 nm precise alignment, making sure that the heater is written in the middle of the slit and the thermometers at the slit's edge. We write two thermometers, on both sides of the slit, rather than just one, because of a high risk of at least one thermometer breaking during lift-off. Despite all the precaution it is still a delicate and risky fabrication procedure, and patterning two thermometers increases the chances of having a working device.

The strip is 33 µm long for the heater and 22 µm long for the thermometers, 100 nm wide and 40 nm thick. The width has been chosen as the minimum possible to still obtain a sufficiently homogeneous cross section. The heater thickness is the minimum at which we could make sure the heater will cross over the flake without developing cracks on the edges. The metal strip consists of 10 nm titanium sticking layer and 30 nm of gold.

Figure 4.6a shows a schematic side view of a finished device and Figure 4.6b shows a schematic top view.

More details on the fabrication procedure can be found in Appendix C.

### 4.5.2 Measurement Setup

Once we have finished our sample, we bond it to the chip carrier and mount it in our flow cryostat, to perform the measurements. This section describes all the parts of our measurement setup in detail.

#### 4.5.2.1 Chip carrier and bonding

For our flow cryostat (see subsection 4.5.2.2) we use home-made copper chip carriers. In Figure 4.7 one can see two photos of one of those chip carriers. On the two sides are the contact pads meant for bonding, and in the middle is a copper plate with space for the sample and two screw holes. The screws are used to assure

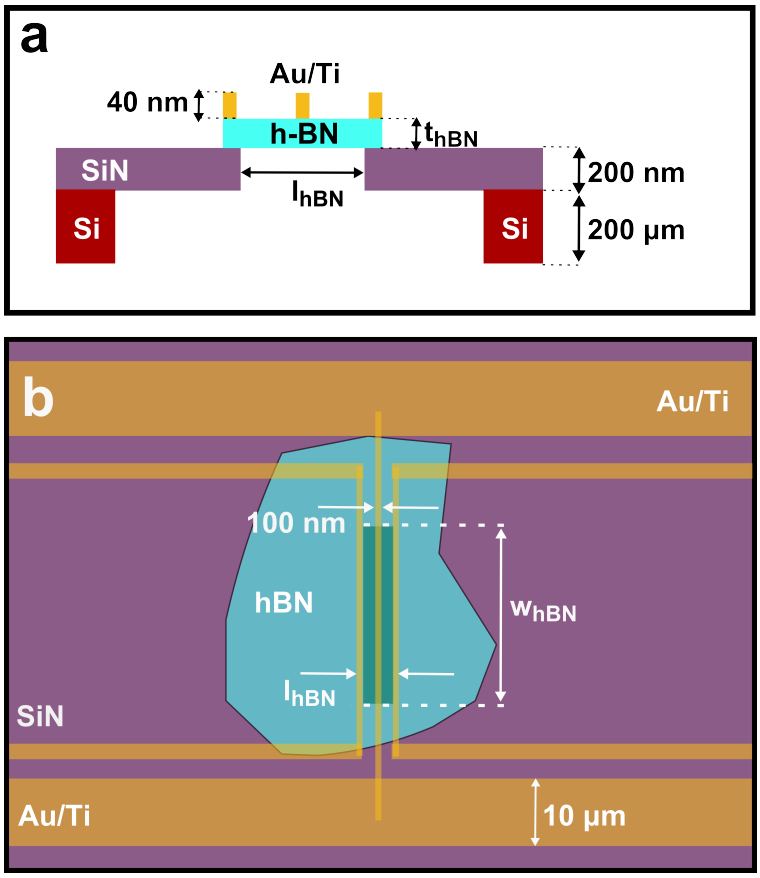


FIGURE 4.6: (a) Schematic side view of a finished sample. (b) Schematic top view of a finished sample. The width $b_{hBN}$, thickness $t_{hBN}$ and length $l_{hBN}$ of the flake vary from sample to sample.

proper thermal contact between the carrier and the cryostat, to avoid long thermalisation times. As our experience shows, without the screws it takes at least one hour to stabilize the sample after a 10 K bath temperature increase. With the screws it takes about 10 minutes.

The sample is glued in the middle with silver paint and left to dry for at least 30 minutes. This is done to again improve the thermal contact between the chip carrier and the sample chip.

Once we have made sure that the sample is properly attached to the chip carrier, we use aluminum wire to bond the contact pads on the substrate and the pads on the chip carrier. Each contact pad from the sample will be bonded by two separate bonds, to allow for a four contact measurement, if needed. During the bonding, all chip carrier pads are shorted together at the bottom, to make sure the heater will not be destroyed due to an electrical discharge.

#### 4.5.2.2 Flow cryostat

We perform all of our measurement inside a flow cryostat. In figure 4.8 one can see a schematic depiction of the cryostat. One end of the transfer line is deposited inside a liquid helium dewar and the other end is inserted inside the cryostat. A screw pump is constantly pushing liquid helium through the transfer line, through the cryostat line around the sample inside the IVC, and then into the recovery line.

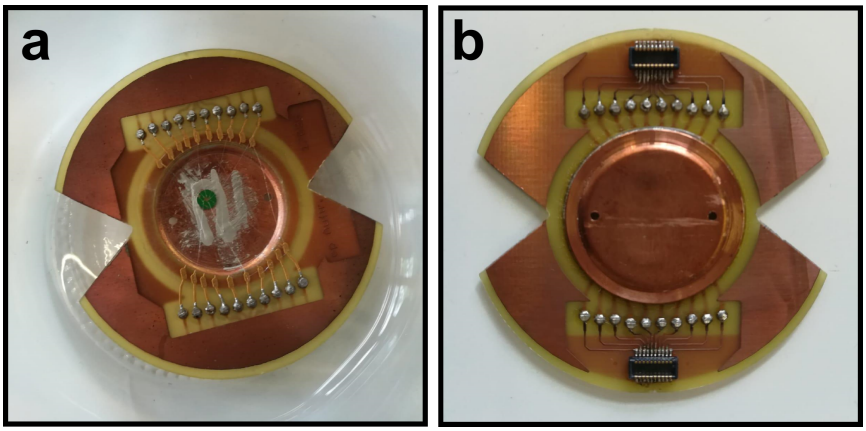


FIGURE 4.7: (a) Photo of the top side of our home-made chipcarrier, with the sample bonded. The 20 contact pads on the top and bottom side will be in contact with the cryostat lines. The sample is glued to the chipcarrier with the silverpaste and bonded to the contact pads with aluminum wires. (b) Photo of the bottom side of the chipcarrier. The black clips are used to place the chipcarrier in the IVC.

The flow can be controlled by the needle valve inside the transfer line. At the full capacity the cryostat can reach about 3 K, setting the flow to about 10-20% will allow to stabilize the temperature in the range between 30 to 300 K. In addition to the needle valve, one can adjust the bath temperature using a built-in heater, which can be set in both automatic and manual mode. The heater and the needle valve are controlled through an Oxford Instruments temperature controller, which can also be accessed through a LabView script. When the system is idle, the helium flow is turned off and the IVC is warming up back to room temperature.

The sample is screwed onto a metal platform (see Figure 4.9a), ensuring proper electrical and thermal contact. We connect the contacts of the chip carrier to the cryostat lines, which can be accessed through a BNC connector box (see Figure 4.9b). On top of the chip carrier we put a copper radiation shield, to ensure proper isolation of the sample from thermal radiation.

Once the sample has been properly mounted, the IVC is closed and pumped by a turbo pump to a pressure of at least 6e-6 mbar. The lower the pressure inside the IVC, the faster the thermalisation time during each cooldown and the lower the helium consumption during the measurement.

#### 4.5.2.3 Wheatstone bridges

To use the $3\omega$ method we need to be able to separate the first and third harmonics of the heater voltage $V_h(t)$, because usually the first harmonic component is much higher in amplitude than the third harmonic. The most used method to separate those harmonics effectively is by using a Wheatstone bridge, which allows to remove the big $V_\omega$ from the measured signal, leaving only the small $V_{3\omega}$.

Figure 4.10 shows a general schematic depiction of a Wheatstone bridge. An oscillating source voltage is applied to the bridge. The current runs from point A to point D, and divides into two branches. The first branch (through point B) contains a constant resistor $R_2$ and a variable resistor $R_v$. The second branch (through point C) contains a constant resistor $R_1$ and the resistance of interest $R_x$.

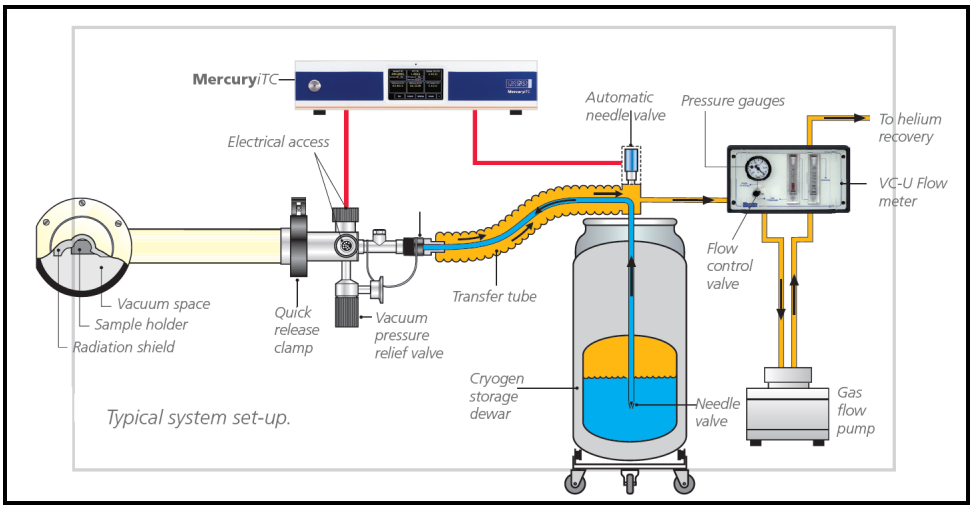


FIGURE 4.8: Schematic view of the Flow cryostat, liquid helium dewar and pumps. Liquid helium is being pumped from the dewar into the cryostat (blue flow), around the sample and into the recovery line (yellow flow). The cryostat IVC (on the left) is kept in vacuum (1e-6 mbar). Image taken from [114].

By making the drop $V_{AB}$ equal to the drop $V_{AC}$, one can balance the bridge, making the voltage $W$ (as measured from B to C) equal to zero. One should make sure that the following condition is met:

$$\frac{R_v}{R_2} = \frac{R_1}{R_x}. \tag{4.40}$$

If we balance the bridge at the beginning of the measurement, while the heater is not yet heated, then the voltage $W$ will be zero. Then, once we send the current through the heater, the resistance of the sample $R_x$ will increase by the oscillating component $\Delta R \cdot cos(2\omega t)$ (see Equation 4.19 ). This will create a small increase in the $W$, that will be proportional to the $\Delta R$.

Since in the heated state the bridge becomes unbalanced, one can now see the bridge as a voltage divider. If one measures the third harmonic of the voltage $W$, $W_{3\omega}$, one can obtain the third harmonic of the sample voltage $V_{3\omega}$ (see Equation 4.21) [115]:

$$W_{3\omega} = \frac{R_1}{R_x + R_1} \cdot V_{3\omega}. \tag{4.41}$$

This way one can obtain both the difference in resistance of the sample $\Delta R_h$ and the corresponding temperature difference $\Delta T_h$ created at the heater.

For our experiment we have build two Wheatstone bridges, first one for the heater and the second one for the thermometer. During a measurement both are used simultaneously. In both bridges, only the sample ($R_h$ and $R_t$) is inside the cryostat, all other components are outside. In each bridge we use three constant metal film resistors, two $\pi$-filters, a lock-in (Standford SR830), a resistor decade and a pre-amplifier (L1 75A NF-electronics, 100x magnification).The pre-amplifiers are powered by Li ion batteries, to reduce the noise in the system and avoid any noise coming from the power net. For variable resistors $R_{v1}$ and $R_{v2}$ we use two resistor decades (Orbit Controls, OCM642-V1000) with a range of 100 mOhm to 1 MOhm

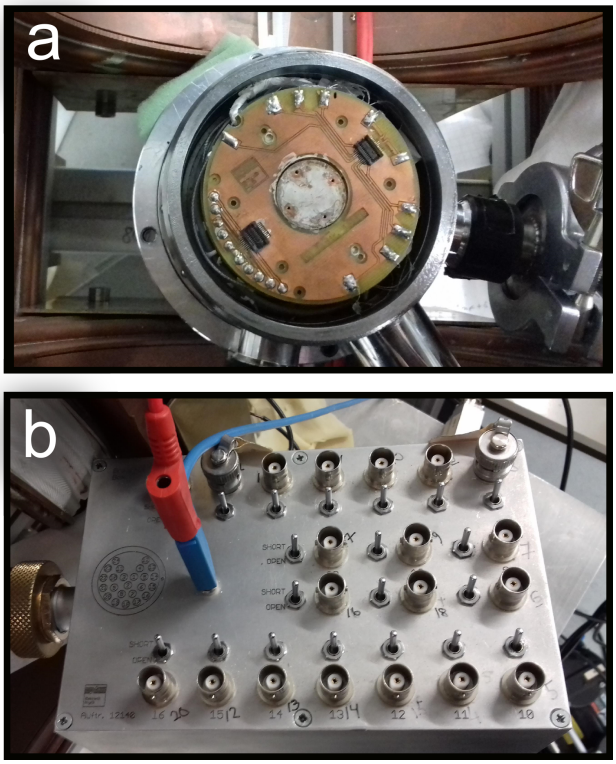


FIGURE 4.9: (a) Photo of the metal platform inside the cryostat IVC, where the chipcarrier is screwed on. The two black clips are used to contacts the 20 bonding pads on the chip carrier, and two out of the four screw holes on the platform are used to screw the chip carrier to the platform. (b) Photo of the BNC box of the flow cryostat. Each BNC connector corresponds to one of the 20 contact pads on the chip carrier. The middle banana plug is used for grounding.

and a 0.02-0.05% precision, depending on the resistance range. All bridge components are connected with coaxial BNC cables and share the same ground. In Figure 4.11 one can see a schematic depiction of the bridges' setup.

In Figure 4.11a one can see a schematic depiction of the heater bridge. The heater bridge uses the first lock-in as the voltage source. A voltage is applied to a pre-resistor (10 kΩ), goes through a π-filter and then goes to the heater bridge and divides between the two branches of the bridge. The π-filters are used to avoid high-frequency pulses reaching the sample. As our experience shows, those pulses often can destroy the heater during the measurement, therefore we use two π-filters in each bridge - before and after the sample.

One branch of the heater bridge consists of a constant resistor $R_1$ and the heater $R_h$. The other branch consists of a resistor decade $R_{v1}$ and a second constant resistor $R_2$. The lock-in measures the third harmonic of the voltage $W_1$, in this case the difference between the voltage drop over $R_h$ (point A to ground) and the voltage drop over $R_{v1}$ (point B to ground). See Figure 4.11a. Both signals are first sent through the differential input of the pre-amplifier and then go to the lock-in input of the first lock-in. The pre-amplifier is needed to improve signal-to-noise ratio and to be able to measure at small powers and stay in the linear regime without losing the quality of the measured signal.

In Figure 4.11b one can see a schematic depiction of the thermometer bridge. The thermometer bridge uses a Yokogawa (GS200) as a DC voltage source. A voltage of

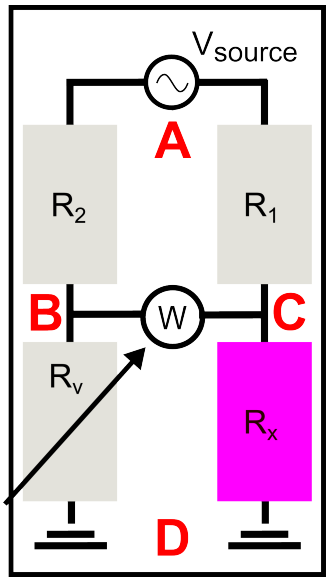


FIGURE 4.10: Schematic depiction of a Wheatstone bridge. $R_1$ and $R_2$ are constant resistors, $R_x$ is the sample and $R_v$ is a variable resistor.

1V is applied to the pre-resistor of 100 kΩ, which creates a DC current of about 10 µA. This current enters the thermometer bridge, almost identical to the heater bridge. Again, two constant resistors, $R_3$ and $R_4$, and a resistor decade, $R_{v2}$, are used together with the thermometer $R_t$. The second lock-in measures the second harmonic of the pre-amplified Wheatstone voltage of the thermometer bridge, $W_2$.

At every bath temperature, we balance both bridges. The heater bridge is balanced at a small source voltage of 10 mV (1 µA current), to avoid balancing a heated strip. Otherwise one risks to balance out part of the resistance increase $\Delta R$ caused by the temperature increase $\Delta T$. The thermometer bridge is balanced at the source voltage of 100 mV (1 µA current). Both voltages $W_1$ and $W_2$ can be balanced to about 5-20 nV in the non-heated state, depending on the noise level.

#### 4.5.2.4 Heater and thermometer calibration setup

As shown in Equation 4.21 and 4.33, we need to calibrate our heater and thermometer, to be able to convert measured voltages to temperature differences. To do that we perform two $R(T_{bath})$ measurements, measuring the resistance of both heater and thermometer as function of the bath temperature $T_{bath}$.

Figure 4.12 shows the experimental setup for such a measurement. One lock-in is used as a voltage source, applying 100 mV to a pre-resistor of 100 kOhm. This creates a current of approximately 1 µA, which will pass through the measured metal strip $R_{strip}$ (either $R_h$ or $R_t$). The voltage drop over the heater/thermometer is measured with a differential input of the pre-amplifier and the first lock-in. The current through the heater/thermometer goes through the second lock-in and then to ground. Again we use two π-filters to avoid high frequency pulses. The first lock-in measures the amplified voltage drop over the metal strip and the second lock-in the current through the strip, allowing us to extract the four-contact resistance of the heater/thermometer. We measure in steps of 1 K, from 30 to 300 K. For each bath temperature 10 minutes are given for thermalisation, before the measurement is started.

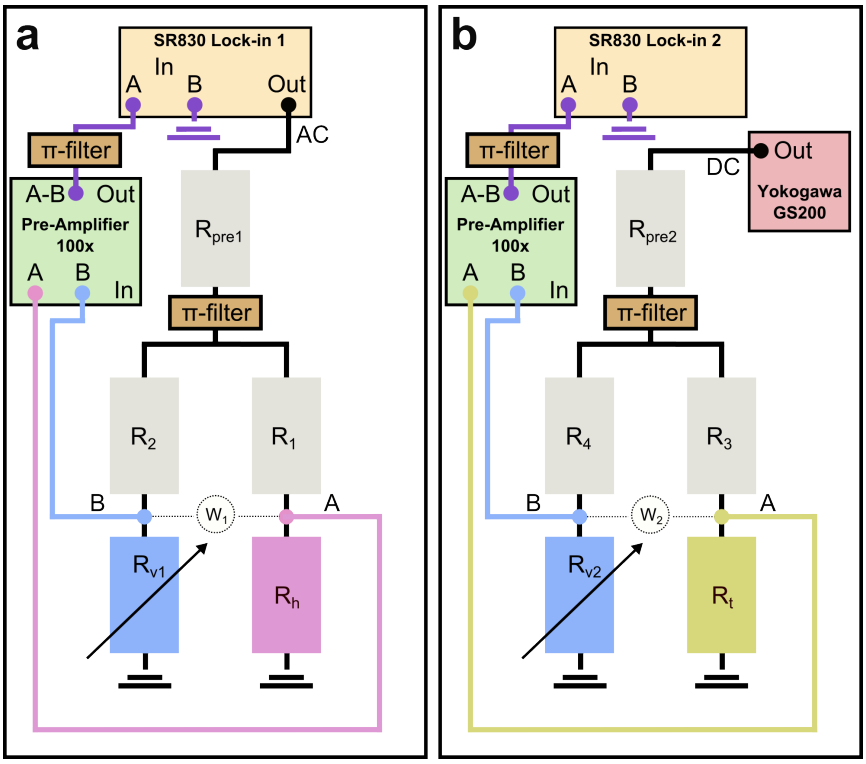


FIGURE 4.11: (a) Schematic view of the Wheatstone bridge used to measure the heater ($R_h$). An AC source voltage is applied by a Lock-in. The current goes through a pre-resistor $R_{pre1}$ (10 kΩ), a π-filter, then enters the Wheatstone bridge. $R_1$ and $R_2$ are both 330 Ω. The lock-in measures the pre-amplified (100x) Wheatstone voltage ($W_1$, indicated with dashed lines) between points A and B. (b) Same setup for the thermometer. $R_3$ and $R_2$ are both 330 Ω, pre-resistor $R_{pre2}$ is 100 kΩ. Instead of a lock-in a Yokogawa is now used as a DC-source for the bridge.

#### 4.5.2.5 Frequency and power sweep setup

To acquire the thermal conductivity $\lambda_{hBN}$ we need to both make sure we are in the linear regime and measure the temperature drop between the heater and the thermometer $\Delta T_{h-t}$. The first is needed to assure that Equation 4.34 is valid and is done by measuring $\Delta T_{h-t}$ as function of the applied power $P$ (power sweeps). The second is needed to calculate the thermal conductivity using Equation 4.34 and is done by measuring $\Delta T_{h-t}$ as function of the frequency $f$ (frequency sweeps). In both cases we acquire $\Delta T_{h-t}$ by measuring $V_{3\omega}$ (see Equations 4.21 and 4.33).

To acquire the thermal diffusivity $D_{hBN}$ we need to measure the phase shift $\Delta\phi$ between the heater and the thermometer as function of frequency (frequency sweeps).

We perform frequency sweeps of both heater and thermometer simultaneously using the Wheatstone bridges described in Section 4.5.2.3. The lock-ins are locked together, measuring at the same frequency. The sweep goes from 1 Hz to 100 kHz. The central heater is being heated, which creates a $3\omega$ signal on voltage $W_1$ of the heater bridge. The reference thermometer picks up the heat flux from the central heater. Since the source current of the thermometer is DC, we can therefore pick up a $2\omega$ signal at the voltage $W_2$ of the thermometer bridge (see Section 4.4.1). Both signals allow us later to extract the $\Delta T$ at both heater and thermometer. We measure

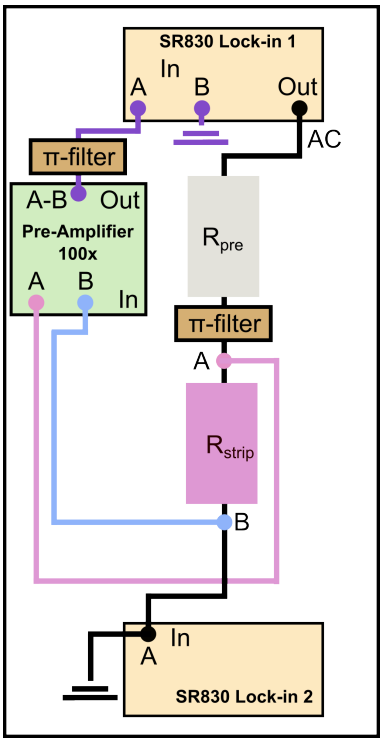


FIGURE 4.12: Schematic of the measurement setup for a heater/thermometer calibration. The first lock-in serves as a voltage source: the AC current goes through the pre-resistor $R_{pre}$ (100 kΩ), through the metal strip ($R_{strip}$, could be either the heater or the thermometer), through the second lock-in that measures the current and then to ground. The first lock-in measured the amplified (100x) voltage drop over $R_{strip}$ (A to B).

both the amplitude and the phase of the voltages $W_1$ and $W_2$. The amplitude will later be needed to determine the thermal conductivity and the phase to determine the thermal diffusivity of our h-BN flakes.

We perform two types of frequency sweeps. The fast sweeps (50 frequency points), using logarithmic scale, for the amplitude measurements, and slow detailed sweeps (519 frequency points), using linear scale, for the phase measurements. Although each measurement captures both the phase and the amplitude, as we found out, it is impossible to fit the phase accurately when measured on a logarithmic scale. Detailed linear sweeps allowed to average the phase and to better analyse the result. Yet, detailed linear sweeps take about 9 hours for one bath temperature, while the logarithmic measurements take up only 1.5 hour and have a way lower helium consumption as a result. Since for the amplitude measurements we do not need so many points, we therefore performed many short logarithmic measurements and only several long linear measurements for each sample.

With the same setup as the frequency sweeps we also perform the power sweeps. In this case, instead of varying the frequency, we vary the source voltage of the heater, keeping the frequency (5 Hz) and the bath temperature constant and measuring the voltages $W_1$ and $W_2$. We sweep the power from 0.01 µW up to the maximum used power for the sample.

### 4.5.3 Sample characterization

We have characterized four different devices, each with its own geometry. In Figure 4.13 one can see optical images of all four samples. Sample 1 (Figure 4.13a1) has an elongated slit of 2 by 20 µm, Sample 2 (Figure 4.13b1) has a square slit of 5 by 5 µm, Sample 3 (Figure 4.13c1) has a square slit of 7 by 7 µm and Sample 4 (Figure 4.13d1) has a square slit of 10 by 10 µm. All of them have a h-BN flake on top of the slit. As one can see by the color contrast, all four samples have a h-BN flake about 2-3 times bigger than the slit surface, covering most of the region between the heater contacts. This forms a certain overlap region between the suspended h-BN and SiN membrane.

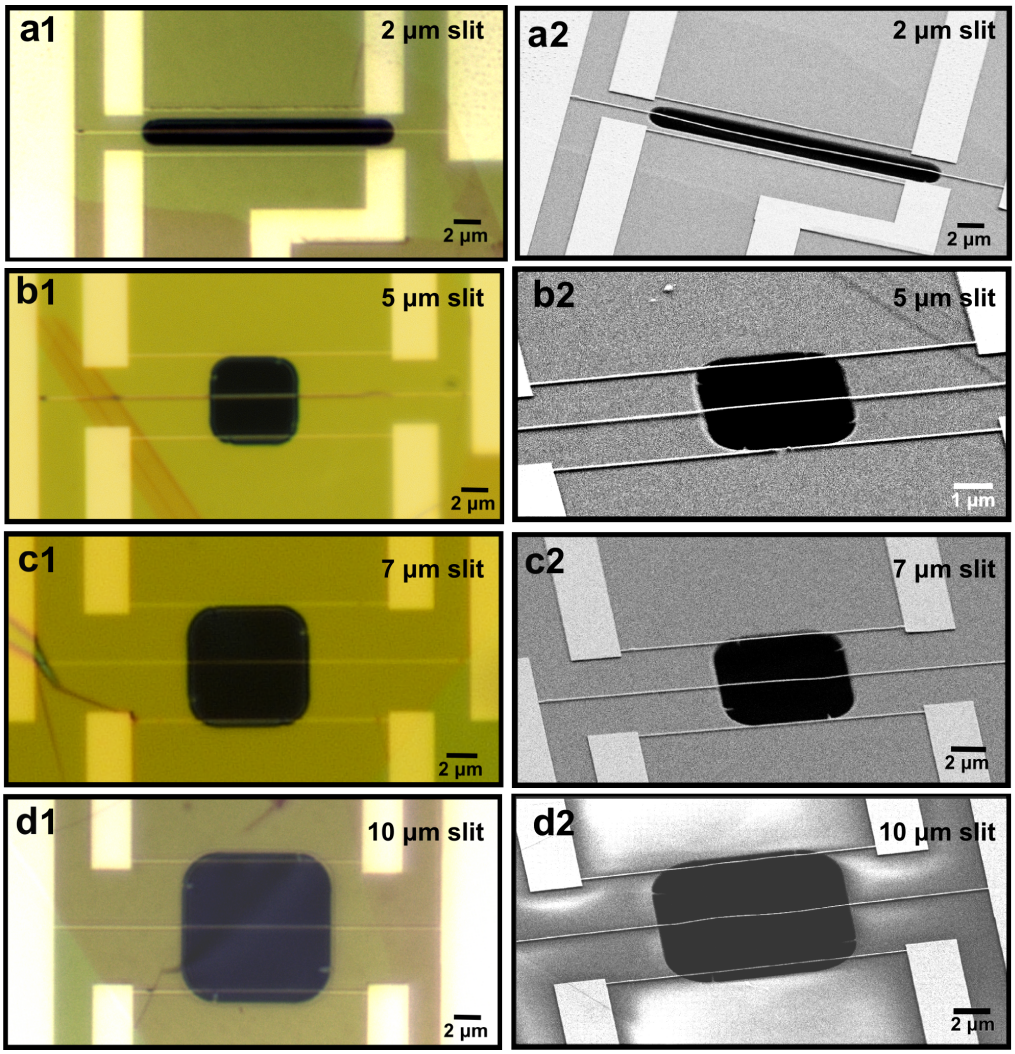


FIGURE 4.13: Optical (left) and SEM (right) images of the four samples. The optical images are taken with a 100x magnification. SEM images are taken with a 45 degree tilted holder. The tilt is perpendicular to the heater. The SEM images are all taken at 2 kV. (a) The 2 µm slit sample. (b) The 5 µm slit sample. (c) The 7 µm slit sample. (d) The 10 µm slit sample.

In Figures 4.13a2, 4.13b2, 4.13c2 and 4.13d2 one can see the SEM images of all four devices. Closer to the contacts the heater tends to bend. In Figure 4.14 one can see a zoom-in of the SEM images from Figure 4.13. It shows the bending of the heater in close-up. The bends in the heater are caused by the kink in the flake at the edge

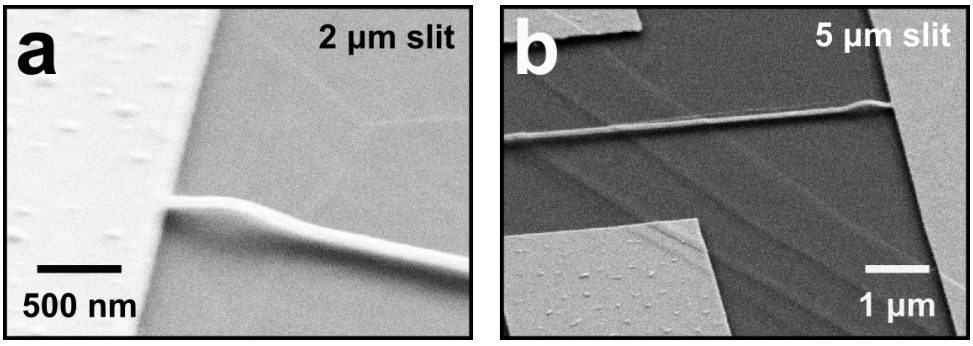


FIGURE 4.14: SEM zoom-in images showing the bending of the heater close to the contacts. (a) Zoom-in of the 2 µm slit. (b) Zoom-in of the 5 µm slit.

of the slit. The border of the etched SiN membrane pulls the flake by van der Waals forces, causing this kink and creating tension in the heater and the flake. Between the edges of the slit the flakes and heaters are straight and defect-free.

In Figure 4.15 one can see optical images of all four samples, taken at 5x magnification. Here one can see the contact structure, from the slit to the bonding pads. The green area is the SiN membrane on top of the Si frame, the orange square indicated the suspended SiN membrane. The slit is positioned in the middle of the membrane and the contact structure. Contacts on top of the membrane are relatively narrow (9 µm), but become wider (80 µm) towards the supported SiN region. This is done to minimize the weight on top of the SiN membrane to avoid its collapse.

In Figure 4.16 one can see the AFM images of all the four devices. Each image shows a part of the h-BN flake and SiN substrate. The white line shows where the height profile was taken and next to each panel a height profile taken at that line is shown. The following heights were measured: 8.5 nm ($\approx$ 25 layers) for the 2 µm slit sample, 6.5 nm ($\approx$ 20 layers) for the 5 µm slit sample, 11.5 nm ($\approx$ 35 layers) for the 7 µm slit sample and 11 nm ($\approx$ 33 layers) for the 10 µm slit sample.

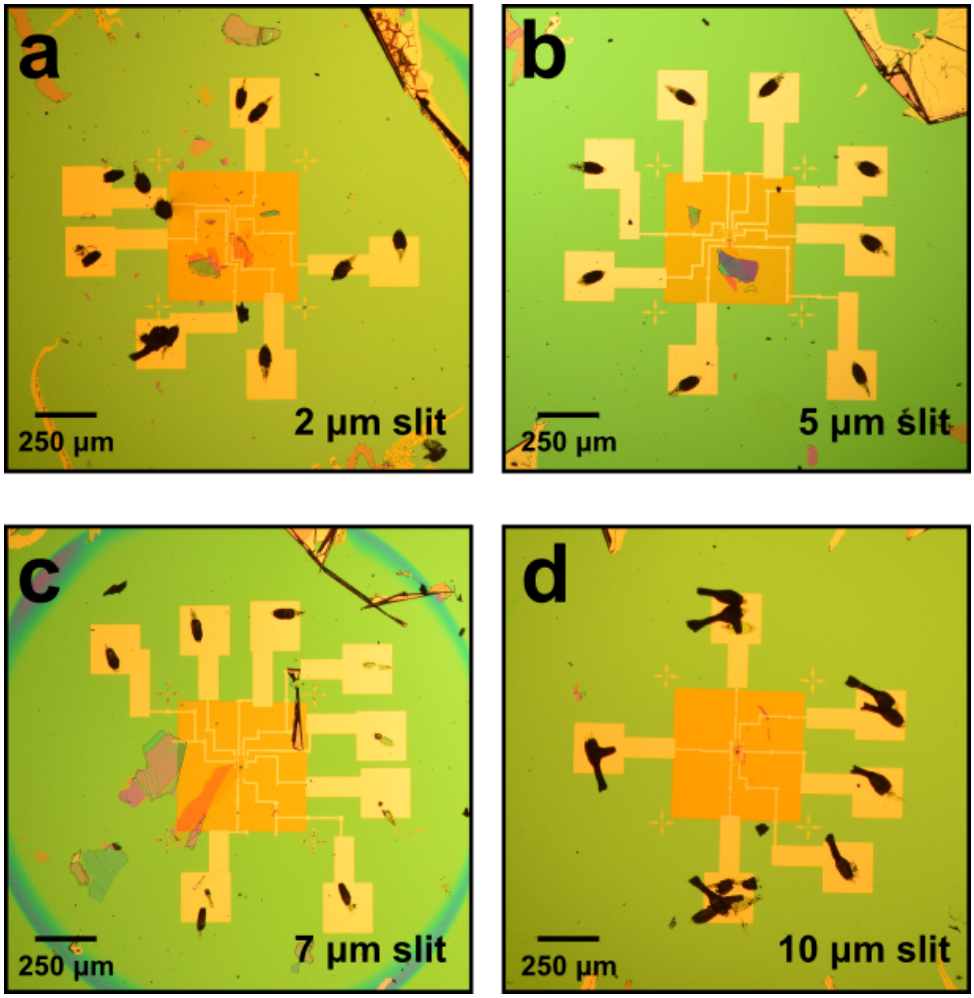


FIGURE 4.15: Optical images of all four samples with a 5x magnification. The green area is the SiN on Si frame, the orange area is the suspended SiN membrane, the yellow area's are the golden contacts. The flake and the slit are at the center of the SiN membrane. (a) The 2 µm slit sample. (b) The 5 µm slit sample. (c) The 7 µm slit sample. (d) The 10 µm slit sample.

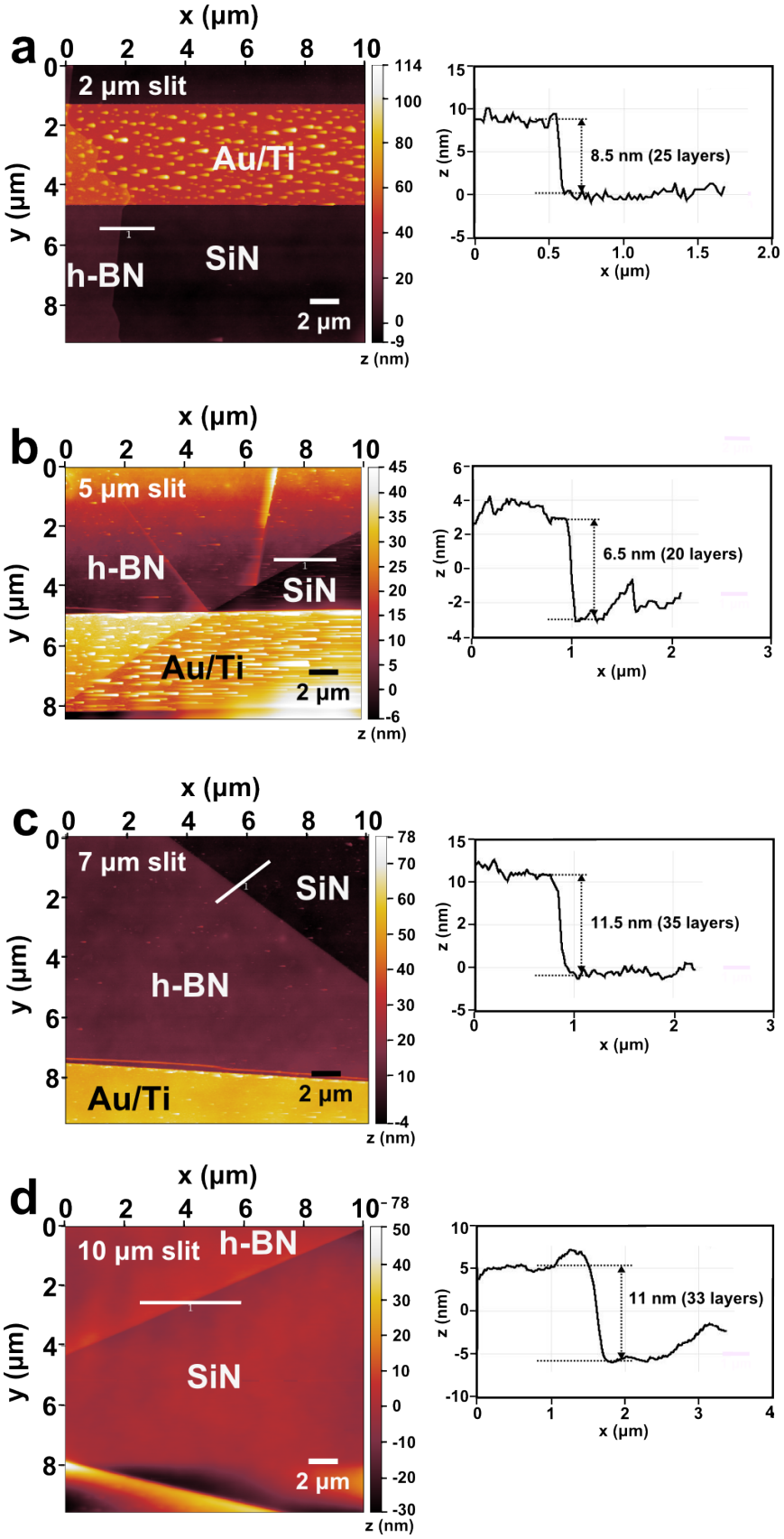


FIGURE 4.16: AFM images of all four samples. Each panel shows a part of the h-BN flake and the SiN substrate. The white line indicates the place where the height profile is taken. Next to the AFM image the height profile is shown. (a) The 2 μm slit sample. (b) The 5 μm slit sample. (c) The 7 μm slit sample. (d) The 10 μm slit sample.

## 4.6 2D COMSOL simulation

In addition to our 1D theoretical model (see Section 4.2.3), we also have made a COMSOL 2D simulation of a zero frequency heating profile in our samples. In contrast to the simpler 1D model, which only considers two materials and 1D heat transport, in the simulation we have implemented all possible elements present on the sample and have used a 2D approach to the transport, allowing the heat flow to spread both parallel and orthogonal to the heater, rather than only orthogonally. But we only took into account the heating profile at zero frequency, therefore not calculating any phase shifts.

In the simulation we have put five different regions: suspended h-BN, supported h-BN on top of $Si_3N_4$, $Si_3N_4$ and gold contacts, either on top of $Si_3N_4$ or on top of a bilayer of h-BN and $Si_3N_4$. The gold contacts are shaped as similar as possible to the sample configuration: we start with the narrow part (4 µm wide), that then broadens out (9 µm wide) and reaches to the border of the $Si_3N_4$ membrane. We have one heater and two thermometers in the simulation. One thermometer at the edge of the slit and the second one 40 µm away from the heater, as present in the 5 µm slit sample. We take the slit to be 10 by 10 µm, the h-BN flake being 30 by 30 µm and the $Si_3N_4$ being 500 by 500 µm. We simulate at the bath temperature of 200 K.

The 2D simulation does not take into account the thickness ratio of the different regions. It presumes all of the regions have an infinite thickness, which is not the case for our samples. Therefore we introduce an effective thermal conductivity for each of the materials, that takes the layer thickness into account:

$$\lambda_{eff} = \lambda_{mat} \cdot \frac{t_{mat}}{t_{SiN}}, \tag{4.42}$$

with $\lambda_{eff}$ the effective thermal conductivity of the material, $\lambda_{mat}$ the thermal conductivity of the material, $t_{mat}$ the thickness of the material and $t_{SiN}$ the thickness of the $Si_3N_4$ membrane.

The model requires for each material an input of the effective thermal conductivity $\lambda_{eff}$, heat capacity and mass density. For gold we take those from literature [116]. The thermal conductivities of h-BN and $Si_3N_4$ are estimated from literature [32, 112] and taken as 100 (effective conductivity of 5.5 W $m^{-1}$ $K^{-1}$) and 5 (effective conductivity of 5 W $m^{-1}$ $K^{-1}$) respectively. The heat capacity of h-BN is taken from the measured literature values for bulk h-BN [117]. The heat capacity of $Si_3N_4$ is taken from [118], measured for 100 nm thick $Si_3N_4$ membranes.

For regions where two materials were present, like the overlap between the h-BN flake and the $Si_3N_4$ or the overlap of the gold contacts and the $Si_3N_4$, we calculated the thermal conductivity in the following way:

$$\lambda_{bilayer} = \frac{\lambda_1 \cdot t_1 + \lambda_2 \cdot t_2}{t_1 + t_2}, \tag{4.43}$$

with $\lambda_{bilayer}$ the thermal conductivity of the overlap region, $\lambda_1$ and $\lambda_2$ the thermal conductivities of the first and second materials in the overlap region respectively and $t_1$ and $t_2$ the thicknesses of the first and second materials, respectively.

In Figure 4.17 one can see the simulated 2D heating profile. In the middle there is the suspended part of the h-BN flake, shown as the small square. Around it is the supported h-BN region, shown as a bigger square. The vertical short green lines crossing the suspended part are the heater and the first thermometer. The vertical short line 40 µm away from the center is the second thermometer. Those are the lines at which we take the temperature profiles, they are not defined in the simulation as

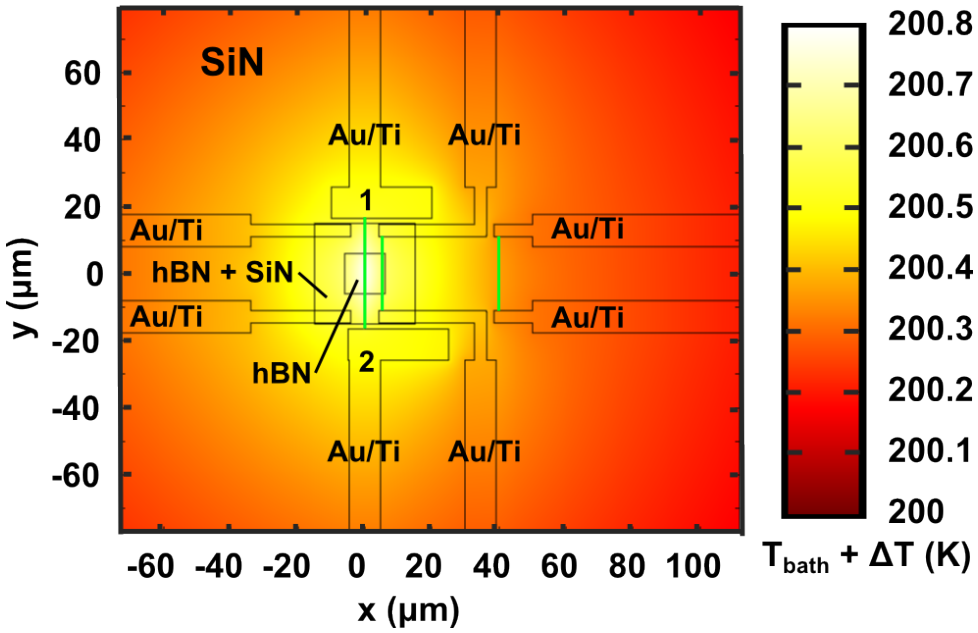


FIGURE 4.17: Simulation with COMSOL of a 2D zero frequency heating profile. The lines indicate the borders of different regions: the suspended h-BN flake in the middle (small square), the supported h-BN flake around it (bigger square), the heater and the two thermometers (three green vertical lines, one in the center, one at the edge of the slit and one further away) and the gold contacts that contact the heater and the thermometers. The simulation is run with the following parameters: $T_{bath}$ = 200 K, $\lambda_{SiN}$ = 5 W m$^{-1}$ K$^{-1}$, $\lambda_{hBN}$ = 100 W m$^{-1}$ K$^{-1}$. Suspended part of the h-BN flake is 10 by 10 µm, the total size of the h-BN flake is 30 by 30 µm.

part of the gold geometry, since they are too narrow to change the heating profile significantly. The geometrical shapes in contact with the heater and the thermometer are the gold contacts. As one can see the heat spreads radially from the heater, forming an ellipse-like shape, that is slightly asymmetric. This asymmetry is due to the asymmetry of the gold contacts contacting the heater (labeled by 1 and 2). The temperature increase ranges from 0 to 0.8 K.

In Figure 4.18 one can see the temperature profile simulated along a 100 µm long line orthogonal to the heater, from the center of the heater. Figure 4.18a shows the full profile, and Figure 4.18b a zoom-in of the profile. Both panels are color-coded. In Figure 4.18c shows a schematic side view of the sample, explaining the colored regions. The blue part indicates the suspended h-BN part, the rosa part indicates the overlap region of the flake and membrane and the light purple part indicates the $Si_3N_4$ membrane. As one can see, the profile of suspended h-BN is the steepest, while the mixed region has the smallest temperature drop. This is expected, since the mixed region has the highest thermal conductance of the three regions.

In Figure 4.19 one can see the simulated temperature profiles along the heater and the two thermometers. In Figures 4.19a-c the individual profiles are shown, and in Figure 4.19d one can see the comparison of the variation of such profiles. There we subtracted the minimum value of the temperature increase, so that one can compare how much the $\Delta T$ varies between the outer ends of the heater/thermometer and its center. As one can see, the profile smoothes out the further the thermometer is from the heater and the absolute variation decreases. So does the procentual

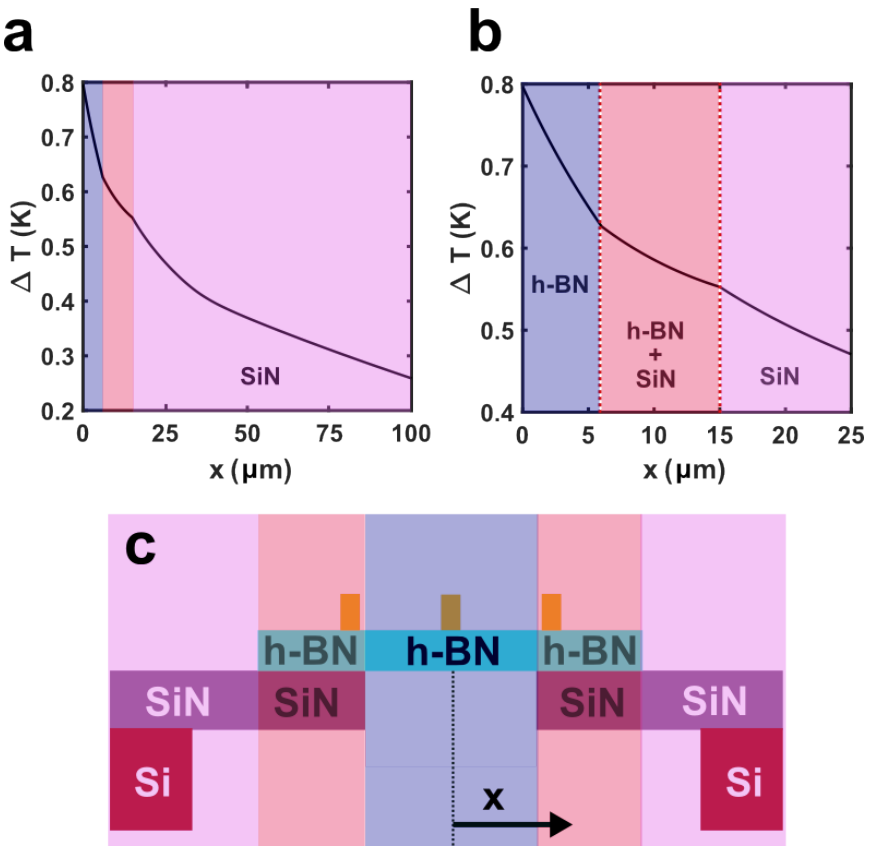


FIGURE 4.18: (a) Temperature increase $\Delta T$ as function of distance $x$ from the heater. The colors indicate different regions, from left to right: h-BN (blue), h-BN on top of $Si_3N_4$ membrane (rosa) and $Si_3N_4$ (light purple)). The profile is sumulated by the COMSOL and extracted from Figure 4.17 (b) Zoom-in of (a), showing the temperature profile more clearly. (c) A schematic depiction of the simulated geometry, side view. The material regions are color-coded the same way as in (a) and (b).

variation: while the heater shows 30% variation, the first and second thermometers show only a variation of 7.9% and 4.1% respectively. Over-all, the maximum variation observed is only $\pm$125 mK from the average heater temperature and even lower for the thermometers.

## 4.7 Results

### 4.7.1 Heater and thermometer calibration

As described in section 4.5.2.3, we start by characterizing our heater and thermometer. To be able to later extract the thermal conductivity and thermal diffusivity from our frequency sweeps, we need to calibrate both our heater and thermometer by measuring their electrical four-contact resistance ($R_h$ and $R_t$) as function of the bath temperature $T_{bath}$. In figure 4.20a one can see the heater resistance $R_h$ of all four samples plotted versus the bath temperature $T_{bath}$ as open circles. The behavior is almost perfectly linear. In Figure 4.20b one can see the same curves ($R_t$ as function of $T_{bath}$) for the thermometers of all the four samples.

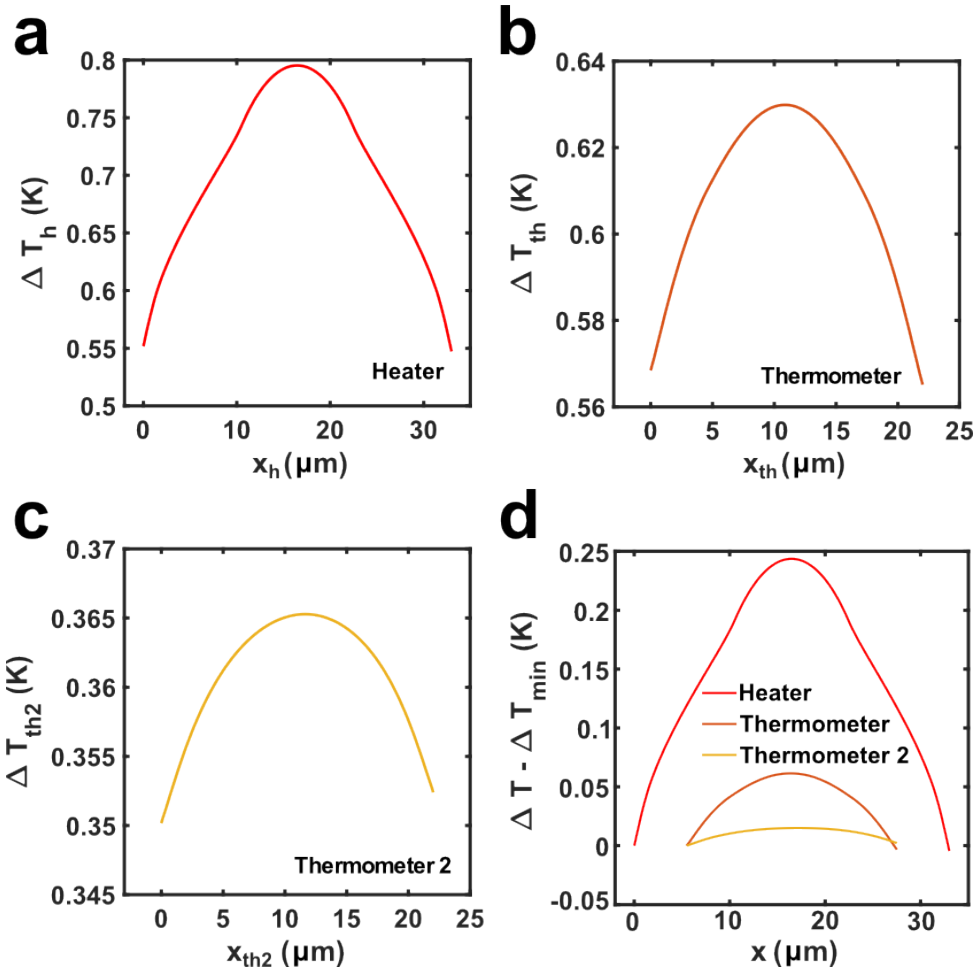


FIGURE 4.19: (a) The temperature increase $\Delta T_h$ at the heater as function of the spacial dimension along the heater $x_h$. (b) The temperature increase $\Delta T_{th}$ at the first thermometer as function of the spacial dimension along the first thermometer $x_{th}$. (c) The temperature increase $\Delta T_{th2}$ at the second thermometer as function of the spacial dimension along the second thermometer $x_{th2}$. (d) The temperature increase variation $\Delta T - \Delta T_{min}$ as function of spacial dimension for the heater and the two thermometers.

One can see that the electrical resistances of the heaters are always higher than the corresponding thermometer resistances. This is due to the fact, that the thermometer is only 22 µm long, while the heater is 33 µm long. We kept the geometry of the golden contacts, heater and thermometer the same from sample to sample. The thermometer is as long as our longest slit (20 µm) plus 2 µm of alignment margin. The heater is 11 µm longer, to leave enough space for the thermometer contacts.

From the values in Figures 4.20a and 4.20b and we can calculate the sheet resistance of the heaters and thermometers, using the following formula:

$$R_{sheet} = R_{strip} \cdot \frac{b_h}{l_h}, \tag{4.44}$$

with $R_{sheet}$ the electrical sheet resistance of the heater/thermometer, $R_{strip}$ the electrical resistance of the metal strip (heater/thermometer), $b_h$ the width and $l_h$ the length of the heater/thermometer. With a width of 100 nm and length of 33 µm for the heater and 22 µm for the thermometer we measure sheet resistances of 1.5-2 Ω

for 30K and of 2.1-3.8 Ω for 300 K. This seems pretty close to the reported values from literature of 0.5-1 Ω [119] for gold films of 25.4 and 46 nm, which is similar to our heater thickness of 40 nm. Since our heater is not just gold, but 30 nm of gold and 10 nm of titanium, a small discrepancy with literature is expected.

We fit all eight curves with a fifth degree polynomial (solid black line) and take the derivative of the polynomial as $\frac{dR}{dT}$. The values of $\frac{dR}{dT}$ vary between 0.86 and 1.32 Ω/K. In Figures 4.20c and 4.20d one can see the difference between the data and the polynomial fit. The observed oscillations are probably due to the measurement uncertainty of the cryostat thermometer, since they are the same for all samples and therefore are sample independent. As one can see, we have a precision of about 0.5 Ω for the heater, which, with our values of $\frac{dR}{dT}$ would mean an absolute precision of about 0.5 K for the bath temperature $T_{bath}$, corresponding to a relative $T_{bath}$ uncertainty of 1% for 50 K and 0.19% for 270 K. For the thermometer it is 0.25 K, with relative error of 0.5% for 50 K and 0.095% for 270 K.

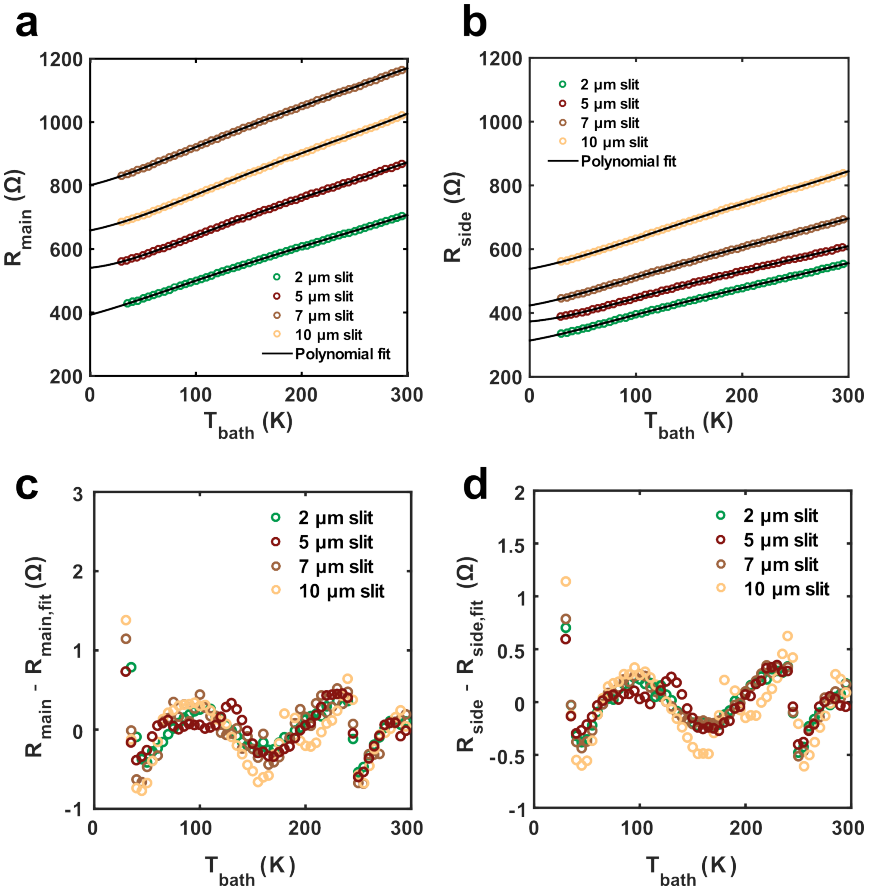


FIGURE 4.20: (a) Resistances of the four sample heaters $R_h$ (open circles) and corresponding polynomial fits (solid lines) as function of bath temperature $T_{bath}$. (b) Resistances of the four sample thermometers $R_t$ (open circles) and corresponding polynomial fits (solid lines) as function of bath temperature $T_{bath}$. (c) The difference between the data in and the polynomial fits in (a). (d) The difference between the data in and the polynomial fits in (b).

### 4.7.2 Linearity of the thermal transport

We did several power sweeps, keeping the frequency constant and varying the source voltage applied to the heater Wheatstone bridge. According to the Fourier's law [96], the $\Delta T_h$ should be linearly proportional to the applied power $P$, if the thermal gradient is low enough. Those sweeps were performed to check if we are really in that linear regime.

In Figure 4.21 one can see the difference between $\Delta T_h$ and $\Delta T_{th}$ for three samples (2, 5 and 10 µm slit samples) as function of applied electrical power $P$. The sweeps are all taken at 5 Hz, since, as we will see in Figure 4.22, this frequency falls in the constant low-frequency regime at all bath temperatures for all the samples.

Unfortunately, the 5 µm slit sample broke during the measurements, and there we were not able to measure the power sweeps. Therefore only three out of four samples are shown in Figure 4.21. Yet, we are confident that this sample would show the same type of characteristics, since the temperature differences in Figure 4.22 and the applied power were similar to other samples.

In all three panels of Figure 4.21 (corresponding to 2 µm slit, 7 µm slit and 10 µm slit) we see a clear linear behavior. This confirms that we are in the linear regime and that we can use Equation 4.34 to calculate the thermal conductivity.

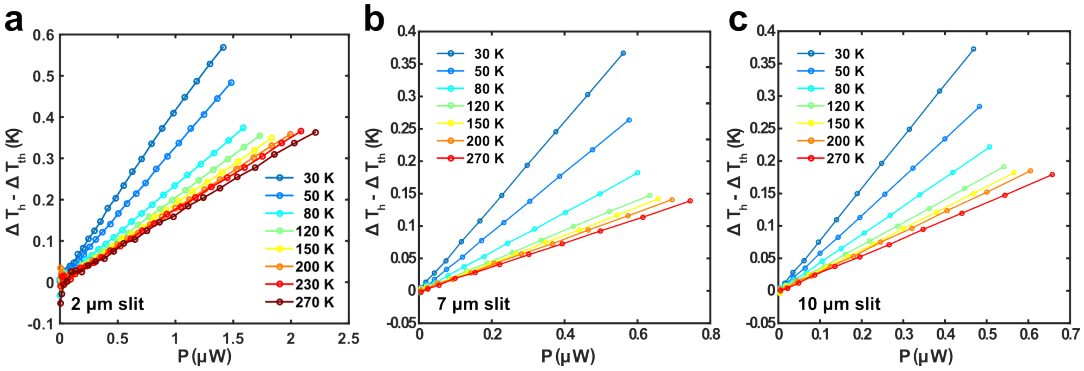


FIGURE 4.21: (a-c) The difference between temperature difference at the heater $\Delta T_h$ and temperature difference at the thermometer $\Delta T_{th}$ for the 2, 5 and 10 µm slit samples correspondingly as function of applied electrical power $P$ at the heater.

### 4.7.3 ΔT measurements

After characterizing the heater and the thermometers and confirming through the power sweeps that we are still in the linear regime, we measure $\Delta T_h$ and $\Delta T_{th}$ as function of frequency. As mentioned in Section 4.5.2.5, for the thermal conductivity we only need short measurements, taking the frequency points on a logarithmic scale. We measure the 3rd harmonic of the heater Wheatstone voltage $W_1$ and the 2nd harmonic of the thermometer Wheatstone voltage $W_2$ (see Figure 4.11 for the measurement setup details). We apply a source voltage $V_s$ of 550 mV (RMS) at the heater bridge ($P$ of $\approx$ 450 nW for 30 K and 600 nW for 270 K) and probe the thermometer using 1V DC voltage. This corresponds to a current of about 25 µA and 5 µA respectively.

In Figure 4.22 one can see the temperature differences measured for the heater ($\Delta T_h$) and at the thermometer ($\Delta T_{th}$) for all four samples for different bath temperatures. The temperature differences are in the order of 100 mK for the heater and

about 10 mK for the thermometer. As one can see about 70% of the temperature drop happens between the heater and the thermometer.

The curves all have a constant region in the low frequency regime and a fast decay in the high frequency regime. This behavior is expected (see Section 4.3.2). In the constant region before the thermal cut-off, the heat current in the sample can keep up with the frequency (thermal penetration depth $L_{th}$ is bigger than the sample size), after the cut-off happens, the temperature difference start to go to zero. The thermal cut-off frequency is around 3-100 Hz for all the curves.

Additionally we had a yet another thermometer for the 5 µm slit sample. This thermometer is 40 µm away from the heater.

In Figure 4.23 one can see the comparison of the temperature difference $\Delta T_h$ at the heater and the temperature difference $\Delta T_{th2}$ at the second thermometer for the 5 µm sample. As one can see, the temperature drop from the first to second thermometer is about 30 mK, which is only 38% of the temperature difference at the first thermometer. For comparison, the drop between the heater and the first thermometer is 73% of the temperature difference at the heater. This shows that there is a long tail after the initial drop between the heater and the first thermometer, with a slow decay of the temperature difference with the distance. It is also in agreement with our 2D COMSOL simulation (see Figure 4.18), where we saw that the at a distance of 100 µm from the heater still about 25% of the initial temperature difference $\Delta T_h$ was present.

This long tail explains the low thermal cut-off frequency in Figure 4.22. The $Si_3N_4$ membrane dominates the time response of the sample, since the suspended h-BN region is much shorter than the $Si_3N_4$ region that comes after the first thermometer. The fact that we can not separate the time response of the h-BN flake and the time response of the $Si_3N_4$ is one of the main reasons why we introduced the thermometers in our samples.

### 4.7.4 Phase shifts

After performing the logarithmic frequency sweeps, we performed several detailed sweeps, this time taking frequency points on a linear scale. Those measurements are performed to accurately measure the phase of the signal to later obtain the thermal diffusivity $D_{hBN}$ (see Section 4.4.3 and Equation 4.39). The detailed sweeps allow for proper averaging of the data and improving the signal-to-noise ratio, which in turn will help to analyze the data more accurately.

We again apply a source voltage $V_s$ of 550 mV (RMS) at the heater bridge ($P$ of $\approx$ 450 nW for 30 K and 600 nW for 270 K) and probe the thermometer using 1V DC voltage. In Figure 4.24 one can see the phase difference between the heater and the thermometer $\Delta\phi$ for all four samples, for different bath temperatures. On the left (Figures 4.24a,4.24c, 4.24e and 4.24g) one can see the data as function of $\sqrt{f}$, for the range up to 10 $Hz^{1/2}$ (100 Hz). On the right (Figures 4.24b,4.24d, 4.24f and 4.24h) the phase difference is plotted as function of frequency up to 1000 Hz.

Figure 4.24b and 4.24d show the data of the 2 µm slit and the 5 µm slit respectively as function of frequency. One can see a small linear increase (up to 5 degrees at 1000 Hz) and almost no distinct bath temperature dependence. This is in strong contrast with Figure 4.24f and 4.24g, that show the data from longer flakes, the 7 µm slit and the 10 µm slit. The longer flakes show a much bigger phase shift and a clear bath temperature dependence. Also, for those two longer samples we can distinguish two regimes: the low frequency regime (up to $\approx$ 200 Hz) with square

root dependence on the frequency ($\Delta\phi \propto \sqrt{f}$)) and the high frequency regime (from $\approx$ 200 Hz on) showing linear behavior ($\Delta\phi \propto f$).

To further show that indeed the low-frequency regime of $\Delta\phi$ is proportional to $\sqrt{f}$, we plot the region up to 100 Hz (10 $\text{Hz}^{1/2}$) as function of $\sqrt{f}$. Since this region does not contain as many points as the full region, we can not average it as well as the full $\Delta\phi$ curve. Therefore we plot the raw data. For the short samples, 2 µm slit and 5 µm slit (Figures 4.24a and 4.24c), the data is too noisy to make a clear statement about the proportionality to $\sqrt{f}$, but for the longer samples, the 7 µm slit and the 10 µm slit (Figures 4.24e and 4.24g), one can clearly note a linear dependence. One can also see that for those two samples the linear coefficient between $\Delta\phi$ and $\sqrt{f}$ decreases with increasing bath temperature. The slopes become less steep.

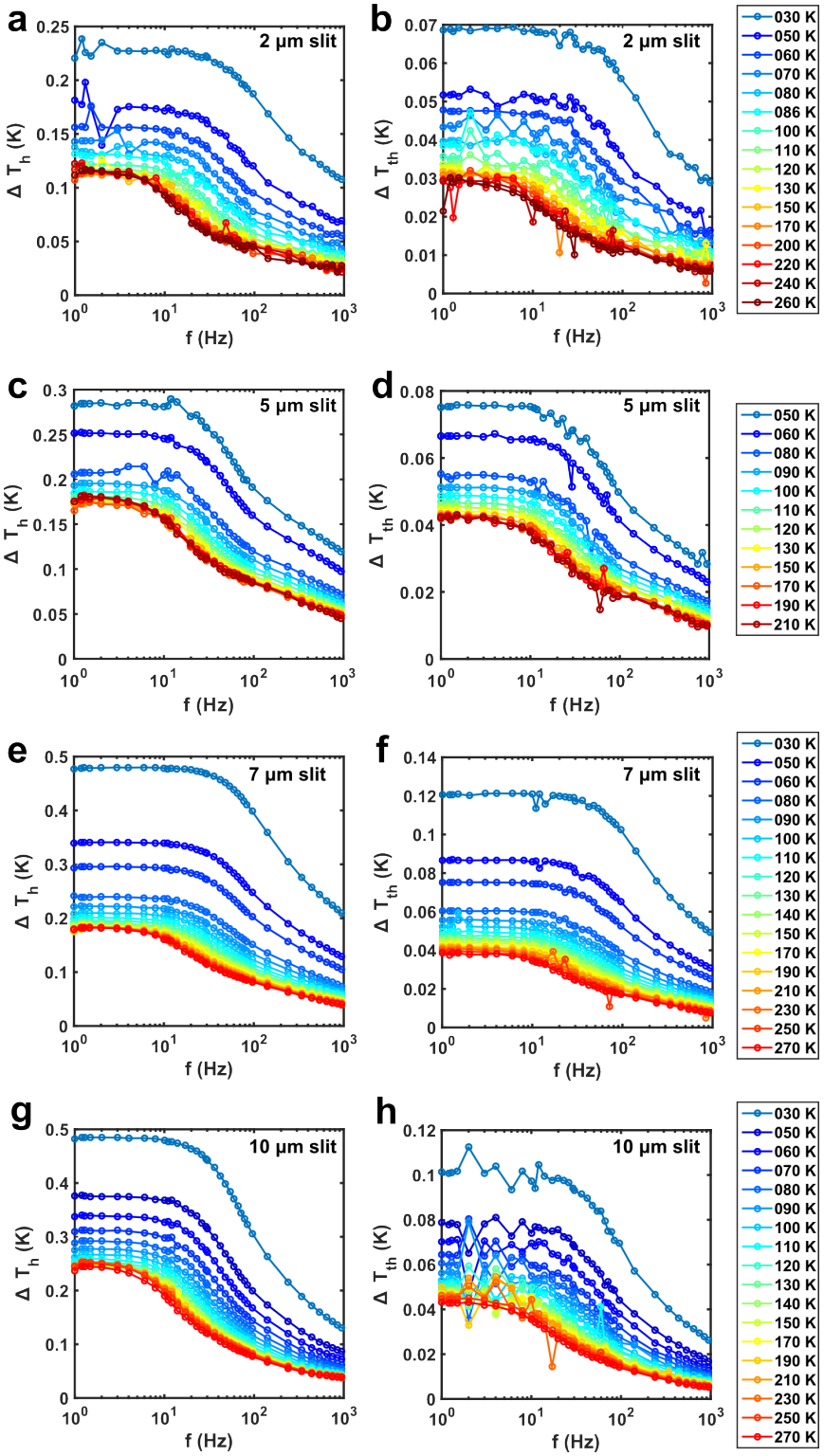


FIGURE 4.22: (a, c, e) Temperature difference $\Delta T_h$ at the heater of Sample 1-3 as function of frequency for different bath temperatures. (b, d, f) Temperature difference $\Delta T_{th}$ at the thermometer of Sample 1-3 as function of frequency for different bath temperatures. $V_{source}$ for the heater is 550 mV (AC), $V_{source}$ for the thermometer is 1V (DC).

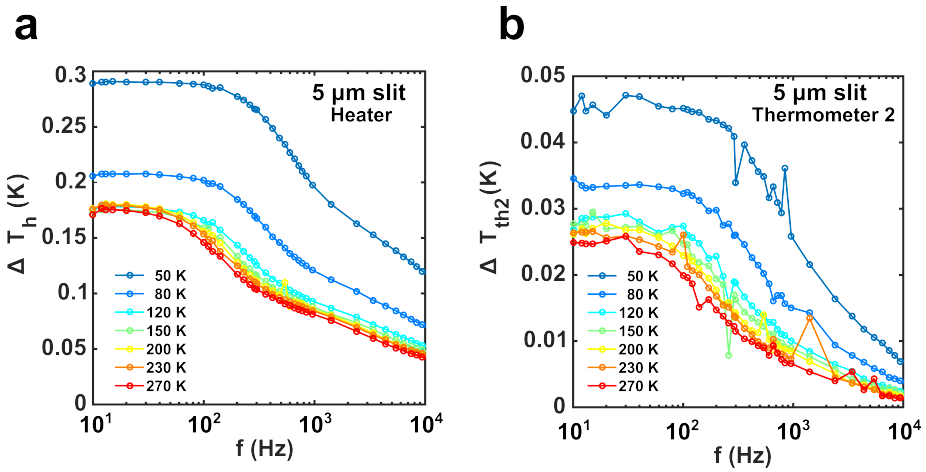


FIGURE 4.23: (a) Temperature difference at the heater $\Delta T_h$ as function of frequency for the 5 µm sample for different bath temperatures. (b) Temperature difference $\Delta T_{th2}$ at the faraway thermometer of the 5 µm sample (40 µm away from the heater) as function of frequency for different bath temperatures.

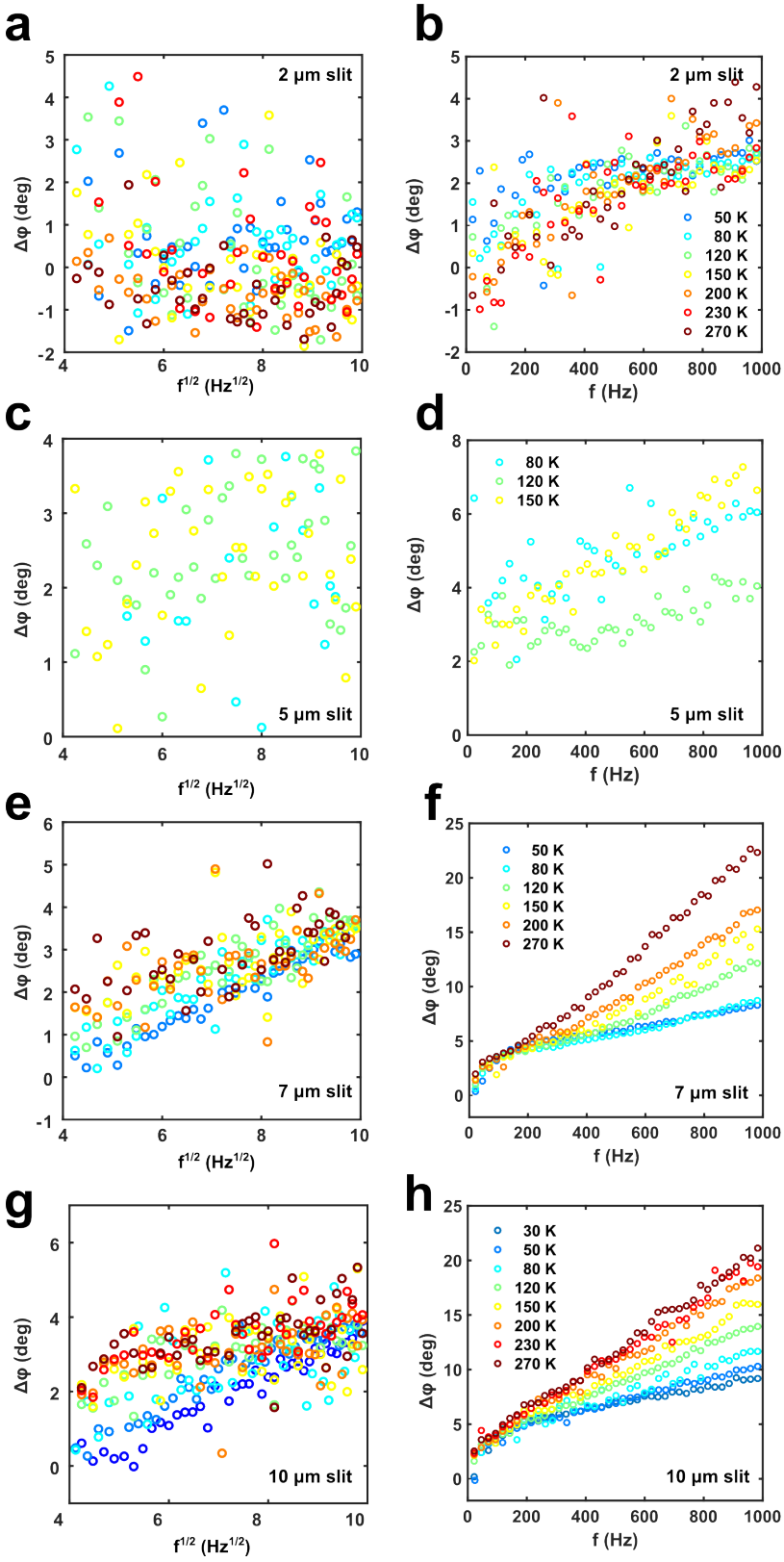


FIGURE 4.24: (a,c,e,g) Raw data of the phase difference between the heater and thermometer $\Delta\phi$ in degrees as function of square root of frequency, for different bath temperatures for the 2 μm slit, 5 μm slit, 7 μm slit and 10 μm slit correspondingly. The range of frequency goes only up to 10 $Hz^{1/2}$ (100 Hz). (b,d,f,h) Averaged data (averaging over sets of 12 points) of the phase difference between the heater and thermometer $\Delta\phi$ in degrees as function of frequency, for different bath temperatures for the 2 μm slit, 5 μm slit, 7 μm slit and 10 μm slit correspondingly. Full frequency range (up to 1000 Hz) is shown.

## 4.8 Analysis of the results

### 4.8.1 Contact resistance

Figure 4.21 shows that we are clearly in a linear transport regime, where $\Delta T_{h-t} = P \cdot R_{th}$, with $R_{th}$ the total thermal resistance of the h-BN flake, heater and possible interface resistances.

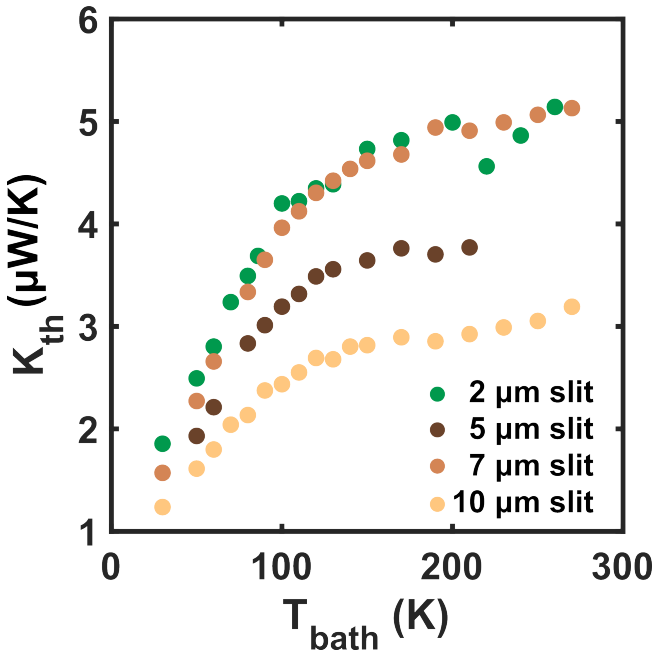


FIGURE 4.25: The total thermal conductance of the sample $K_{th}$ for all four samples as function of the bath temperature $T_{bath}$.

In Figure 4.25 one can see the total thermal conductance $K_{th}$ of the sample, the inverse of the thermal resistance $R_{th}$. There seems to be no clear thickness or half-width dependence.

But if we plot the thermal resistance as function of flake half-width $b_{hBN}/2$, the dimension along the heat flow, we can expect the thermal resistance of the h-BN flake $R_{th,hBN}$ to be the only part to depend on the distance between the heater and thermometer ($b_{hBN}/2$). If any additional resistance is present, like the thermal resistance of the heater or of any interface between heater and the flake, it would cause an offset in the $R_{th}$, shifting it up along the y-axis. It might also hide a thickness or half-width dependence in Figure 4.25, because those resistances would not depend on either of those parameters.

In Figure 4.26a one can see $R_{th}$ plotted as function of the distance between the heater and thermometer for different bath temperatures. The data of the 2, 5 and 10 μm slits show linear behavior with the distance, while the 7 μm slit sample shows a systematically lower thermal resistance than the other three samples. The data do not extrapolate to zero, which indicates the presence of a thermal contact resistance $R_c$.

In Figure 4.26b one can see this thermal contact resistance $R_c$ plotted as function of bath temperature. The decay is in agreement with the fact that thermal conductance increases with the bath temperature for solids. The observed contact resistance $R_c$ contributes at least 50% of the full thermal resistance for the 10 μm sample, and

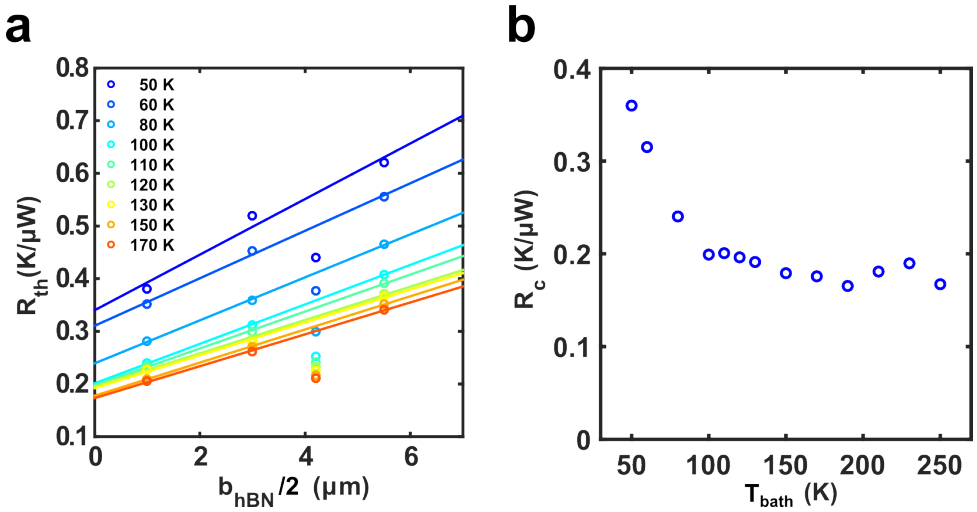


FIGURE 4.26: (a) The thermal resistance $R_{th}$ of the h-BN flake, contacts, heater and thermometer as function of the half-width of the h-BN flake $b_{hBN}/2$ for different bath temperatures. (b) The thermal contact resistance $R_c$ as function of bath temperature $T_{bath}$.

even more for the smaller samples at 50 K, decreasing to 30% for the 10 µm sample at 200 K.

To account for the presence of the contact resistance $R_c$ in our system, we subtract it from the total thermal resistance $R_{th}$.

### 4.8.2 Geometrical corrections

Before calculating the thermal conductivity we also need to take the contact geometry into account. As already mentioned in Section 4.7.1, the length of our heater is always bigger than the length of our slits. This could mean that both the applied power over the full heater is not equal to the power applied to the h-BN flake only, and that the $\Delta T_h$ measured over the full heater is not equal to the part of the $\Delta T_h$ caused by the h-BN flake. In our calculations of $\lambda_{hBN}$ we need to take both those factors into account.

#### 4.8.2.1 Corrections to the applied power

The power applied to heater can be divided in two parts. The first part of the applied power will go to the supported part of the h-BN flake that lies on top of $Si_3N_4$ membrane or simply $Si_3N_4$, left and right of the suspended flake. The second part of the applied power will go to the suspended h-BN flake.

Since the electrical resistance of the heater is the same over the whole heater, the applied electrical power $P$ will be also the same over the whole length of the heater. This means that to calculate the power $P_{hBN}$ applied to the suspended flake only, we simply can scale it with the ratio of the length of the suspended flake $l_{hBN}$ and the length of the heater $l_h$:

$$P_{hBN} = P \cdot \frac{l_{hBN}}{l_h}, \tag{4.45}$$

with $P_{hBN}$ the power applied to the suspended part of the h-BN flake only, $P$ the total applied power to the heater and $l_{hBN}$ and $l_h$ the length of the suspended part of h-BN flake and of the heater respectively.

For 2 µm slit sample $P_{hBN}$ contributes to 61% of the full applied power $P$, for 5 µm slit sample 18%, for the 7 µm slit sample 25% and for the 10 µm slit sample 33%.

#### 4.8.2.2 Corrections to the measured temperature differences

The temperature rise $\Delta T_h$ over the heater could be non-uniform. Part of the heater lies on top of either just $Si_3N_4$ or supported h-BN flake on top of the $Si_3N_4$. To estimate how the temperature rise over the suspended and the non-suspended part would relate to each other, we can use the compiled simulated COMSOL profiles (see Figure 4.19).

For the COMSOL simulation, the average $\Delta T_h$ over the full heater is equal to 0.7058 K, while the average temperature increase over the suspended flake only is 0.7836 K. This means that the measured $\Delta T_h$ would be 90% of the actual $\Delta T_h$ caused by the suspended h-BN. For the thermometer at the edge of the slit this percentage is even higher. The average temperature increase $\Delta T_{th}$ is 0.6093 K, corresponding to 97.4 % of the temperature increase due to the suspended h-BN flake (0.6254 K).

This would mean that a correction to the $\Delta T_h$ would make $\lambda_{hBN}$ smaller by 10%. This is an insignificant change (within the measurement uncertainty of our $\lambda_{hBN}$ values, see Appendix A) and can therefore be neglected.

### 4.8.3 Thermal conductivity

To calculate the thermal conductivity of our flakes, we need to keep both the thermal contact resistance in mind and the geometrical correction to the applied power. First we need to remove the contact resistance $R_c$, since it is either not dependent on the distance between the heater and thermometer or very weakly dependent. Then we need to apply the geometrical correction to the applied power (see Equation 4.45). If we apply both corrections, we can calculate the thermal conductivity $\lambda_{hBN}$ in the following way:

$$\lambda_{hBN} = \frac{l_{hBN}}{l_h} \cdot \frac{b_{hBN}}{2 \cdot l_{hBN} \cdot t_{hBN}} \cdot \left( \frac{\Delta T_{h-t}}{P} - R_c \right)^{-1}, \tag{4.46}$$

with $\lambda_{hBN}$ the thermal conductivity of h-BN flake, $\Delta T_{h-t}$ the temperature drop between the heater and thermometer, $P$ the full power applied to the heater, $R_c$ the thermal contact resistance, extracted from Figure 4.26a, $l_h$ the length of the heater, $l_{hBN}$ the length of the suspended h-BN flake (orthogonal to the heat flow), $b_{hBN}$ the width of the suspended h-BN flake (parallel to the heat flow) and $t_{hBN}$ the thickness of the suspended h-BN flake.

What needs to be taken into account with $R_c$ is that in Figure 4.26 the 7 µm sample shows a systematic deviation from the fit lines. If we then subtract the same contact resistance for this sample as for the others, we obtain an unproportionally high thermal conductivity and conductance for this sample. But if we assume that this deviation can fully be attributed to the difference in the thermal contact resistance $R_c$, rather than a systematic difference in $R_{th,hBN}$ of the 7 µm slit sample, we can estimate the thermal conductivity $\lambda_{hBN}$ of this sample in the following way:

$$\lambda^*_{hBN} = \frac{l_{hBN}}{l_h} \cdot \frac{b_{hBN}}{2 \cdot l_{hBN} \cdot t_{hBN}} \cdot \left( R_{th,fit} - R_c \right)^{-1}, \tag{4.47}$$

with $\lambda^*_{hBN}$ the estimated thermal conductivity the 7 µm slit sample and $R_{th,fit}$ the value taken from the fit line in Figure 4.26a at $b_{hBN}/2$ equal to 3.5 µm, the half-width of the 7 µm slit sample. This way we assume that the $R_c$ of the 7 µm slit sample

is equal to exactly the $R_c$ minus the difference between the measured $R_{th}$ and the expected $R_{th}$ from the fit:

$$R_c^* = R_c - \left( R_{th,fit} - \frac{\Delta T_{h-t}}{P} \right), \tag{4.48}$$

with $R_c^*$ the actual contact resistance of the 7 µm slit sample, $R_c$ the thermal contact resistance of the other three samples and $R_{th,fit}$ the value of the linear fit in Figure 4.26a at $b_{hBN}/2$ equal to 3.5 µm.

In Figure 4.27a one can see the thermal conductivity $\lambda_{hBN}$ for all four samples plotted as function of the bath temperature, indicated by the hollow circles. As predicted, the measured thermal conductivity for the 7 µm sample becomes unproportionally high due to the fact that the contact resistance $R_c$ is lower for this sample than for the others. In Figure 4.27b we show the same data as in Figure 4.27a, but replacing the thermal conductivity $\lambda_{hBN}$ of the 7 µm slit sample with the estimated $\lambda_{hBN}^*$ from Equation 4.47. In this panel, when we consider the estimated thermal conductivity $\lambda_{hBN}^*$ of the 7 µm slit sample, we see a clear thickness dependence for the thermal conductivity. The thermal conductivity seems to increase with the decreasing flake thickness.

In Figure 4.28a this trend if confirmed. Here we plot the sheet conductance (= $\lambda_{hBN} \cdot t_{hBN}$) of all four flakes as function of bath temperature. We only plot the $\lambda_{hBN}^*$ of the 7 µm sample. As one can see, all four curves fall on top of each other. This confirms that indeed the spread of the thermal conductivity in Figure 4.27b is due to the thickness spread of the flakes. In Figure 4.28b we plot $\lambda_{hBN}$ as function of the flake thickness. In this figure it is clear that the thermal conductivity decreases with increasing thickness. This is a consistent trend over the full bath temperature range.

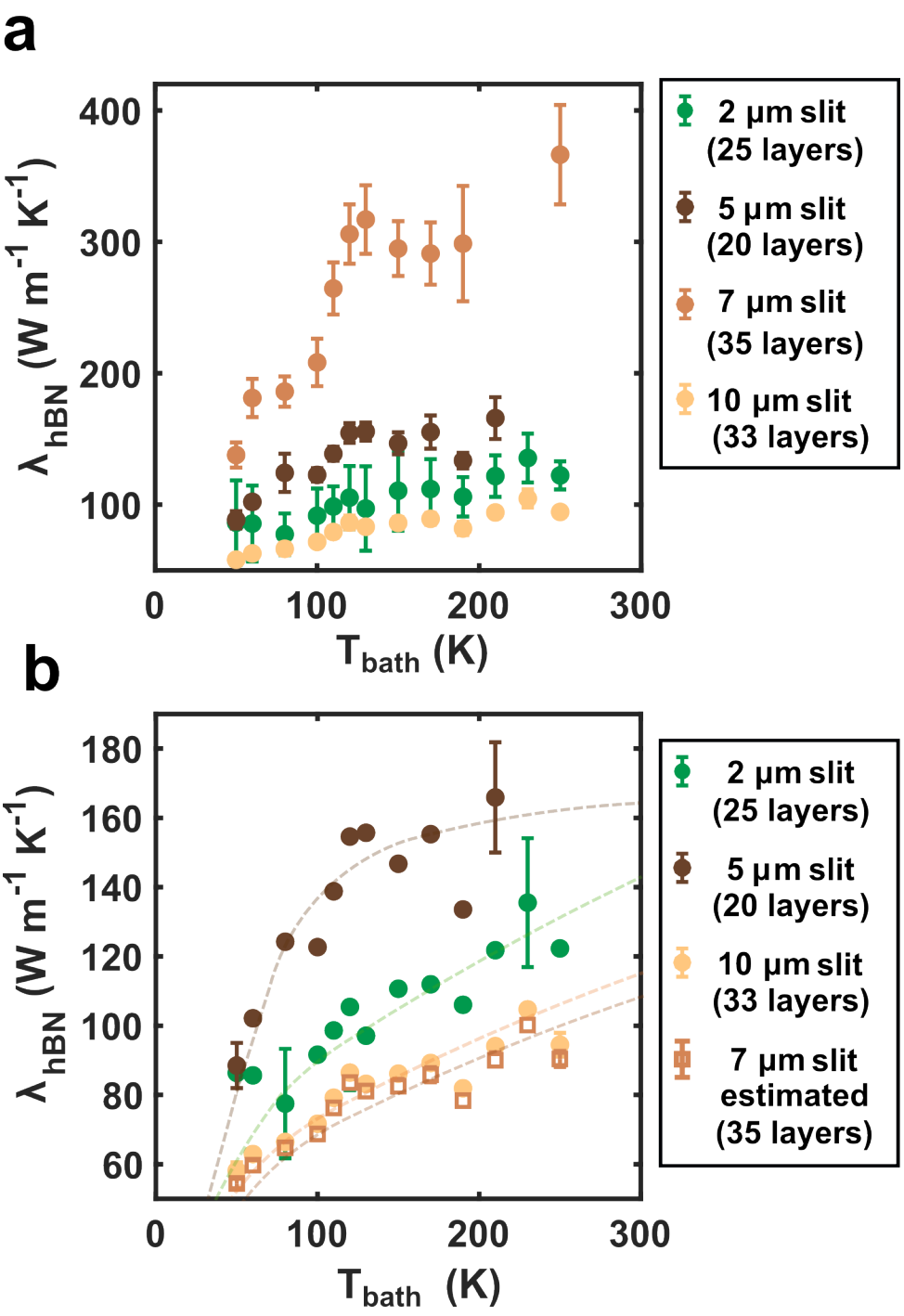


FIGURE 4.27: (a) Thermal conductivity of the h-BN flake $\lambda_{hBN}$ calculated from the measurements in Figure 4.22 for all four samples with the corresponding errorbars (b) Zoom-in of (a) showing all the curves, except for the 7 µm slit sample (filled circles). Additionally the estimated $\lambda^*_{hBN}$ of the 7 µm slit sample is shown (hollow squares), estimated using Equation 4.47. Two errorbars, at low and high bath temperature is shown for every curve, indicating the random error. Additionally, there can be up to 25% of systematic error present (see Appendix A for more details). The grayed out dashed lines serve as a guide to the eye.

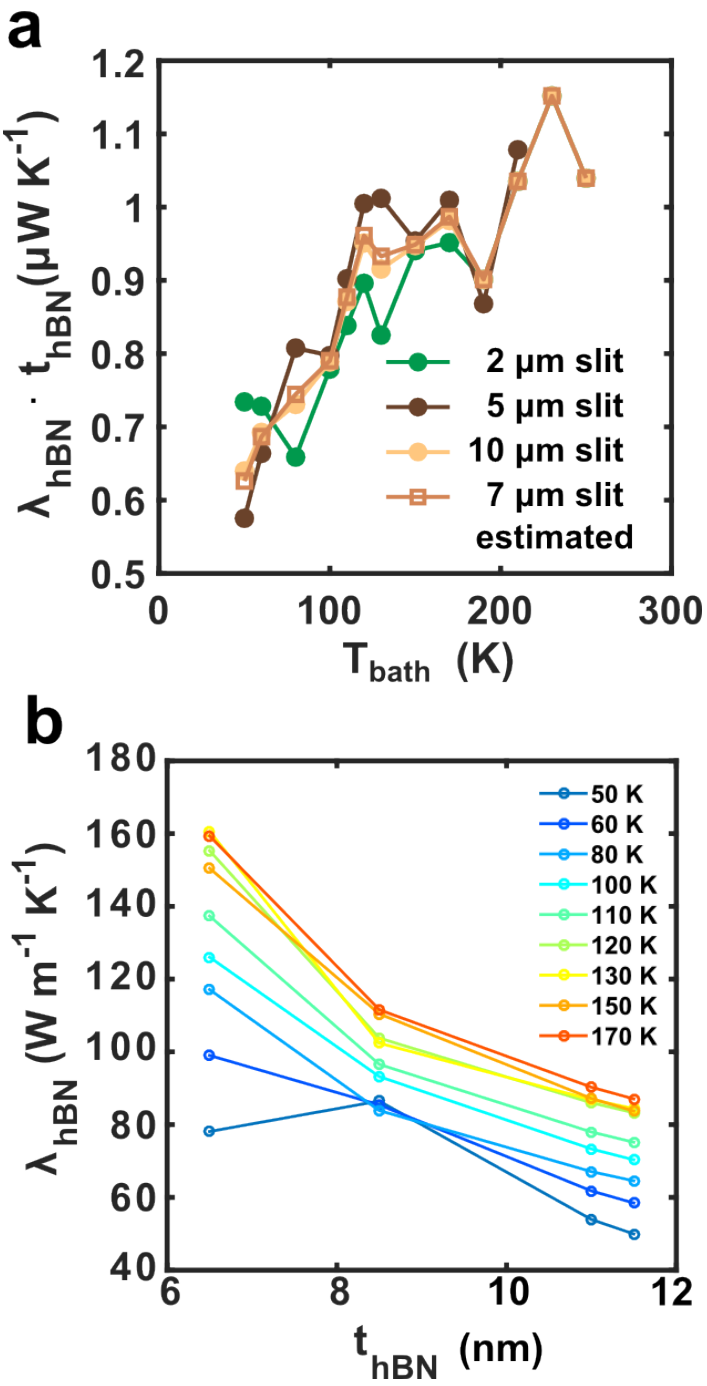


FIGURE 4.28: (a) The thermal conductivity $\lambda_{hBN}$ of three samples (2, 5 and 10 µm) and the estimated thermal conductivity $\lambda^*_{hBN}$ for 7 µm taken from Figure 4.27b, multiplied by the flake thickness $t_{hBN}$. (b) Thermal conductivity of h-BN as function of flake thickness for different bath temperatures. For the 7 µm slit the estimated data is shown.

### 4.8.4 Thermal diffusivity

If we take the slope of the linear part of the phase curves from Figure 4.24 we can obtain values for thermal diffusivity of the suspended h-BN flake $D_{hBN}$ in the following way:

$$t_0 = \frac{\Delta\phi}{4\pi f}, \tag{4.49}$$

$$D_{hBN} = \frac{b_{hBN}^2}{2t_0}, \tag{4.50}$$

with $D_{hBN}$ the thermal diffusivity of the h-BN, $\Delta\phi/f$ the slope of the linear part of the phase $\Delta\phi$, $b_{hBN}/2$ the half-width of the slit (parallel to the heat flow) and $t_0$ the average time it takes for changes in temperature to propagate from the heater to the thermometer. In Table 4.2 we list the values of $t_0$ for different samples and bath temperatures. All values are in the order of 1 to 10 µs.

TABLE 4.2: The times $t_0$, obtained from Figure 4.24 for different bath temperatures and different samples.

| | $T_{bath}$ = 50 K | $T_{bath}$ = 80 K | $T_{bath}$ = 150 K | $T_{bath}$ = 270 K |
|---|---|---|---|---|
| 2 µm slit | 4.0 µs | 0.95 µs | 5.5 µs | 7.8 µs |
| 5 µm slit | - | 6.2 µs | 7.1 µs | - |
| 7 µm slit | 8.0 µs | 14 µs | 19 µs | 31 µs |
| 10 µm slit | 4.8 µs | 6.0 µs | 9.3 µs | 13 µs |

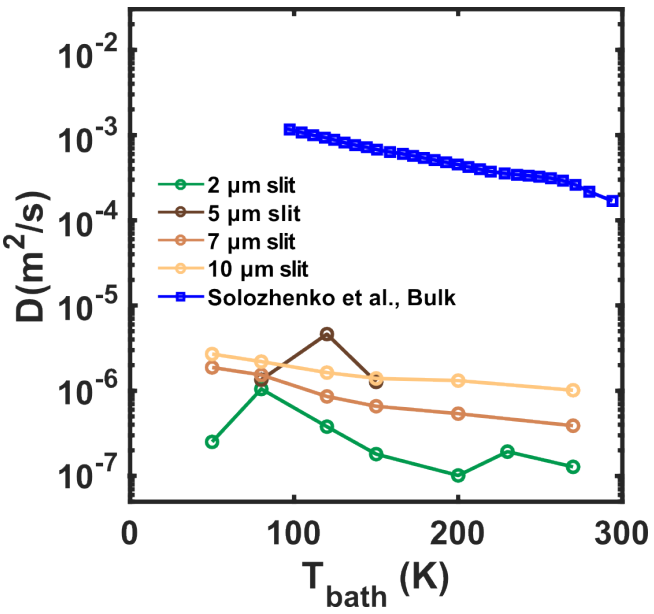


FIGURE 4.29: Thermal diffusivity $D$ as function of bath temperature $T_{bath}$ for all samples (open circles), compared to calculated $D_{hBN}$ values using heat capacity values measured by Solozhenko et al. [117] and thermal conductivity values measured by Sichel et al. [120] for bulk h-BN (blue squares). The measured values for the thermal diffusivity of h-BN $D_{hBN}$ were obtained using Equations 4.38 and 4.39.

In Figure 4.29 one can see the obtained thermal diffusivities with Equation 4.50 for the four samples (indicated by the hollow circles) and the calculated $D_{hBN}$ values using heat capacity values measured by Solozhenko et al. [117] and thermal conductivity values measured by Sichel et al. [120] for bulk h-BN (blue squares). Although the obtained shape of the curves is similar to the bulk h-BN values, our values are three to four orders of magnitude smaller than the values from Solozhenko and Sichel.

Additionally we modeled the low-frequency range (up to 200 Hz) with a square root function ($\Delta\phi \propto \sqrt{f}$), and obtained the proportionality factors $s_0$:

$$s_0 = \frac{\Delta\phi}{\sqrt{f}}, \tag{4.51}$$

with $\Delta\phi$ the phase difference for the frequencies up to 200 Hz and $f$ the frequency. In Table 4.3 one can see the values of $s_0$ for different samples and bath temperatures. Over-all the smaller samples, the 2 and 5 µm slits, show no clear bath temperature dependence, while the bigger samples, the 7 and 10 µm slits, show a clear decrease of $s_0$ with the bath temperature, going down by $\approx 40\%$ over a range of 200 K.

TABLE 4.3: The coefficients $s_0$, obtained from low-frequency region (f < 100 Hz) in Figure 4.24 for different bath temperatures and different samples.

$s_0$ in deg/Hz$^{1/2}$

| | $T_{bath}$ = 50 K | $T_{bath}$ = 80 K | $T_{bath}$ = 150 K | $T_{bath}$ = 270 K |
|---|---|---|---|---|
| 2 µm slit sample | 0.108 | 0.151 | - | -0.509 |
| 5 µm slit sample | - | 0.95 | 0.189 | - |
| 7 µm slit sample | 0.568 | 0.563 | 0.384 | 0.345 |
| 10 µm slit sample | 0.608 | 0.381 | 0.281 | 0.351 |

In a similar way as for our h-BN flakes, we can evaluate the phase difference between the heater and the second thermometer for the 5 µm sample. The material there is a bilayer, one layer being the 30 µm long $Si_3N_4$ membrane and the second layer being the supported h-BN flake on top of the membrane. This bilayer is in series with the suspended h-BN flake, but will dominate the phase difference due to its 10 times bigger length.

In Figure 4.30a one can see the averaged phase difference $\Delta\phi$ between the heater and the second thermometer as function of frequency. One can see that the phase difference is much higher than the ones measured for the h-BN flakes, between the heater and the first thermometer. This is expected, since the longer distance yields a bigger time $t_0$ and hence also a bigger phase difference. Again a square root dependence is present at the low frequencies and a linear part is present for the higher frequencies.

In Figure 4.30b we show the thermal diffusivity $D_{region}$ of the region between the first and second thermometer for the 5 µm sample. The thermal diffusivity is calculated with Equation 4.39 and the values from Figure 4.30a. Additionally we plot the literature values for the thermal diffusivity of a 100 nm $Si_3N_4$ membrane [118, 121] and of 500 nm $Si_3N_4$ membranes [112, 122]. For the latter, the values of specific heat from [118] are used to calculate the diffusivity. As one can see, our values are almost an order of magnitude higher than the literature values.

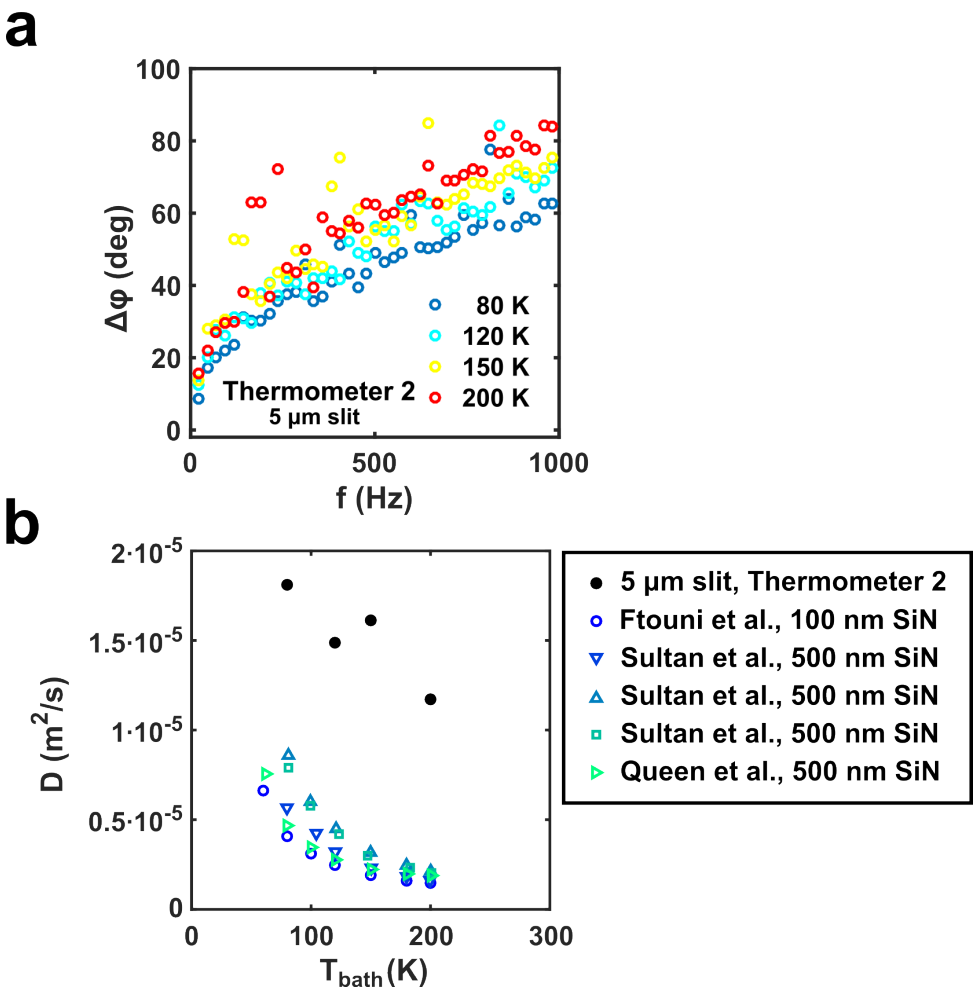


FIGURE 4.30: (a) Averaged phase difference $\Delta\phi$ between the heater and the second thermometer in degrees for the 5 µm sample, for different bath temperatures. (b) Thermal diffusivity $D_{region}$ of the region between the first and second thermometer for the 5 µm sample as function of bath temperature (black filled circles). Values for the thermal diffusivity $D_{SiN}$ of 100 nm thick $Si_3N_4$ membrane [118,121] and of various literature reports of 500 nm thick $Si_3N_4$ membranes [112,122]. For the latter, the values of specific heat from [118] are used to calculate the diffusivity.

We also calculate the square root proportionality factor $s_0$ for this thermometer. We obtain values of 3.33 deg/$Hz^{1/2}$ for 80 K and 2.97 deg/$Hz^{1/2}$ for 200 K. The values are an order of magnitude higher than the values calculated for the first thermometer. Although there is a significant decrease with the bath temperature (the absolute uncertainty of the values is $\approx$ 0.18 deg/$Hz^{1/2}$), relatively this decrease ( 11 % over 110 K) is a factor two smaller than the decrease of the 7 and 10 µm slit samples (28 % over 110 K).

### 4.8.5 1D Diffusion model

To check our obtained values for thermal conductivity and thermal diffusivity of h-BN, we also tried to model our data using the 1D model from Section 4.2.3. The model allows us to calculate both the $\Delta T_{th}$ (see Figure 4.22) and the phase $\Delta\phi$ (see

Figure 4.24) of a data set. This way the amplitude and the phase of each bath temperature measurement can both be modelled using the same set of fitting parameters.

We used the thermal conductivity of the $Si_3N_4$ membrane $\lambda_{SiN}$ and the thermal diffusivity of h-BN $D_{hBN}$ as fitting parameters. For the thermal conductivity of h-BN $\lambda_{hBN}$ we took our values from Figure 4.27, for the temperature difference at the heater $\Delta T_h$ we took our values from Figure 4.22 and for the diffusivity of $Si_3N_4$ $D_{SiN}$ we used Equation 4.4 and the values for $Si_3N_4$ heat capacity $c_{SiN}$ from Ftouni et al. [118]. For the length $L_1$ we took the half-width of the flake $b_{hBN}/2$ (parallel to the heat flow). For the length $L_2$ we took the length of the slit $l_{hBN}$ (orthogonal to the heat flow), presuming that 1D transport would only carry on for one square in the $Si_3N_4$ membrane, before spreading in the orthogonal direction to the heat flow as well.

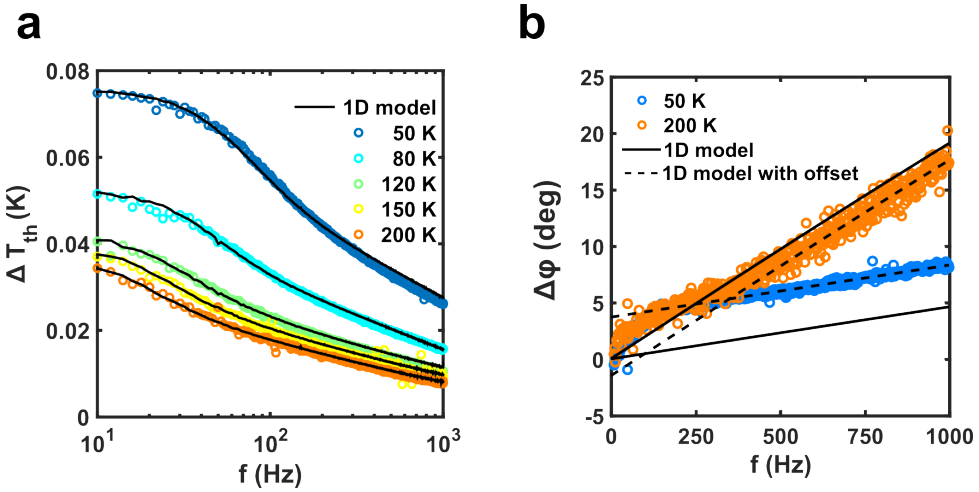


FIGURE 4.31: (a) Temperature difference at the thermometer $\Delta T_{th}$ as function of frequency for the 7 µm sample. The colored circles indicate data for different bath temperatures. The black lines indicate the theoretical fits. (b) The phase difference $\Delta\phi$ as function of frequency for two different bath temperatures for the 7 µm sample. The colored circles indicate the data and the black lines the theoretical fits. The dashed black lines indicate the fits with a small offset in the y-axis, to fit the data better.

In Figure 4.31 one can see the theoretical curves modeled using the 1D model for the 7 µm slit sample. We chose this sample as an example, because it has the lowest level of measurement noise. In Figure 4.31a we show the calculated temperature difference at the thermometer $\Delta T_{th}$ (black lines) compared to the measured data (hollow circles) as function of frequency. As one can see, the model reproduces the data quiet well. In Figure 4.31b we show the calculated phase difference $\Delta\phi$ (black lines) compared to the measured data (hollow circles) as function of frequency for the same sample. We could not reproduce the full curve of the $\Delta\phi$ with our model, but only the high-frequency linear part. Moreover, we had to offset our theoretical curve: the calculated phase curves always extrapolate to zero (solid black lines), while if we extrapolate the linear high frequency part of our measurement curves, it will not always cross the y-axis at zero (dashed black line). The square root low frequency part of the measurement could not be reproduced with this 1D model, even when changing the fitting parameters from the ones used to produce the theoretical curves in Figure 4.31.

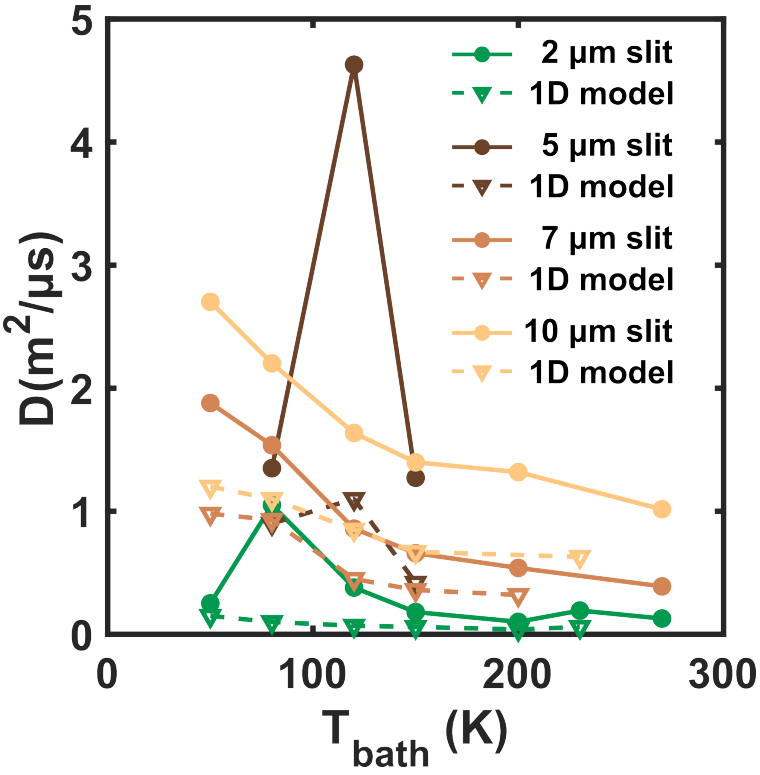


FIGURE 4.32: The thermal diffusivity $D_{1Dmodel}$ of all four samples obtained from the fits in using the our 1D diffusion model (see Section 4.2.3) as function of bath temperature (dashed lines with triangles) and the thermal diffusivity $D_{hBN}$ as function of bath temperature $T_{bath}$ for all samples (solid lines with filled circles), obtained using Equations 4.38 and 4.39.

We were able to reproduce the data of all four samples in a similar way as shown in Figure 4.31. One can find the graphs for the other samples in Appendix B. From the fitting parameters we could obtain the thermal diffusivity of h-BN $D_{1Dmodel}$, which one can see in Figure 4.32 (dashed lines with triangles). The values are very similar to the ones obtained by Equation 4.39 (solid lines with filled circles), and are still about three orders of magnitude smaller than the measured values for bulk h-BN from Solozhenko and Sichel.

The fact that we were able to explain the linear part of our phase data with a diffusive model and the long times obtained with Equation 4.38 (see Table 4.2) suggest that we are observing a diffusive process, rather than a ballistic or second sound one. The effective speed of the phonons ($v_{eff} = b_{hbN}/(2 \cdot t_0)$) would be in the order of 0.2-0.8 m/s, and according to [123] the acoustic longitudinal phonons have a sound velocity of 18.86 km/s, while the slower transverse phonons have a sound velocity of 11.86 km/s. We do not know the orientation of our flake with respect to the heater, but both velocities are four orders of magnitude higher than the observed velocities in our samples.

In Figure 4.33 one can see the values of thermal conductivity of $Si_3N_4$ $\lambda_{SiN,fit}$ obtained from the fitting parameters used for the curves in Figure 4.31, for all four different samples. As one can see the values of $\lambda_{SiN,fit}$ for 2 µm slit sample (Figure 4.33a) are unrealistically high, being even higher than our values for the thermal conductivity of h-BN $\lambda_{hBN}$. Yet for the other samples (Figure 4.33b-d) the values are only slightly higher than the values from Sikora et al. [95] (1-5 W $m^{-1}$ $K^{-1}$). Since the

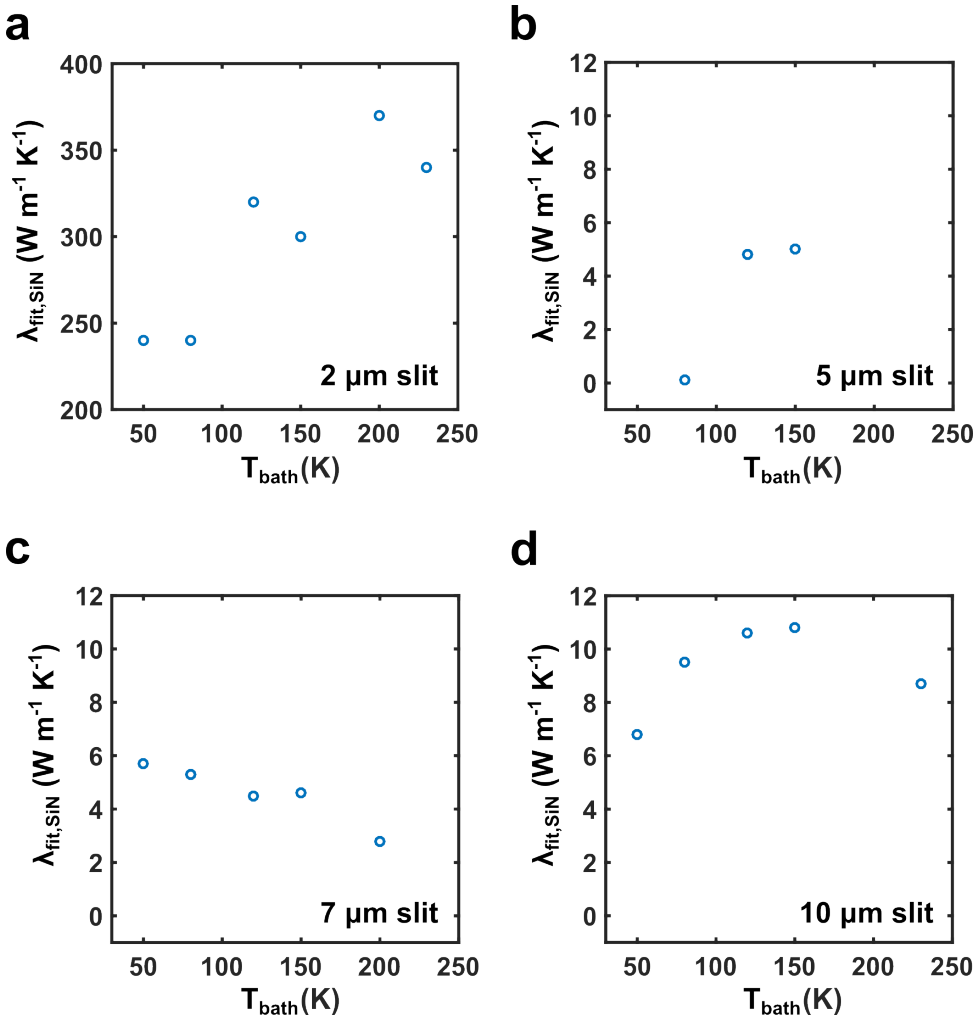


FIGURE 4.33: The obtained fit values for thermal conductivity $\lambda_{SiN,fit}$ for silicon nitride membrane, using our 1D diffusion model (see Section 4.2.3). (a) 2 µm slit sample (b) 5 µm slit sample (c) 7 µm slit sample (d) 10 µm slit sample.

region after the thermometer is partly covered with supported h-BN flake we can argue that the values indeed should be slightly higher, since an additional parallel channel for thermal transport is added for part of the membrane. A conductivity higher by a factor of 1.5-2 is then not that unexpected.

The bath temperature dependence of the curves in Figure 4.33 is not always the same as in Sikora's work [95]. We expect a slow rise for lower bath temperatures and a saturation for higher bath temperatures. This behavior is only visible for the 10 µm sample, and could be present for the 5 µm sample. The other two samples show a different curve shape. This deviation in shape and for the 2 µm sample also deviation in order of magnitude leaves doubts whether our theoretical model is fully correct.

### 4.8.6 2D COMSOL simulation

We can compare the measured temperature differences with the ones obtained using a 2D COMSOL simulation (see Section 4.6). For this purpose we use the values from low-frequency regime, where the $\Delta T_h$ and $\Delta T_{th}$ are relatively constant. What we also need to take into account is the contact resistance $R_c$, which was not taken into account in the model. The contact resistance would yield an additional temperature difference between the heater and thermometer:

$$\Delta T_{Rc} = R_c \cdot P, \tag{4.52}$$

with $\Delta T_{Rc}$ the temperature increase caused by the contact resistance, $R_c$ the thermal contact resistance in and $P$ the total applied power to the heater.

For a bath temperature $T_{bath}$ of 200 K, as used in the simulation, $\Delta T_{Rc}$ would be equal to 104 mK. In Table 4.4 one can see all the temperature differences, at the heater and both thermometers, compared. As one can see the absolute value of those differences is at least 3-10 times higher than what we measure. Yet the temperature drop between the heater and the first thermometer, if you add $\Delta T_{Rc}$ to the drop obtained by the model (see last column), is in very good agreement.

This simulation also allows us to check whether our expression for thermal conductivity $\lambda_{hBN}$ (Equation 4.46) indeed reproduces the input thermal conductivity, if we use the $\Delta T_h$ and $\Delta T_{th}$ from the COMSOL simulation. Since there is no contact resistance $R_c$ in the simulation, Equation 4.46 becomes:

$$\lambda_{hBN} = \frac{l_{hBN}}{l_h} \cdot \frac{b_{hBN}}{2 t_{hBN} l_{hBN}} \cdot \frac{P}{\Delta T_{h-t}}, \tag{4.53}$$

with $l_{hBN}$ and $t_{hBN}$ the length (orthogonal to the heat flow) and the thickness of the h-BN flake. For our simulation we set them to be 10 µm and 11 nm, respectively. $l_h$ is the length of the heater, 33 µm. $b_{hBN}/2$ is the half-width of the flake, here 5 µm. $P$ is the applied power, for the simulation we used a value of 0.65 µW. $\Delta T_{h-t}$ is the temperature drop between the heater and the first thermometer. As one can see in Table 4.4, for our simulation it is equal to 0.09 K.

If we then calculate the thermal conductivity $\lambda_{hBN}$ using the input parameters and the computed $\Delta T_{h-t}$ we obtain a value of 99.48 $Wm^{-1}K^{-1}$, which is very close to our input thermal conductivity of 100 $Wm^{-1}K^{-1}$. This shows that Equation 4.46 indeed shows the proper way of calculating $\lambda_{hBN}$ from the measured $\Delta T_{h-t}$.

TABLE 4.4: Comparison of the COMSOL simulation and measured values, with $\Delta T_h$ the average temperature difference at the heater in K, with $\Delta T_{th}$ the average temperature difference at the first thermometer in K, with $\Delta T_{th2}$ the average temperature difference at the second thermometer in K and $\Delta T_{Rc}$ the temperature difference in K caused by the thermal contact resistance $R_c$.

| | $\Delta T_h$ (K) | $\Delta T_{th}$ (K) | $\Delta T_{th2}$ (K) | $\Delta T_h$ - $\Delta T_{th}$ (K) | ($\Delta T_h$ - $\Delta T_{th}$) + $\Delta T_{Rc}$ (K) |
|---|---|---|---|---|---|
| COMSOL | 0.7 | 0.61 | 0.36 | 0.09 | 0.194 |
| Measured | 0.25 | 0.045 | 0.027 | - | 0.205 |

## 4.9 Discussion

### 4.9.1 Contact resistance

As mentioned in Section 4.8.1 we observe a rather high thermal contact resistance $R_c$ in our samples, which contributes at least 50% of the full thermal resistance $R_{th}$ for 50 K and at least 30% for 200 K. There are several possible causes to such a thermal resistance. Firstly we could be observing a thermal interface resistance, also called Kapitza resistance, between either the heater and the h-BN flake or the h-BN flake and the $Si_3N_4$ membrane. Secondly there could be some stress present in the h-BN flake due to the van der Waals forces pulling it towards the edges of the slit (see Figure 4.14), and this could cause distortions and kinks with a thermal resistance. Thirdly there could be a layer of adsorbates, PMMA residues or impurities between the heater and the h-BN flake, since the surface of the flake could become contaminated during the fabrication of the heater. In this section we consider all three of those possibilities.

First, we consider the possibility of the thermal interface resistance. Using the predicted Kapitza interface resistances between metals or $SiO_2$ and graphene [124, 125], we can estimate what our Kapitza interface resistance between the heater and the h-BN should be. With the calculated Kapitza resistance being in the order of $1{\cdot}10^{-8}$ K m$^2$/W and the interface area for us being $3.3{\cdot}10^{-10}$ m$^2$, we would obtain an interface thermal resistance of only $3{\cdot}10^3$ K/W. For the interface between the flake and the $Si_3N_4$ the interface resistance would be even smaller due to a bigger overlap area. Yet we observe a thermal contact resistance of about $0.2\text{-}0.3{\cdot}10^6$ K/W, which is at least two orders of magnitude bigger. So it is unlikely that our $R_c$ is caused by the Kapitza resistances.

Secondly, we consider a possibility of a kink in the flake with a high thermal resistance. In a work by Dolleman et al. [126] there is a mention of such high thermal resistance. There they study thermal transport in suspended graphene drums and observe thermal interface resistances as high as $4{\cdot}10^6$ K/W, which is two orders of magnitude higher than the predicted Kapitza resistances for graphene interfaces with $SiO_2$ [125].

In the follow-up paper [127] Dolleman et al. explore the possibility of a kink in the flake at the border of the suspended drum being the reason for such high thermal resistances. They calculate the reflectance probability for different phonons (LA, TA and ZA) at such a kink and predict very strong angle dependence of the reflectance. For example, for out-of-plane (ZA) phonons the transmission is only possible at very small angles around 0, while all other angles will be reflected. The original paper [126] estimates the total phonon transmission probability to be as low as $3{\cdot}10^{-3}$.

In the work by Dolleman et al. [126] the conditions of the graphene drums are similar to ours. The depth of the slit is 300 nm, which is similar to our 200 nm. The circular slits have diameters between 3 and 7 µm, which is comparable to our slits of 2-10 µm. The main differences are the thickness of the flakes (single layer graphene is only 0.337 nm thick, while we have h-BN flakes of 6-11 nm thick) and the shape of the slit. Yet it is not unreasonable to think that we also could have such a kink in the flake at the border of our slits.

We can estimate what our thermal resistance would be for our geometry, using the formula from Dolleman et al. [127]:

$$R_{kink} = \frac{1}{G_{kink} \cdot t_{hBN} \cdot Pr_{slit}}, \tag{4.54}$$

with $R_{kink}$ the thermal resistance caused by the kink, $G_{kink}$ the thermal interface conductance, $t_{hBN}$ thickness of the h-BN flake and $Pr_{slit}$ the perimeter of the slit.

If we take the value of $G_{kink}$ from Dolleman et al. [126] ($30 \pm 20 \cdot 10^6$ W m$^2$ K$^{-1}$), and calculate $R_{kink}$ for our four samples, we obtain numbers in the order of 0.1-0.6 K/µW. Taking into account that the value of the thermal interface conductance is measured at room temperature, our numbers for thermal contact resistance are of the same order of magnitude (see Figure 4.26), although closer to the lower bound.

Using another formula from [126] we can also estimate the time delay caused by such a kink:

$$\tau_{kink} = \frac{\rho_{hBN} \cdot c_{hBN} \cdot b_{hBN}}{4 \cdot G_{kink}}, \tag{4.55}$$

with $\tau_{kink}$ being the thermal RC-time of the kink, $\rho_{hBN}$ the mass density of h-BN flake, $c_{hBN}$ the specific heat of the h-BN flake, $b_{hBN}$ the width of the flake, orthogonal to the heat flow, and $G_{kink}$ the thermal interface conductance.

If we again use the value from [126] for $G_{kink}$ we obtain values of 65 ns for the 2 µm slit sample and 350 ns for the 10 µm slit sample.

If this kink indeed is the cause of our contact resistance $R_c$, then it would be inversely proportional to the width of the slit $b_{hBN}$, but we do not see such a dependence. Moreover, in the 10 µm slit sample our thermometer is positioned before the slit edge, on the suspended part of the h-BN flake. For all three other samples the thermometer is positioned right outside of the slit, after the slit edge. If such a kink indeed was the reason for the observed thermal contact resistance, we would have seen a smaller or even absent $R_c$ for the 10 µm slit sample as compared to the other three samples. Yet we do not see such a behavior. Therefore we can conclude that our contact resistance is not caused by a kink in the flake.

As a third cause of our $R_c$, we consider a layer of adsorbates or impurities between the heater and the h-BN flake. In the work of Jaber et al. [128] the authors calculate that even a relatively thin layer (2 nm thick) below the heater of 100 nm width (as is the case for our samples) could create an additional 40% increase in the temperature difference $\Delta T_h$ at the heater, which in turn would lead to an overestimation of measured thermal conductance. We observe similar numbers: 35-50% of the full thermal resistance is due to the thermal contact resistance.

We can check if it is possible that we have a diffusive layer of several nanometers thick below our heater. We can calculate the thermal conductivity corresponding to our thermal contact resistance using Equation 4.34 and the dimensions of the heater:

$$\lambda_c = \frac{t_{ab}}{l_h \cdot b_h} \cdot \frac{1}{R_c}, \tag{4.56}$$

with $\lambda_c$ the effective thermal conductivity of the potential interface adsorbates layer, $t_{ab}$ the thickness of the potential adsorbates layer, $R_c$ the thermal contact resistance, obtained from Figure 4.26 and $l_h$ and $b_h$ the length and width of the heater respectively.

If we take a thickness of the adsorbates layer $t_{ab}$ around 1-5 nm, we obtain a thermal conductivity $\lambda_c$ as high as 1000-5000 W m$^{-1}$ K$^{-1}$, which is unreasonably high for a layer of adsorbates. For comparison: the thermal conductivity of PMMA is 0.19 W m$^{-1}$ K$^{-1}$ at room temperature [129]. This suggests that the thermal resistance we are seeing is most likely not arising due to a diffusive mechanism, but rather a barrier for phonons with a non-zero reflectance probability.

So, the most viable explanation for this contact resistance is a reflective barrier below the heater, possibly formed by a thin layer of adsorbates or impurities. If

this is the case, we can try to model this situation using the Debye model and the effusion model (see Appendix E for more details). We take as a basis a box with phonons, with a small orifice, through which the phonons can escape, and modify this effusion model to our case: instead of an orifice we have a reflective box wall, with a small transmission probability. The phonons inside the heater are represented as the phonons in the box, the adsorbates layer serves as a reflective barrier and the phonons that manage to travel from the heater to the h-BN flake are the phonons that escaped the box. With this model we can express $R_c$ in the following way:

$$R_c = (A \cdot \mathcal{T} \cdot u_h \cdot \rho_h c_h)^{-1}, \tag{4.57}$$

with $R_c$ the thermal contact resistance, $A$ the cross-section area of the heater, $\mathcal{T}$ the transmission probability, $u_h$ the speed of sound within the heater material, $\rho_h$ the density of the heater material and $c_h$ the specific heat of the heater material. Within the Debye model [130] we can express $\rho_h c_h$ as:

$$\rho_h c_h(T) = 9k_B \left[\frac{N_{heater}}{V_{heater}}\right] \left[\frac{T}{T_{D,h}}\right]^3 \int_0^{T_{D,h}/T} \frac{x^4 e^x}{(e^x-1)^2} dx, \tag{4.58}$$

with $T$ the bath temperature, $k_B$ the Boltzmann constant, $T_{D,h}$ the Debye temperature of heater and $N_{heater}/V_{heater}$ number density of atoms in the heater. The speed of sound $u_h$ can be expressed in terms of $T_{D,h}$ as:

$$u_h = \left[\frac{\pi \cdot V_{heater}}{6 \cdot N_{heater}}\right]^{1/3} \frac{2k_B \cdot T_{D,h}}{h}, \tag{4.59}$$

with $V_{heater}$ the total volume of the heater, $N_{heater}$ the amount of atoms in the heater, $k_B$ the Boltzmann constant, $T_{D,h}$ the Debye temperature of heater and $h$ the Planck's constant.

Our heater consists of 10 nm titanium and 30 nm gold. We can calculate an weighed average of the Debye temperature of the heater in the following way:

$$T_{D,h} = \frac{t_{Ti} \cdot T_{D,Ti} + t_{Au} \cdot T_{D,Au}}{t_{Ti} + t_{Au}}, \tag{4.60}$$

with $t_{Ti}$ and $t_{Au}$ the thicknesses of titanium and gold respectively and $T_{D,Ti}$ and $T_{D,Au}$ the Debye temperatures of the titanium and gold respectively. Taking $T_{D,Ti}$ = 420 K and $T_{D,Au}$ = 170 K from [131], we calculate $T_{D,h}$ to be 232.5 K. Using this value of $T_{D,h}$ we can calculate the speed of sound $u_h$ with Equation 4.59, obtaining a value of 3.05 km/s.

We use two fitting parameters, $T_{D,h}$ and $\mathcal{T}$, and obtain the values of 230 K and $2.5{\cdot}10^{-4}$ respectively. The value of the Debye temperature is very close to the value calculated with Equation 4.60, which supports the validity of Equation 4.57.

In Figure 4.34 one can see our $R_c$ values as function of the bath temperature $T_{bath}$ (hollow circles) and the calculated values using effusion model using Equation 4.57 (dashed line). The model shows very good agreement with the data. From the Equation 4.57 we extract the transparency of our interface barrier: $2.5{\cdot}10^{-4}$. This confirms the hypothesis of the $R_c$ being caused by a highly reflective barrier.

### 4.9.2 Thermal conductivity

As mentioned in section 4.8.3, we observe a clear thickness dependence of our values of $\lambda_{hBN}$, the thermal conductivity decreases with increasing thickness. This thickness dependence is in contrast to what has been measured by Jo et al. [32] where they

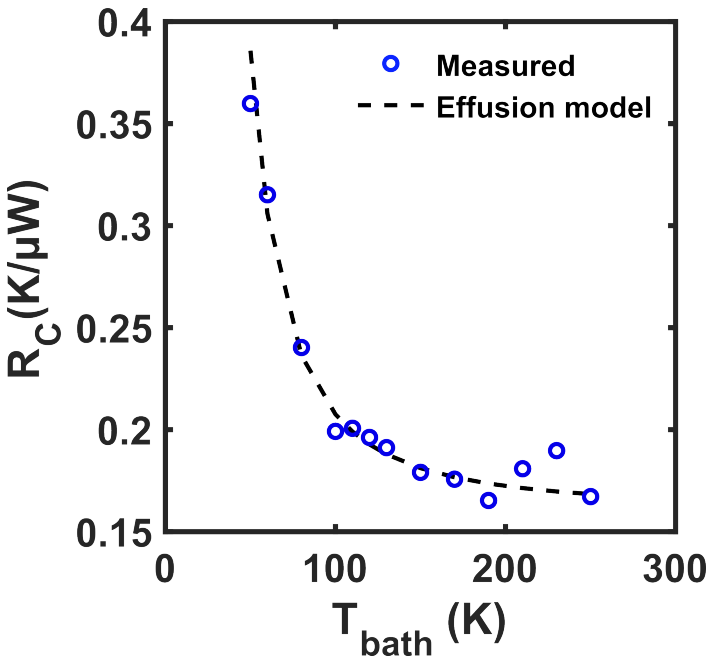


FIGURE 4.34: The thermal contact resistance $R_c$ as function of the bath temperature (hollow circles), and the calculated $R_c$ using Debye model (dashed line), see Equation 4.57. We use the following fitting parameters: $T_{D,h}$ = 230 K, $\mathcal{T}$ = 2.5·10$^{-4}$.

observed an increase of thermal conductivity from a 5 layer to 11 layer sample, rather than a decrease with the thickness, as is the case in our samples. Jo et al. explained it by the presense of the PMMA-residues that could reduce the thermal conductivity in the affected top layer of the flake. Since this would have a higher effect on a thinner sample than the thicker one, it would explain why the 11 layer sample showed a higher thermal conductivity.

Yet, other findings from literature do not confirm Jo's thickness trend. In Figure 4.35a one can see our measured values of $\lambda_{hBN}$ from Figure 4.27b, and in Figure 4.35b one can see values for different flake thicknesses from literature. The blue and cyan squares indicate the measurements from Jo et al. [32] for 5 and 11 layers sample respectively. The red hollow triangles show the measurements of an h-BN bilayer [132] by Wang et al., the black filled triangles show the values for bulk by Sichel et al. [120] and the magenta dashed line shows a theoretical prediction for an h-BN monolayer [133] by Lindsay et al.. As you can see the bilayer measured by Wang et al. has a thermal conductivity as high as the 11 layer from Jo et al., which was explained in their work by the lack of PMMA-residues on the bilayer. But then the monolayer prediction by Lindsay shows an even higher thermal conductivity, which again contradicts the trend of the samples from Jo et al..

In the theoretical work by Lindsay et al. [133] they argue that indeed a thickness dependence of the thermal conductivity would be present, with decreasing thermal conductivity with increasing thickness. This trend is explained by the high contribution of the out-of-plane phonon modes to the thermal conductivity. With increasing thickness those modes become suppressed in the middle layers of the flake, reducing the thermal conductivity. Yet the calculation shown in the work predicts a significant change in thermal conductivity only between the monolayer and the bilayer. After the bilayer, the thermal conductivity quickly starts to saturate. It is therefore not a good explanation for a visible trend in our much thicker samples (20-35 layers).

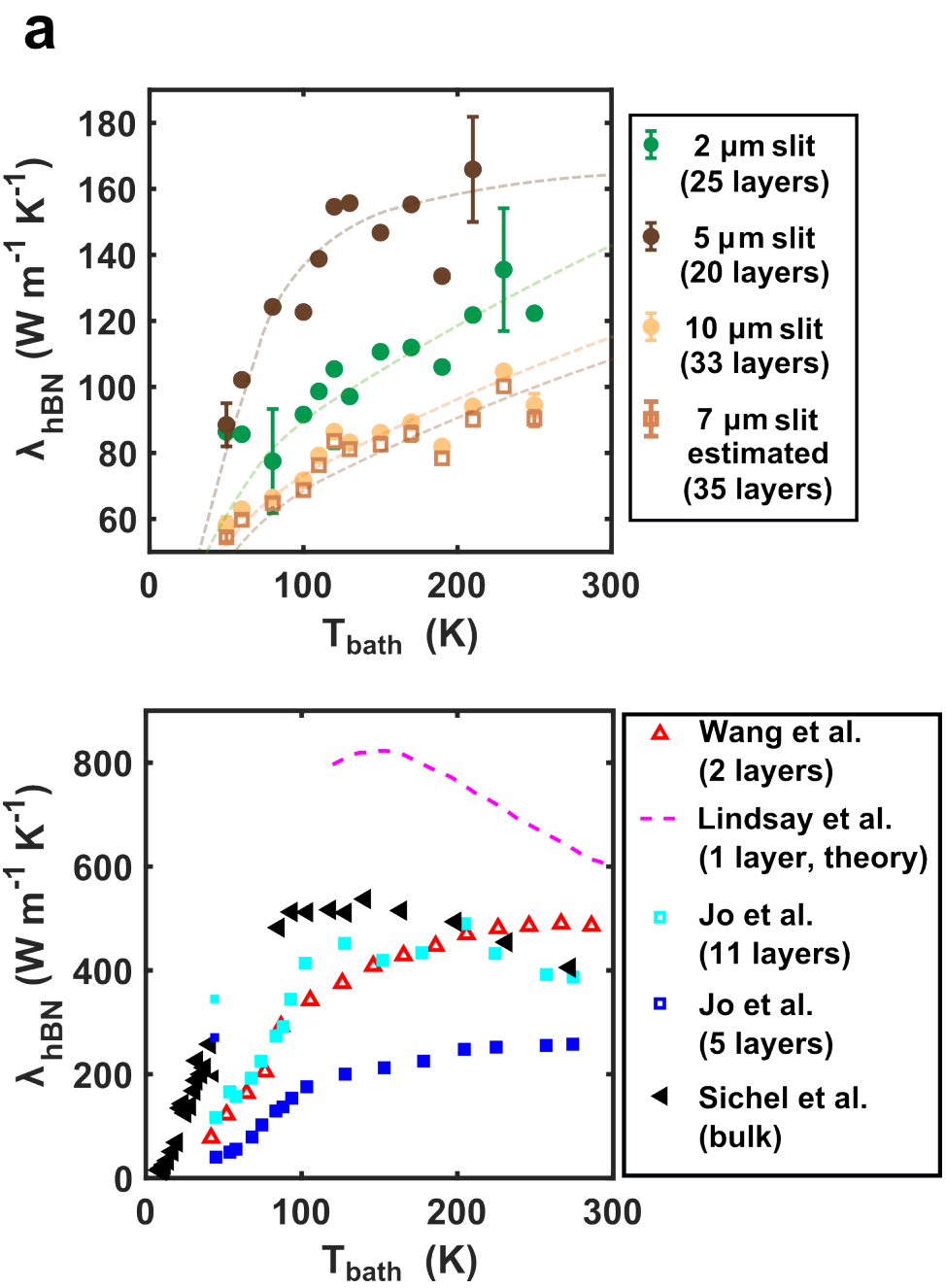


FIGURE 4.35: (a) Thermal conductivity of h-BN $\lambda_{hBN}$ for all four samples as function of $T_{bath}$, except for the 7 µm slit sample (filled circles). Additionally the estimated $\lambda^*_{hBN}$ of the 7 µm slit sample is shown (hollow squares), estimated using Equation 4.47. Two errorbars, at low and high bath temperature is shown for every curve. The grayed out dashed lines serve as a guide to the eye. (b) Comparison from literature [32, 120, 132, 133], showing experimentally measured thermal conductivity of h-BN samples with 2 (red hollow triangles), 5 and 11 atomic layers (blue and cyan squares respectively), bulk (black triangles) and the theoretically predicted thermal conductivity of monolayer h-BN (magenta dashed line).

Independently of the thickness trend, our measured thermal conductivity values are the same order of magnitude as the measurements of Jo et al. [32] and Wang et al. [132], being the closest to the Jo's 5 layers sample. Our samples also show a similar bath temperature dependence as all other measured samples from literature: a slow rise of thermal conductivity at low bath temperatures up to 100-120 K and a certain saturation of thermal conductivity from 100-120 K on.

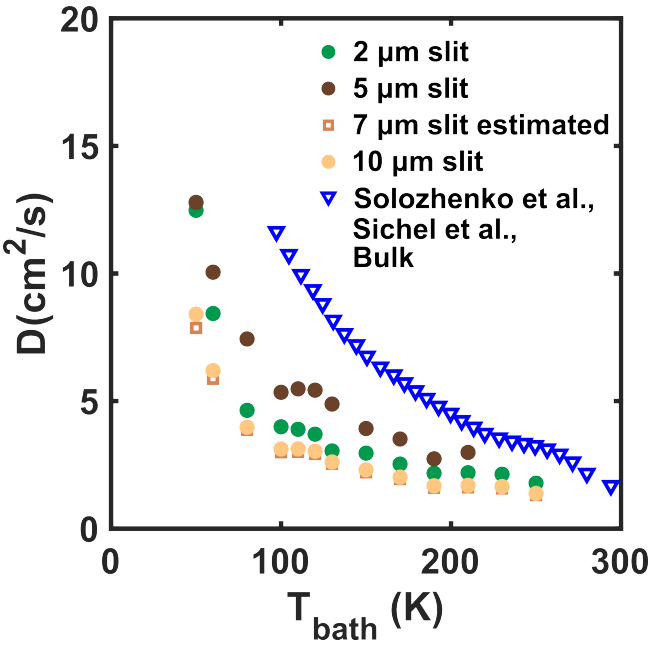


FIGURE 4.36: Thermal diffusivity of h-BN $D_{hBN}$ calculated using Equation 4.4 from the values in Figure 4.27b as function of $T_{bath}$ for 2, 5 and 10 µm slit samples (filled circles). Additionally the calculated $D_{hBN}$ from the estimated $\lambda^*_{hBN}$ (see Equation 4.47) of the 7 µm slit sample is shown (hollow squares). The hollow blue triangles show the bulk thermal diffusivity, calculated using the heat capacity values of Solozhenko et al. [117] and the thermal conductivity values of Sichel et al. [120].

Using the heat capacity from Solozhenko et al. [117] we calculated the corresponding thermal diffusivity from our thermal conductivity values by using Equation 4.4. In Figure 4.36 one can see the values of $D_{hBN}$ calculated using the values of $\lambda_{hBN}$ (filled circles) and the estimated $\lambda^*_{hBN}$ of the 7 µm slit sample (hollow squares) from Figure 4.27b. The hollow blue triangles indicate the bulk thermal diffusivity, calculated using the heat capacity values of Solozhenko et al. [117] and the thermal conductivity values of Sichel et al. [120]. As one can see, our curves show the same bath temperature dependence and the same order of magnitude as the values from Solozhenko and Sichel.

Using the h-BN heat capacity values from the work of Solozhenko et al. [117], we also calculated the mean free path $\Lambda_{ph}$ by combining Equations 4.4 and 4.5:

$$\lambda_{hBN} = \frac{1}{2} \cdot u_{hBN} \cdot \Lambda_{ph} \cdot \rho_{hBN} c_{hBN}, \tag{4.61}$$

with $\lambda_{hBN}$ the thermal conductivity of h-BN, $u_{hBN}$ the average phonon speed of sound, $\Lambda_{ph}$ the phonon mean free path within h-BN, $\rho_{hBN}$ the mass density of h-BN and $c_{hBN}$ the specific heat of h-BN. The speed of sound $u_{hBN}$ can be expressed in terms of the Debye temperature [130]:

$$u_{hBN} = \frac{a_{hBN} \cdot k_B \cdot T_D}{\hbar}, \tag{4.62}$$

with $a_{hBN}$ the atomic spacing of h-BN, $k_B$ the Boltzmann constant, $T_D$ the Debye temperature of h-BN and $\hbar$ the reduced Planck's constant.

We use $T_D$ = 1000 K as the Debye temperature that gives the best Debye approximation for the heat capacity values of Solozhenko et al. [117] and McDonald et al. [134]. We take $a_{hBN}$ = 0.246 nm from [120] and calculate $u_{hBN}$ to be 3.22 km/s using Equation 4.62.

In Figure 4.37a one can see the obtained values of $\Lambda_{ph}$ as function of the bath temperature $T_{bath}$, compared with the bulk h-BN $\Lambda_{ph}$, which we calculate using the heat capacity values from Solozhenko et al. [117] and the thermal conductivity values from Sichel et al. [120]. The order of magnitude and the bath temperature dependence are very similar. Both follow an exponential temperature dependence.

This exponential behaviour can be explained by the dominant scattering mechanism. The exponential dependence suggests that the dominant scattering process is the umklapp process, where the scattering time $\tau_0$ is proportional to $\exp(T/T_0)$, with $T_0$ a temperature of the same order of magnitude as the Debye temperature [135]. Since the mean free path is equal to the product of the scattering time and the speed of sound ($\Lambda_{ph} = u_{hBN} \cdot \tau_0$), $\Lambda_{ph}$ will also have an exponential bath temperature dependence if the umklapp scattering dominates the mean free path. We were able to approximate both our samples and the bulk data using:

$$\Lambda_{ph} = \Lambda_0 \cdot \exp\left(\frac{T_0}{T}\right), \tag{4.63}$$

with fitting parameters $\Lambda_0$ equal to 11 nm and $T_0$ to 182 K for the bulk, and 8 nm and 114 K for our samples. Such a low temperature suggests that the phonons contributing to the thermal transport are most likely situated in the lowest acoustic branches, where the energy varies between 0 and 20 meV (0 and 232 K) [136]. The slightly lower $T_0$ in our samples could mean that in the few-layer flakes the energy of the lowest acoustic modes could be less than in the bulk, possibly due to a higher mechanical flexibility.

In Figure 4.37b one can see the $\Lambda_{ph}$ multiplied with the thickness $t_{hBN}$ as function of the bath temperature together with exponential fit using Equation 4.63 (dashed line). As one can see, the scatter between the points is the highest for the low temperatures, being $\approx$ 70 nm$^2$ for 50 K, but for the higher bath temperatures the curves almost fall on top of each other, with the scatter below 1 nm$^2$ for 250 K. The data are in very good agreement with Equation 4.63, which suggests that in this temperature regime the umklapp process dominates all other scattering mechanisms, including the temperature-independent boundary and impurity scattering.

In Figure 4.37c one can see the bulk h-BN values of $\Lambda_{ph}$ calculated using the data from Solozhenko and Sichel (blue triangles), as function of bath temperature, together with an exponential fit using Equation 4.63 (dashed line). Here the data show deviations from the exponential curve at lower and higher temperatures. Most likely, at lower temperatures the curve deviates due to the umklapp peak in the heat capacity, where $\Lambda_{ph}$ is still temperature-independent, while at the higher temperatures the higher energy branches start to contribute with a higher $T_0$.

As mentioned in the introduction, so far there is no consensus about the phonon mean free path in few-layer h-BN. The predictions of $\Lambda_{ph}$ range between 30 nm and 550 nm in different studies [32, 88–91]. For example, Jo et al. [32] estimate $\Lambda_{ph}$ to be

550 nm for 11 layers and 180 nm for the 5 layers for bath temperatures below 100 K. Our values in Figure 4.37 are at the lower end of the predicted spectrum.

Of course, we use relatively simple models to explain our data. Debye model is mostly reliable for very low ($T \ll T_D$) and very high ($T \gg T_D$) bath temperature regimes, while our temperature range is somewhere in between. Moreover we consider all the energy branches simultaneously, taking an average speed of sound using the Debye temperature (see Equation 4.62). More complicated models can be used to approximate the thermal conductivity and the corresponding mean free path, taking into account the full dispersion relation [133, 136], but although they probably will introduce certain corrections, the order of magnitude of obtained $\Lambda_{ph}$ is not likely to change.

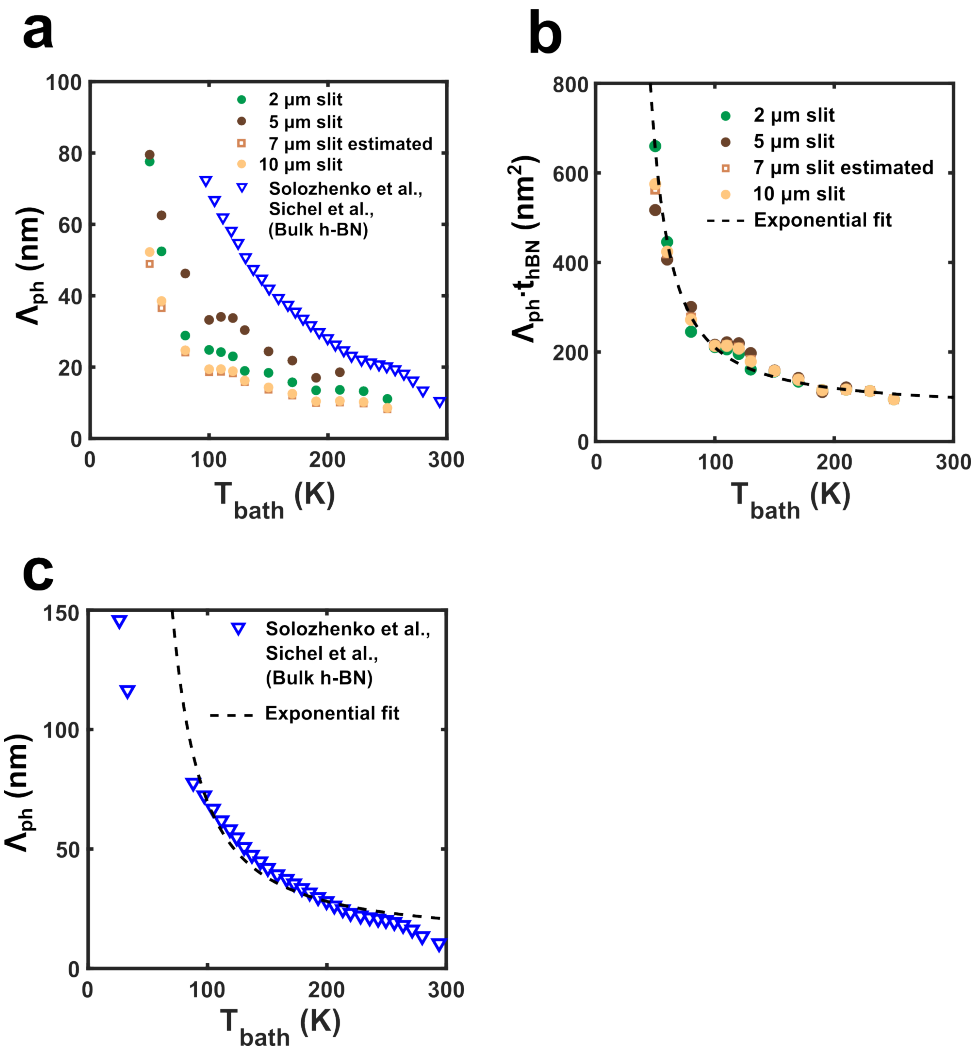


FIGURE 4.37: (a) The phonon mean free path $\Lambda_{ph}$ obtained from the Debye model, as function of bath temperature. For the 7 µm slit sample we use the estimated values (see Equation 4.47). The blue triangles indicate the calculated $\Lambda_{ph}$ from the heat capacity values from Solozhenko et al. [117] and the thermal conductivity values from Sichet et al. [120]. (b) The $\Lambda_{ph}$ from (a) for our samples multiplied with the thickness $t_{hBN}$ as function bath temperature. The dashed line indicates an exponential fit using Equation 4.63. Fitting parameters: $\Lambda_0$ = 8 nm, $T_0$ = 114 K. (c) The calculated $\Lambda_{ph}$ from the heat capacity values from Solozhenko et al. [117] and the thermal conductivity values from Sichet et al. [120] as function of $T_{bath}$ (blue triangles). The dashed line indicates an exponential fit using Equation 4.63. Fitting parameters: $\Lambda_0$ = 11 nm, $T_0$ = 182 K.

### 4.9.3 Thermal diffusivity

Additionally to calculating the thermal diffusivity from our thermal conductivity values using Equation 4.4, we also were able to calculate $D_{hBN}$ independently, from the phase shift $\Delta\phi$ (see Figure 4.32). We use the linear high-frequency part of the phase shift and calculate the diffusivity using Equation 4.39. The obtained values are about three to four orders of magnitude lower than the bulk h-BN values from Solozhenko and Sichel [117, 120]. As mentioned in Section 4.8.5 we were able to reproduce the linear part of the phase shift using the 1D diffusion model from Section 4.2.3, but we had to introduce an offset, since the linear part of the phase does not extrapolate to zero. The values of $D_{hBN}$ calculated with the 1D model were very similar to the ones obtained using Equation 4.39, and were again three to four orders of magnitude smaller than the bulk values.

Because our values for the thermal conductivity $\lambda_{hBN}$ do match the order of magnitude from literature [32, 120, 132], this big deviation for the thermal diffusivity would mean either the violation of Equation 4.4 ($D = \lambda/(\rho \cdot c_p)$) or that specific heat of our samples is different than the values for the bulk [117]. The second possibility seems unreasonable, since it would mean that the heat capacity of h-BN would increase by three to four orders of magnitude from bulk to few-layer form.

Our low $D_{hBN}$ values would also mean an unreasonably low phonon mean free path, when calculated from the diffusivity by rewriting Equation 4.5 and presuming the 1D case, where $F_0$=1/2 (2D geometry):

$$\Lambda_{ph} = 2 \cdot D_{hBN}/u_{hBN}. \tag{4.64}$$

With our diffusivity values and using the calculated value of the speed of sound using Equation 4.62 (3.22 km/s), we would obtain values of 1-7 Å for the phonon mean free path, which is unrealistically low. The literature values of the $\Lambda_{ph}$ for h-BN vary between 30 nm and 550 nm at room temperature in different studies [32, 88–91]. Our $\Lambda_{ph}$ values obtained using Equation 4.61 (see Figure 4.37) vary between 8.5 nm (250 K) and 80 nm (50 K).

The reason that we need an offset for the linear curves calculated with the 1D model, is that we have a small square root part in the low-frequency region of our phase curves. In Figure 4.24 one already saw the two different regimes: square root dependence for low-frequency regime (f < 200 Hz) and linear dependence for high-frequency regime (f > 200 Hz). This square root dependence at lower frequencies was predicted in the 1D diffusion equation solution by Carslaw and Jaeger [137], but that solution was for semi-infinite solid, which is not fully applicable to our case. Several papers successfully adapted their solution for systems similar to ours [138–145], but in the Morikawa et al. [145] work the authors mention that this solution would not be applicable for our geometry, since we do not comply with the condition of $\Delta\phi \cdot b_{hBN}/2 > 1$. Nevertheless we can evaluate the square root coefficients $s_0$ using the solution proposed by Carslaw and Jaeger:

$$D_{hBN} = \pi \cdot \left(\frac{b_{hBN}}{2}\right)^2 \left[\frac{\Delta\phi}{\sqrt{f}}\right]^2 = \pi \cdot \left(\frac{b_{hBN}}{2}\right)^2 [s_0]^2, \tag{4.65}$$

with $D_{hBN}$ the thermal diffusivity of h-BN, $b_{hBN}/2$ the half-width of the h-BN flake, $\Delta\phi$ the phase shift between the heater and thermometer, $f$ the frequency and $s_0$ the square root proportionality coefficient between the phase shift and the frequency ($= \Delta\phi/\sqrt{f}$).

If we use our values of $s_0$, obtained from Figure 4.24 (see Section 4.8.4), we can calculate $D_{hBN}$ for our samples. Yet, the values calculated using Equation 4.65 are even smaller than the values obtained from the linear region of the phase, in the order of $0.1 \cdot 10^{-7}$ $m^2/s$ for 50 K and $0.5 \cdot 10^{-7}$ $m^2/s$. This is five orders of magnitude lower than the Solozhenko and Sichel bulk diffusivity values [117,120] and one order of magnitude lower than the values obtained from the linear region of the phase (see Figure 4.29).

A possible explanation for such unrealistically low thermal diffusivity values, both from the square root part and the linear part, would be a slow component in the system that would increase the total time $t_0$, while not affecting the static $\lambda_{hBN}$ values, leading to the underestimation of $D_{hBN}$. A good candidate would be the time delay caused by the thermal contact resistance $R_c$. We can calculate this total RC-time in the following way:

$$\tau_{R_c} = c_h \cdot \rho_h \cdot V_{heater} \cdot R_c, \tag{4.66}$$

with $\tau_{R_c}$ the thermal RC-time of the thermal contact resistance, $c_h$ the specific heat of the heater material, $\rho_h$ the mass density of the heater material, $V_{heater}$ the volume of the heater and $R_c$ the thermal contact resistance.

Taking the values of specific heat for gold from [116], we calculate $\tau_{R_c}$ to be 66 ns for 50 K and 54 ns for 250 K. This is two to three orders of magnitude lower than our values of $t_0$. Therefore this could not explain our high $t_0$ values.

Another explanation for such low $D_{hBN}$ values would be that we observe a different type of thermal transport in our samples, which cannot be properly explained by a diffusive model. This hypothesis is supported by the fact, that our values of the thermal diffusivity $D_{region}$ of joint region, consisting of the h-BN/$Si_3N_4$ bilayer and $Si_3N_4$, obtained from the measurements at the second thermometer in the 5 µm slit sample (see Figure 4.30) are not that far from the literature values.

If the actual diffusivity values of h-BN would match the values from bulk h-BN of Solozhenko and Sichel, as we expect from Equation 4.4 ($D = \lambda / (\rho \cdot c_p)$), the mixed thermal diffusivity $D_{region}$ of the region between the first and second thermometer would have been higher than the diffusivity of the $Si_3N_4$ membrane alone. This is in agreement with what we see for our values of $D_{region}$ (see Figure 4.30). This agreement confirms the validity of the analysis.

So, our method for calculating the diffusivity from the phase shift is correct, but the obtained $D_{hBN}$ values are too small. This supports the conclusion, that the phase shift in our h-BN flakes can not be correctly evaluated with a diffusive model, since our method is based on it. Moreover, the two different frequency regimes of the phase $\Delta\phi$ and the discrepancy between the obtained $\Lambda_{ph}$ values from our $\lambda_{hBN}$ values using Equation 4.4 and the $\Lambda_{ph}$ values obtained using $D_{hBN}$ values suggest that the dominant thermal transport mechanism at lower frequencies (f < 200 Hz) and higher frequencies (f > 200 Hz) might be different in nature.

# Chapter 5

# Conclusion

We have characterized the optoelectronic properties of two few-layer $In_2Se_3$ phototransistors, measuring the current in dark and under illumination. We have determined the dominant photocurrent generating mechanism in our samples by extracting the coefficients $\alpha$ from the relation between the effective power $P_{eff}$ and the photocurrent $I_{ph}$. We have found that the dominant photocurrent generating mechanism can be tuned using the back gate: fast photoconduction in the OFF state and high gain photogating in the ON state.

According to our analysis the photogating in the ON state is caused by long-lived hole traps between the flake and the substrate. They cause an ultrahigh gain, but reduce the speed of the transport. The sample with the bigger amount of trap states (the top contact device) showed a better responsivity, while the sample with the lower amount of trap states (the pre-patterned contact device) showed a faster response.

For our top contact device we calculate a responsivity of ($R \approx 105$ A/W) for a bias voltage of 50 mV, and a detectivity of $3 \cdot 10^{13}$ Jones. This is one of the best reported results for 2D materials in literature [23–31] and makes $In_2Se_3$ a good candidate for future photodetection applications.

We have introduced a modified $3\omega$ method. For the investigation of thermal transport in 2D materials we added thermometers at the end of the suspended flake to be able separate the flake and the substrate.

We observe a systematic thermal contact resistance $R_c$ in our samples. This resistance is unusually big and is likely caused by a reflective layer of absorbates or impurities between the heater and the h-BN flake. We could approximate the bath temperature dependence of $R_c$ with the Debye model, calculating a transmission probability of 0.025%.

We have measured the thermal conductivity of four suspended h-BN flakes and found a clear thickness dependence, with decreasing $\lambda_{hBN}$ as the thickness increases. The values are all in the order of 100 W $m^{-1}$ $K^{-1}$ and are in good agreement with the other values reported for few-layer h-BN by Jo et al. [32] and Wang et al. [132]. Using the values of heat capacity from Solozhenko et al. [117] we were able to calculate both the mean free path and the thermal diffusivity using our thermal conductivity values. The calculated diffusivity is in good agreement with bulk h-BN diffusivity [117, 120]. The calculated mean free path in our samples shows an exponential temperature dependence, indicating that the umklapp scattering is the dominant scattering mechanism in our flakes. The values of thermal conductivity are confirmed by both the 2D COMSOL simulation for zero frequency and the 1D analytical diffusion model.

We have calculated the thermal diffusivity of our samples using the high-frequency linear regime of the phase shift between the heater and thermometer. The obtained

values are in the order of 1 $mm^2/s$ and about three to four orders of magnitude lower than the bulk diffusivity values [117, 120]. We were able to reproduce the high-frequency linear part of our phase shift with the 1D analytical diffusion model, but not the low-frequency square root part. This indicates that there are two different thermal transport regimes present in our samples, one at lower frequencies and one at higher frequencies, and that our phase shift can not be properly explained by a diffusion model only.

# Appendix A

# Error analysis

## A.1 Thermal conductivity of h-BN

As mentioned in Section 4.8.3, we can calculated the thermal conductivity of a suspended h-BN flake in the following way:

$$\lambda_{hBN} = \frac{b_{hBN}}{2 \cdot l_{hBN} \cdot t_{hBN}} \cdot \frac{l_{hBN}}{l_h} \cdot \left( \frac{\Delta T_{h-t}}{P} - R_c \right)^{-1} = \frac{b_{hBN}}{2 \cdot l_h \cdot t_{hBN}} \cdot (R_{th,hBN})^{-1}, \quad \text{(A.1)}$$

with $\lambda_{hBN}$ the thermal conductivity of h-BN, $\Delta T_{h-t}$ the temperature drop between the heater and the thermometer, $b_{hBN}/2$ the half-width of the h-BN flake (parallel to the heat flow), $l_{hBN}$ the length of the h-BN flake (orthogonal to the heat flow), $t_{hBN}$ the thickness of the h-BN flake, $P$ the total applied power to the heater, $l_h$ the length of the heater, $R_c$ the thermal contact resistance and $R_{th,hBN}$ the thermal resistance of the h-BN flake.

To calculated the error of the obtained value, we use the formula for the propagation of error:

$$\epsilon_{f(x_1,x_2,x_3,...)} = \sqrt{\left( \epsilon_{x_1} \cdot \frac{\partial f}{\partial x_1} \right)^2 + \left( \epsilon_{x_2} \cdot \frac{\partial f}{\partial x_2} \right)^2 + \left( \epsilon_{x_3} \cdot \frac{\partial f}{\partial x_3} \right)^2 + ...}, \quad \text{(A.2)}$$

with $f(x_1, x_2, x_3, ...)$ the quantity in question and $\epsilon_{x_n}$ the absolute error of any quantity it may depend on.

It is important to separate the systematic error, which is reproducible and is the same for all measurements of one sample, and the statistical error, which varies from measurement to measurement. In our case the only source of statistical error in the thermal conductivity is the uncertainty of temperature difference $\Delta T_{h-t}$. We obtain this uncertainty from a RMSE fit to the low-frequency constant part in Figure 4.22, and this RMSE value is different for every bath temperature.

The uncertainties of the applied power $P$ and the length scales ($l_h$, $w_{hBN}$, $t_{hBN}$) are systematic and are caused by the limited precision of our equipment, the lock-in, the SEM and the AFM. The uncertainty of the thermal contact resistance $R_c$ is obtained from the RMSE of the linear approximation of $R_{th}$ as function of the distance $b_{hBN}/2$, and is the same for all samples. Therefore it also systematic.

In the case of the thermal conductivity $\lambda_{hBN}$ we estimate the measurement uncertainties of the length scales ($l_h$, $w_{hBN}$, $t_{hBN}$) and the temperature difference $\Delta T$. For the estimation of the error of applied power $\epsilon_P$ and the thermal resistance of h-BN $R_{th,hBN}$ we need to use Equation A.1.

### A.1.1 Measurement uncertainty of the applied power

We calculate the applied power in the following way:

$$P = (I_h)^2 \cdot R_h, \tag{A.3}$$

with $I_h$ the current through the heater and $R_h$ the electrical resistance of the heater.

Considering the Wheatstone bridge of the heater (see Figure 4.11), and the fact that both branches have an equal electrical resistance ($R_1 = R_2$ and $R_v = R_h$ in the balanced state), we can expresse the current $I_h$ in the following way:

$$I_h = \frac{V_s}{R_1 + R_h + 2R_{pre}}, \tag{A.4}$$

with $I_h$ the current through the heater, $R_1$ the constant resistance in the branch of the heater, $R_h$ the electrical resistance of the heater and $R_{pre}$ the pre-resistance of the heater Wheatstone bridge.

Combining both equations, we can express $P$ as:

$$P = \frac{V_s^2 \cdot R_h}{(R_1 + R_h + 2R_{pre})^2}. \tag{A.5}$$

Then we can write the systematic relative error of $P$ as:

$$\frac{\epsilon_P}{P} = \sqrt{\left[\frac{2\epsilon_{V_s}}{V_s}\right]^2 + \frac{P_h}{V_s^2 R_h}\left(\left[\frac{\epsilon_{R_h}(R_1 - R_h + 2R_{pre})}{R_h(R_1 + R_h + 2R_{pre})^2}\right]^2 + [2\epsilon_{R_1}]^2 + \left[4\epsilon_{R_{pre}}\right]^2\right)}, \tag{A.6}$$

with $\epsilon_P$ the absolute error of the applied power $P$, $\epsilon_{R_1}$ the absolute error of the constant resistor in the Wheatstone bridge, $\epsilon_{R_{pre}}$ the absolute error of the pre-resistor before the Wheatstone bridge, $\epsilon_{R_h}$ the absolute error of the heater resistance and $\epsilon_{V_s}$ the absolute error of the source voltage.

From the specification of the Standford SR830 we know that for a source voltage $V_s$ of 550 mV an uncertainty $\epsilon_{V_s}$ of 11 mV is present. This corresponds to a relative error of 2%. For the resistances $R_{pre}$ of 10 kΩ and $R_1$ of 330 Ω we estimate the systematic uncertainty to be 10 Ω and 0.5 Ω respectively. This corresponds to relative errors of 0.1% and 0.15% respectively. This is as precise, as we can measure those resistances. The uncertainty of the $R_h$ we can estimate from the precision with which it was possible to balance the Wheatstone bridge, which is 50 mΩ. This corresponds to a relative error of 0.01%.

As such, we obtain a relative systematic uncertainty of the applied power $P$ of 4%.

### A.1.2 Measurement uncertainty of the h-BN thermal resistance

The thermal resistance of the h-BN flake $R_{th,hBN}$ is defined in the following way:

$$R_{th,hBN} = \frac{\Delta T_{h-t}}{P} - R_c, \tag{A.7}$$

with $R_{th,hBN}$ the thermal resistance of the h-BN flake, $\Delta T_{h-t}$ the temperature drop between the heater and the thermometer, $P$ the full power applied to the heater and $R_c$ the thermal contact resistance in the system.

To estimate the measurement uncertainty of $\Delta T_{h-t}$ we take a look at the constant part of the $\Delta T_h$ and $\Delta T_{th}$ as function of the frequency (see Figure 4.22). If we fit that difference of those two graphs with a constant line, we get an RMSE (Root Mean Square Error with respect to the fit) value of the data. This error is bath temperature independent, varying relatively randomly. For the 2 µm sample it is 4.8 mK (3.8%) for 50 K and 1.9 mK (2.1%) for 250 K. For the 5 µm sample it is 4.7 mK (2.2%) for 50 K and 4.2 mK (3.1%) for 210 K. For the 7 µm sample it is 3.2 mK (1.2%) for 50 K and 2.3 mK (1.6%) for 250 K. For the 10 µm sample it is 5.1 mK (1.7%) for 50 K and 3.7 mK (1.8%) for 250 K.

To estimate the error of the thermal contact resistance $R_c$ we do the same: we look at the RMSE of the fit of the full thermal resistance $R_{th}$ as function of the distance between the heater and the thermometer (see Figure 4.26). For different bath temperatures the RMSE is between $1.45{\cdot}10^3$ (50 K) and $9.08{\cdot}10^3$ K/W (250 K). This gives a relative error up to 2.5 %.

The absolute statistical error of $R_{th,hBN}$ is solely dependent on $\Delta T_h$ and will be equal to:

$$\alpha_{R_{th,hBN}} = \frac{\epsilon_{\Delta T_{h-t}}}{P}, \tag{A.8}$$

with $\alpha_{R_{th,hBN}}$ the absolute statistical error of the thermal resistance of h-BN, $\epsilon_{\Delta T_{h-t}}$ the absolute error of the temperature difference $\Delta T_{h-t}$ and $P$ the applied power.

We calculate $\alpha_{R_{th,hBN}}$ to be 15.4 K/mW (37.3%) for 50K and 4.2 K/mW (8.8%) for 250 K for the 2 µm sample, 11.7 K/mW (7.4%) for 50K and 8.1 K/mW (9.6%) for 210 K for the 5 µm sample, 5.59 K/mW (7.0%) for 50K and 3.12 K/mW (10.3%) for 250 K for the 7 µm sample and 10.7 K/mW (4.1%) for 50K and 5.8 K/mW (3.6%) for 250 K for the 10 µm sample.

The absolute systematic error of the thermal resistance of h-BN $R_{th,hBN}$ can be expressed in the following way:

$$\beta_{R_{th,hBN}} = \sqrt{\left[\frac{\epsilon_P \cdot \Delta T_{h-t}}{P^2}\right]^2 + [\epsilon_{R_c}]^2}, \tag{A.9}$$

with $\beta_{R_{th,hBN}}$ the absolute systematic error of the thermal resistance of h-BN, $\Delta T_{h-t}$ is the temperature drop between the heater and thermometer, $P$ the total applied power to the heater, $\epsilon_P$ the absolute error of the applied power and $\epsilon_{R_c}$ the absolute error of the thermal contact resistance.

We calculate $\beta_{R_{th,hBN}}$ to be 18.4 K/mW (44.7%) for 50K and 8.7 K/mW (18.1%) for 250 K for the 2 µm sample, 22.6 K/mW (14.3%) for 50K and 10.7 K/mW (12.7%) for 210 K for the 5 µm sample, 19.8 K/mW (24.7%) for 50K and 8.0 K/mW (26.6%) for 250 K for the 7 µm sample and 26.4 K/mW (10.1%) for 50K and 13.1 K/mW (8.2%) for 250 K for the 10 µm sample.

### A.1.3 Measurement uncertainty of the thermal conductivity

We obtain our length scales from SEM images and can estimate the uncertainty of the length and width of the flake to be not more than 200 nm. For the 2 µm slit sample and 5 µm slit sample the uncertainty of the half-width is 50 nm, for 7 µm slit sample it is 80 nm and for the 10 µm slit sample it is 200 nm. This gives a relative

error up to 5 % for the half-width of the flake and up to 0.6 % for the length of the heater.

For the AFM measurement of the thickness $t_{hBN}$ we estimate a measurement uncertainty of 0.5 to 1 nm. So $\epsilon_{t_{hBN}}$ = 1 nm. This gives a relative error not more than 15 %.

The statistical relative error of $\lambda_{hBN}$ can be expressed as:

$$\frac{\alpha_{\lambda_{hBN}}}{\lambda_{hBN}} = \frac{\alpha_{R_{th,hBN}}}{R_{th,hBN}}, \tag{A.10}$$

with $\frac{\alpha_{\lambda_{hBN}}}{\lambda_{hBN}}$ the relative statistical error of thermal conductivity of h-BN and $\frac{\alpha_{R_{th,hBN}}}{R_{th,hBN}}$ the relative statistical error of the thermal resistance of the h-BN.

Rewriting Equation A.1 we can write the relative systematic error of the thermal conductivity $\lambda_{hBN}$ as:

$$\frac{\beta_{\lambda_{hBN}}}{\lambda_{hBN}} = \sqrt{\left[\frac{\beta_{R_{th,hBN}}}{R_{th,hBN}}\right]^2 + \left[\frac{\epsilon_{l_h}}{l_h}\right]^2 + \left[\frac{\epsilon_{t_{hBN}}}{t_{hBN}}\right]^2 + \left[\frac{\epsilon_{b_{hBN}}}{b_{hBN}}\right]^2}, \tag{A.11}$$

with $\beta_{\lambda_{hBN}}/\lambda_{hBN}$ the relative systematic error of the thermal conductivity of h-BN, $\beta_{R_{th,hBN},sys}/R_{th,hBN}$ the relative systematic error of the thermal resistance of h-BN, $\epsilon_{l_h}/l_h$ the relative error of the heater length, $\epsilon_{b_{hBN}}/b_{hBN}$ the relative error of the width of the flake (parallel to the heat flow) and $\epsilon_{t_{hBN}}/t_{hBN}$ the relative error of the thickness of the h-BN flake.

In Figure A.1 one can see the calculated relative statistical error in % (Figure A.1a) and relative systematic error in % (Figure A.1b), as function of bath temperature.

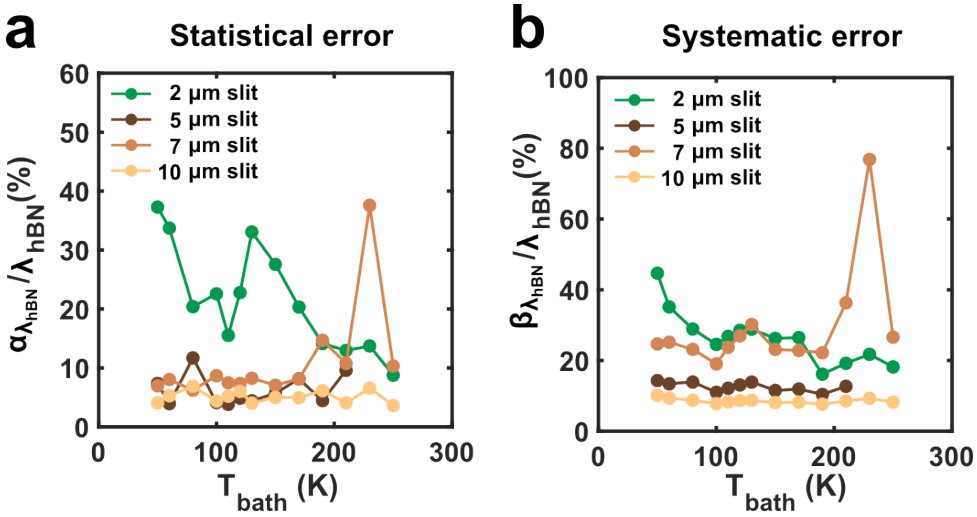


FIGURE A.1: The relative error of the thermal conductivity of h-BN $\epsilon_{\lambda_{hBN}}/\lambda_{hBN}$ of our conductivity values in Figures 4.27a and 4.27b, in percent, as function of bath temperature $T_{bath}$, for all four samples (filled circles). (a) The relative statistical error. (b) The relative systematic error.

## A.2 Thermal diffusivity of h-BN

The thermal diffusivity $D_{hBN}$ depends on two quantities: the distance between the heater and thermometer $b_{hBN}/2$, which has a systematic error, and the time $t_0$ the

heat flow travels this distance. The latter has a statistical error, that varies from sample to sample and from measurement to measurement.

We can express the relative statistical error of $D_{hBN}$ in the following way:

$$\frac{\alpha_{D_{hBN}}}{D_{hBN}} = \frac{\epsilon_{t_0}}{t_0}, \tag{A.12}$$

with $\epsilon_{t_0}/t_0$ the relative error of $t_0$. We can obtain $\epsilon_{t_0}$ from the standard deviation of our linear approximation of the high-frequency part of the phase (f > 200 Hz). It is equal to 240 ns (6.4%) for 50 K and 658 ns (8.4%) for 270 K for the 2 µm slit sample, 576 ns (9.3%) for 80 K and 637 ns (8.9%) for 150 K for the 5 µm slit sample, 103 ns (1.6%) for 50 K and 389 ns (1.2%) for the 7 µm slit sample, 169 ns (4.8%) for 30 K and 403 ns (3.2%) for 270 K for the 10 µm slit sample.

We can express the relative systematic error of $D_{hBN}$ in the following way:

$$\frac{\beta_{D_{hBN}}}{D_{hBN}} = \frac{2 \cdot \epsilon_{b_{hBN}}}{b_{hBN}/2}, \tag{A.13}$$

with $\epsilon_{b_{hBN}}/(b_{hBN}/2)$ the relative error of the distance between the heater and the thermometer. The uncertainty of $b_{hBN}$ is again 50 nm (10 %) for 2 µm slit sample, 50 nm (2%) for the 5 µm slit sample, 80 nm (2.2%) µm slit sample and 200 nm (4%) for the 10 µm slit sample.

# Appendix B

# 1D diffusion model for two materials

In this Appendix all fits done with the 1D model derived by Denis Kochan (see Section 4.2.3) are shown for all four samples.

## B.1 Comparison of $\Delta T_{th}$ with the Kochan model

In Figure B.1 one can see the fits of temperature difference at the thermometer $\Delta T_{th}$ for all the four samples, for different bath temperatures. For some plots the fits look noisy. This due to the fact that using Equation 4.33 we need to use experimental values for the temperature difference at the heater $\Delta T_h$ and these data may contain noise.

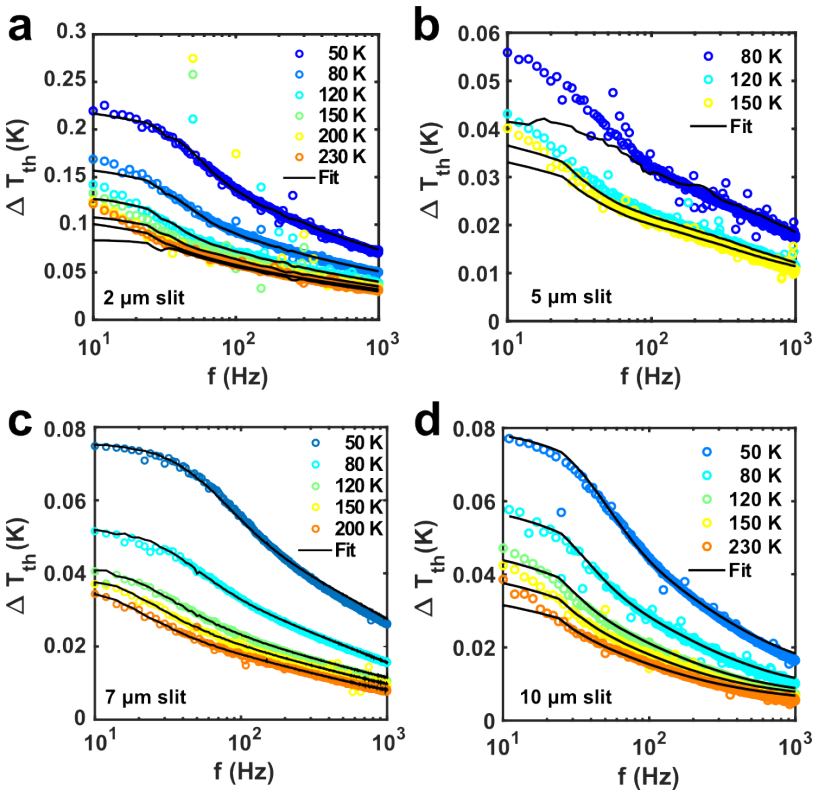


FIGURE B.1: Fits using our 1D model (see Section 4.2.3) of the temperature difference at the thermometer $\Delta T_{th}$ for different samples and bath temperatures. (a) 2 μm slit sample (b) 5 μm slit sample (c) 7 μm slit sample (d) 10 μm slit sample

## B.2 Comparison of the phase difference with the Kochan model

In Figures B.2, B.3, B.4 and B.5 one can see the fits of the phase difference between the heater and the thermometer $\Delta\phi$ for different bath temperature and different samples. All the fits are slightly offseted over the y-axis to fit the data better. The original fit will always go through zero parallel to the offset fit.

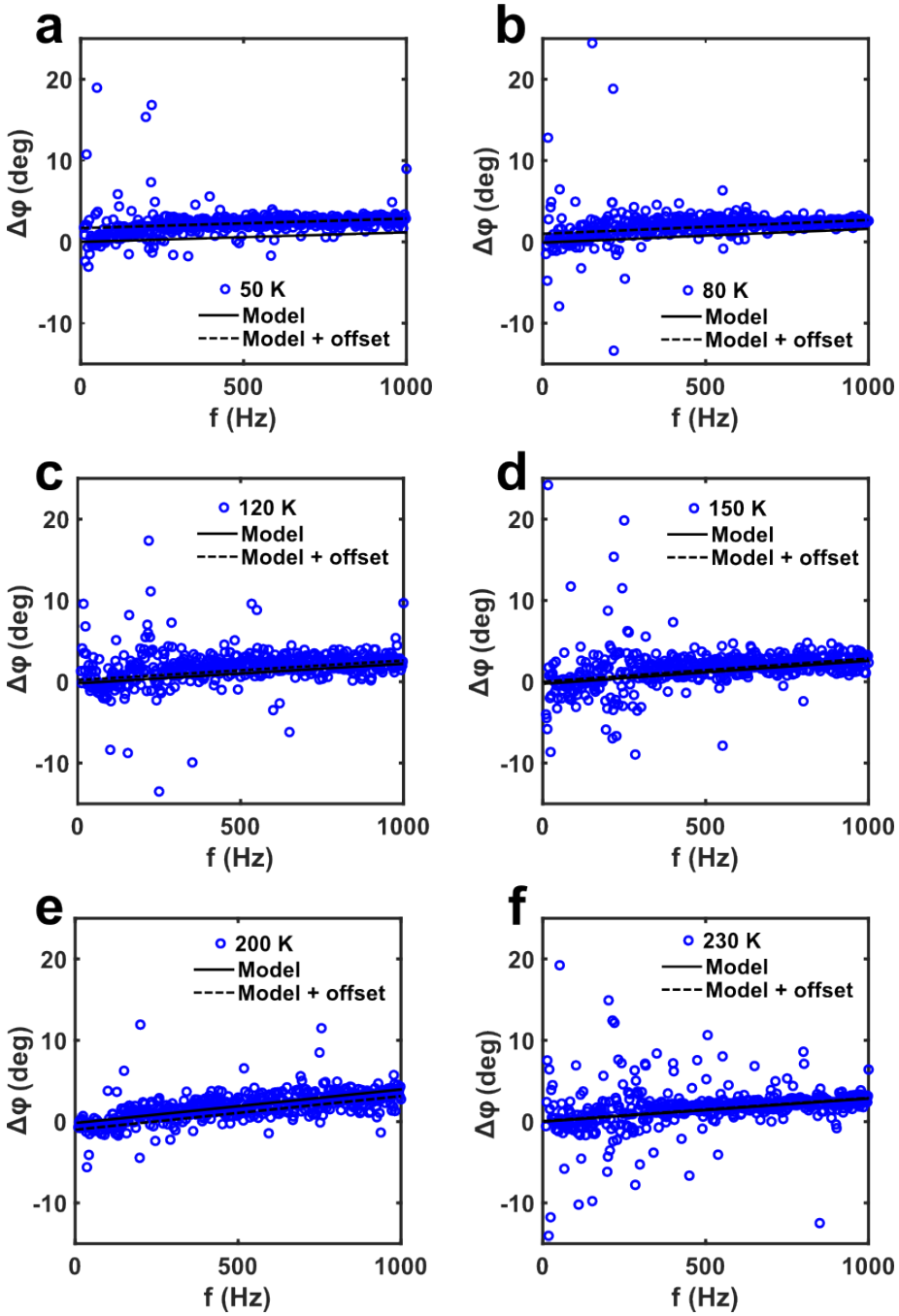


FIGURE B.2: Fits of the phase difference between the heater and thermometer $\Delta\phi$ for the 2 µm slit sample, for different bath temperatures.

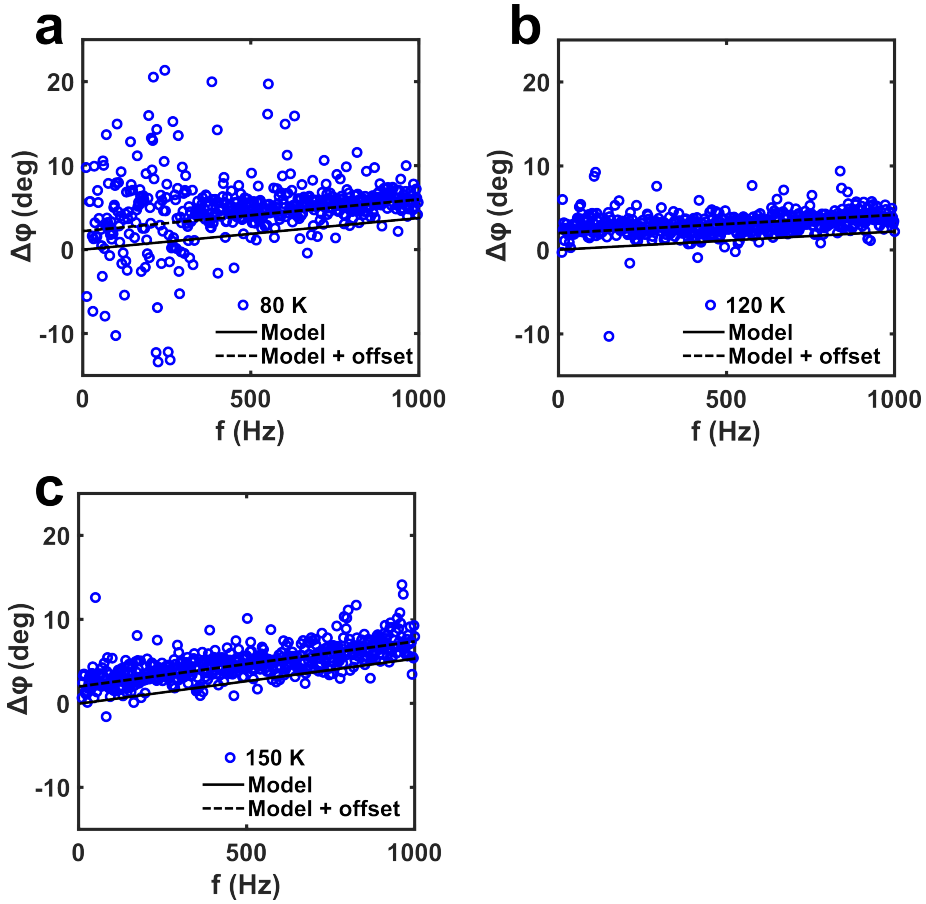


FIGURE B.3: Fits of the phase difference between the heater and thermometer $\Delta\phi$ for the 5 µm slit sample, for different bath temperatures.

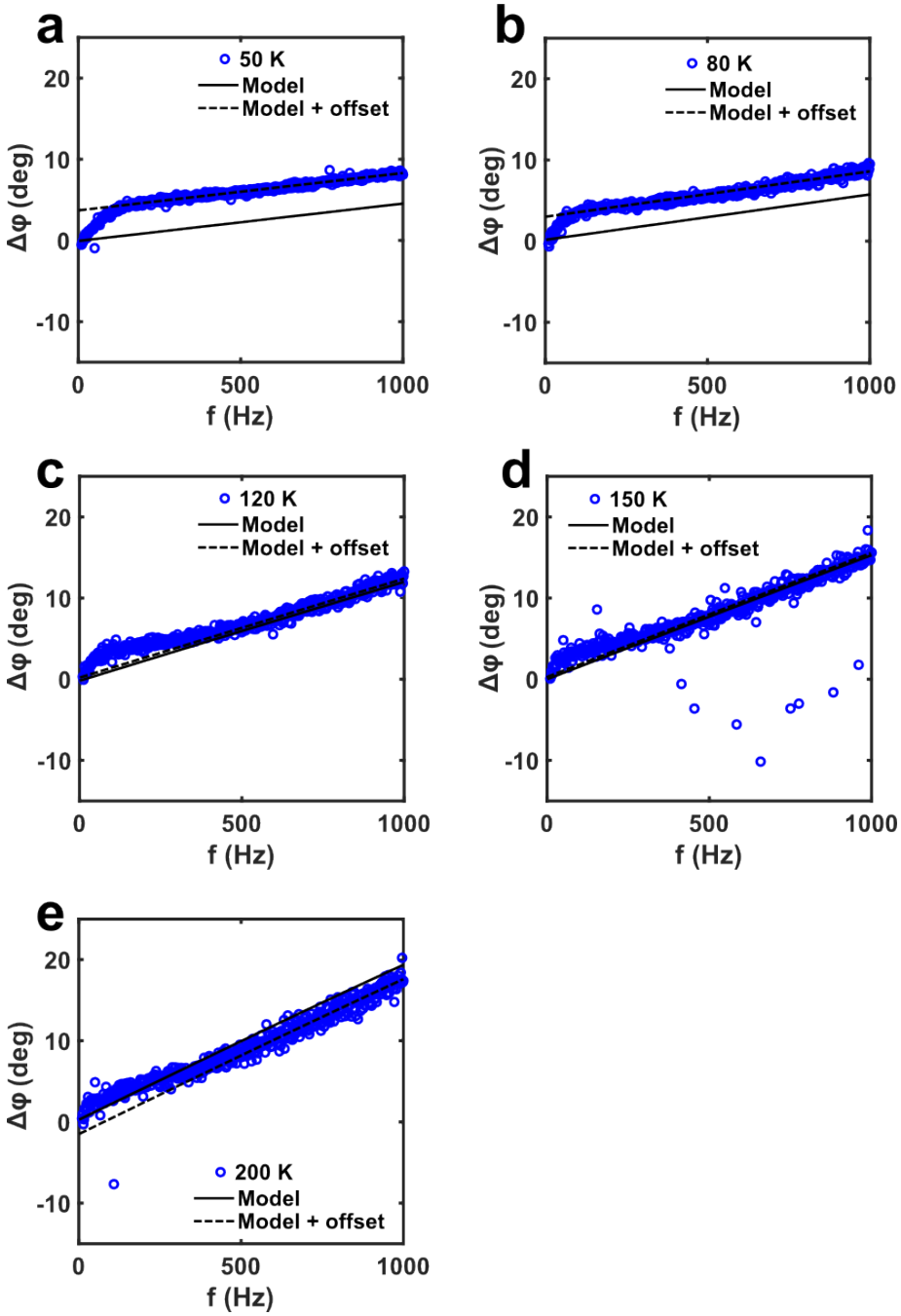


FIGURE B.4: Fits of the phase difference between the heater and thermometer $\Delta\phi$ for the 7 µm slit sample, for different bath temperatures.

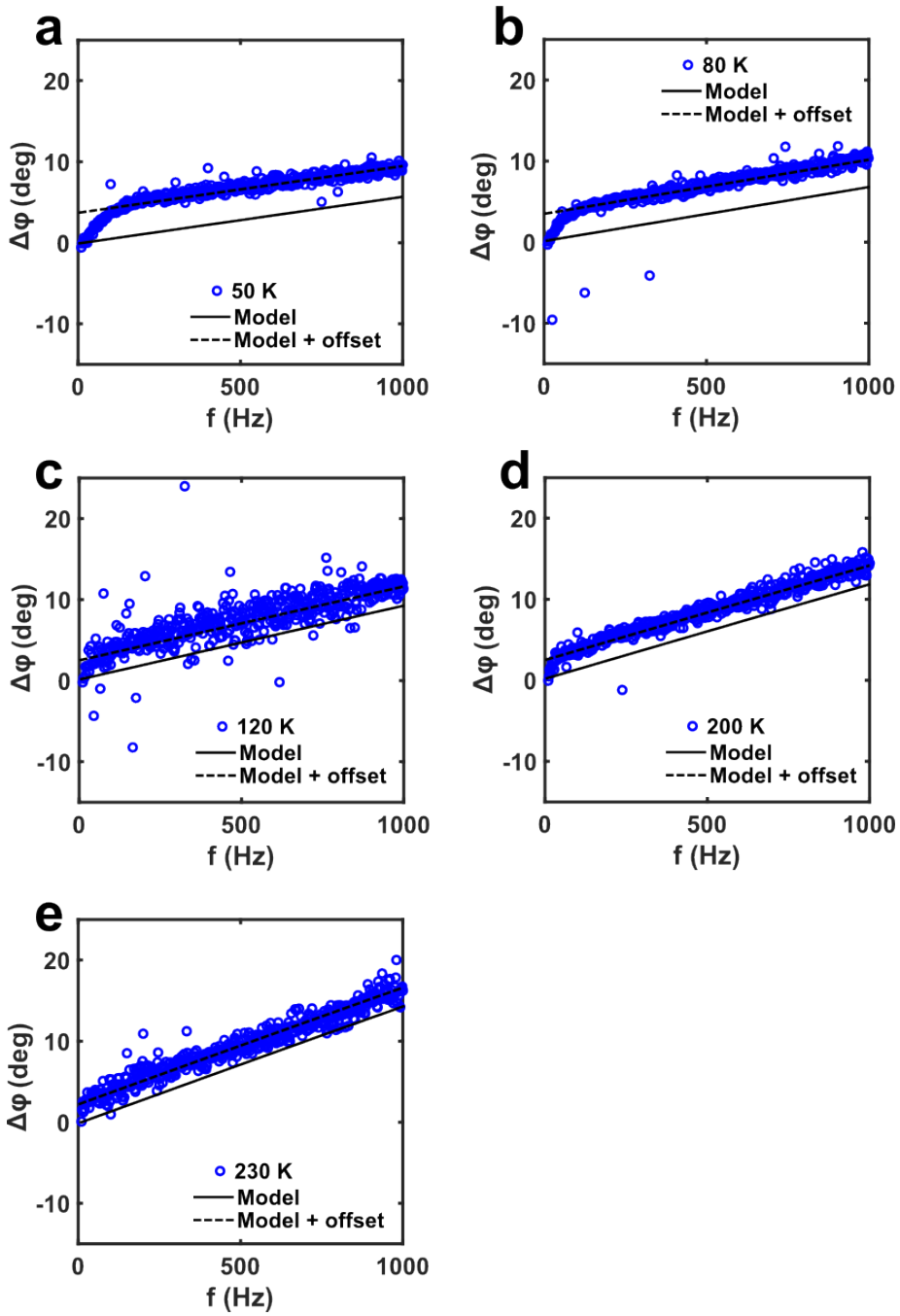


FIGURE B.5: Fits of the phase difference between the heater and thermometer $\Delta\phi$ for the 10 µm slit sample, for different bath temperatures.

# Appendix C

# Fabrication steps

In this section all the fabrication steps for Chapter 4 are described in detail, so that one could reproduce them if needed.

## C.1 Markers

The first step is to fabricate the alignment markers on our samples. As mentioned in Section 4.5.1, we order the 200 nm thick $Si_3N_4$ membranes from TedPella inc. (product number 21520). Those are low-stress membranes, 3 mm in diameter, with the 200 nm layer of $Si_3N_4$ grown on top of 200 µm thick Si frame.

### C.1.1 Cleaning

We first clean the membranes in acetone, then put it shortly in isopropanol and gently dry it with the nytrogen gun. It is possible that during the blowing the membrane will temporally bend, which is visible by the color of the reflection. Yet this dry blowing does not break them and they will immediately go back to the original state, once the pressure from the nytrogen gun is removed.

### C.1.2 Gluing to the glass plate

After the cleaning we spincoat the membranes with the PMMA. To be able to do that, we need to make sure to not to expose the membrane to the vacuum chuck. Direct one-sided vacuum would break the membrane immediately. Therefore we glue the membrane to a small, thin glass plate using the Fixogumm glue. This is done by dipping the handle of a pair of tweezers into the glue and drawing two narrow lines on the glass plate. The sample is then deposited in between those two lines and slightly pushed over the glue, by shifting it to the right and to the left. This is a delicate procedure - if too much glue is used, it can get to the bottom of the membrane, from where you could not remove it anymore. If too little glue is used, the sample will get loose during spincoating. It is recommended to use sharp carbon tweezers to deposit the sample on the glue, to gain the maximum control. After the sample is glued, one should give it a minute to dry. The tweezers handle can easily be cleaned by removing the not yet dried glue with a tissue.

### C.1.3 Spincoating

Once the sample is safely glued to the glassplate, one can deposit it on the vacuum chuck without any risk of damaging the membrane with the vacuum. We spincoat one layer of 950k 5% PMMA, using a standard 2 step procedure. The first step is 5 seconds at 3000 rpm, the second step is 30 seconds at 8000 rpm. After spincoating

we bake the sample at 150 °C, for 6 minutes, without removing the sample from the thin glass plate. It is important not to use thick glass plates during baking and make sure the original thin glass plate is laying on the hotplate directly. Otherwise the presence of two glass plates would reduce the effective baking temperature to an unacceptable level.

### C.1.4 E-beam lithography

After baking the PMMA, we proceed to E-beam lithography. We use the program Edraw to create the needed geometry to be written and Elitho to actually write it. All lithographies have been done with the laser interferometric stage. We use Zeiss SEM's. The corners of the membrane are used to align the geometry to the sample. It is not a very precise procedure, big shifts are possible from the actual center of the membrane, but the following steps (the slit and the heater) will be perfectly aligned to the markers. We write eight markers: four central small ones, that will be used for precise alignment, and four big ones, outside of the membrane, that will be later used for rough alignment. The central markers all have the same writing field of 110 µm square, with the center at (0,0). The big outside markers all have their own individual writing field with a shifted center. We write at 30 kV, with a dose of 560 $\mu C/cm^2$. The aperture is 30 µm.

### C.1.5 Development

After the E-beam lithography, we develop the sample in the mixture of Methyl isobutyl ketone (MIBK) and isopropanol (ratio of 1:3). The sample is hold in the MIBK mixture for 20 s and then for 45 s in the pure isopropanol. After development it is important to check the sample in the optical microscope to make sure all markers are present and have preserved their expected shape. On rare occasions some dirt, bubbles or scratches could be present on the sample, which would prohibit a successful deposition.

### C.1.6 Metal deposition

After development we load our samples in our Univex A deposition chamber. This system has chamber with a cap, that can be tilted. Within one hour of pumping one can reach vacuum of about 1-5e-6 mbar. We load a metal strip with gold on top and either an e-gun titanium target, or a second metal strip with titanium on top. The system allows both e-gun and thermal deposition. Both methods were used for the titanium and yield approximately the same results. We deposit 5 nm of Ti and 30 nm of Au. The usual rate for Ti is about 1-2 Å p/s. The rate for gold deposition usually started at 2 Å p/s and would rise during the deposition to 3-4 Å p/s. The currents used for thermal deposition of gold would be around 140-150 A. For thermal deposition of Ti around 190-200 A. For E-gun deposition of Ti the poti would show 1.3-1.4.

### C.1.7 Lift-off

After the deposition the samples would be put in warm acetone and left on a hotplate overnight, at 60 °C. To remove the unneeded metal leftovers, we shake the bottle till all the metal, except for the markers, comes loose. After that we take out the sample from acetone, shortly wash in isopropanol and blow dry with a nytrogen gun.

## C.2 Slit

To etch a slit in the membrane, we again undergo a similar procedure as for the markers.

### C.2.1 Spincoating

We again glue our sample to a thin glass plate, to avoid exposing it to the vacuum. For the etching step we spincoat three consequent layers of 200k 9% PMMA. Each layer is baked for 6 min at 150 °C, and then left to cool off for 1 min before the next spincoating. If this cooling is not done, the PMMA tends to form cracks around the slit after development. The three layers are necessary to form a thick enough buffer, so that during etching in the unexposed area's only the PMMA is etched, without reaching the SiN membrane.

### C.2.2 E-beam lithography and development

For lithography we again use 30 kV and a 30 µm aperture. The dose is 1000 µC/cm$^2$. We use an alignment procedure in two steps. First we use the big markers for rough adjustment of the field. Then we use the smaller, central markers for a precise alignment with windows of alignment. This way we do not expose the writing field of the slit to the beam, and expose the small markers with only a very small dose (10 µC/cm$^2$) during the alignment. This prohibits the accidental etching of the marker area on the membrane.

The development is done again in MIBK-isopropanol mixture (1:3). The sample is hold for 1 min in the mixture and 30 s in pure isopropanol.

### C.2.3 Reactive Ion Etching

Before putting sample into the Reactive Ion Etcher (RIE) chamber, we clean it in two steps. The first step uses argon (40 ccm), 40 mTorr, 150 W, for 2 min. The second step uses oxygen (100 ccm), 100 mTorr, 200 W, for 10 min. After cleaning we load the sample into the Reactive Ion Etcher (RIE). We use two gases, $CHF_3$ (50 ccm) and $O_2$ (5 ccm), 30 mTorr, 150 W, for 6 min.

### C.2.4 Cleaning

After etching we put the samples overnight in warm acetone (60 °C) to remove the PMMA. After that we wash it shortly in isopropanol and then blow dry with the nytrogen gun. Usually, even after the cleaning in acetone, there are still some PMMA residues left on the sample. We remove those residues by doing an extensive oxygen plasma cleaning (60%), for 1 min. If needed, the process can be repeated till all the residues are gone.

## C.3 h-BN and heater

After making the slit, we stamp a h-BN flake on top of that slit using deterministic dry viscoelastic stamping method [41]. This process is described in detail in Chapter 2.

### C.3.1 Annealing

After successful stamping session, we make optical pictures of the sample at different magnification and make a file for the E-beam lithography. To make sure the flake does not fly off during spincoating we anneal the sample in air, on a 300 °C hotplate for 10 min.

This type of annealing makes the surface hydrophobic, which prohibits the PMMA to stick to the sample surface during spincoating. Therefore we put the sample shortly into weak oxygen plasma (30 %) for 20 seconds. This brings the sample back to its normal state.

### C.3.2 Spincoating and E-beam lithography

For spincoating we again glue our sample to a thin glass plate, to avoid exposing it to the vacuum. For this step we spincoat one layer of 950k 5% PMMA. We bake the sample for 6 min at 150 °C.

After spincoating the sample, we use the optical pictures to load the sample with proper orientation into the SEM. Then we use the geometry file to write the contacts. We use 30 kV, 30 µm aperture. For the contacts outside the membrane we use a dose of 560 µC/cm$^2$, for small parts and contacts on the membrane we use a dose of 1200 µC/cm$^2$. We again use the double alignment procedure, with the big markers used for rough alignment, and central small markers for precise alignment. During this lithography it is of grave importance to focus as best as possible, preferably reaching decent view on 20 nm scale. Otherwise it is not possible to keep the heater 100 nm wide.

### C.3.3 Development and Metal deposition

We develop the samples again in MIBK-isopropanol mixture (1:3). We put the sample for 20 s in the mixture, and then for 45 s in the pure isopropanol.

We then load the sample into Univex. We again deposit gold and titanium as sticking layer. See Section C.1.6 for details. We deposit 10 nm of titanium and 30 nm of gold.

### C.3.4 Lift-off

We keep the sample overnight in warm acetone at 60 °C. After that we again shake the bottle to remove the unneeded metal from the surface. Then we shortly wash the sample in isopropanol and let it dry itself by its own, to minimize the stress to the suspended flake.

# Appendix D

# 3ω method - 2D model

As mentioned in Section 4.3.2 we have considered the 1D model for the 3ω method. We have also considered a 2D model as well, proposed by Jain and Goodson in 2008 [111], but could not use it for the same reason as the 1D model proposed by Sikora et al. [95] - 3ω method can not be used to measure two materials at the same time. Yet, during our consideration of the 2D model we have found a small error in the expression of the $\Delta T_h$ (see Equations D.4 and D.6) and asked Denis Kochan to derive the proper expression. This appendix explains the 2D model in detail and points out where the error was and what the corrected expression should be.

In their work Jain and Goodson derive a solution to the 2D diffusion equation:

$$\frac{\partial^2 T}{\partial x^2} + \frac{\partial^2 T}{\partial y^2} = \frac{\eta}{\lambda_{mat}} + \frac{1}{D} \cdot \frac{\partial T}{\partial t}, \tag{D.1}$$

where $T(x, y, t)$ is the temperature, $x$ and $y$ are the coordinates in the plane of the measured material (presuming a negligible thickness compared to the width and length of the film), $\lambda_{mat}$ is the thermal conductivity of the measured material and $D$ is its thermal diffusivity. $\eta$ is the power input per volume.

We assume a suspended thin film as the material we want to measure. Figure D.1 shows a schematic of such a sample, with Figure D.1a showing side view and Figure D.1b the top view of the membrane. The length of the heater and the membrane is denoted with $l_{mem}$ and the width is denoted with $b_{mem}$. We assume the x-axis along the heater.

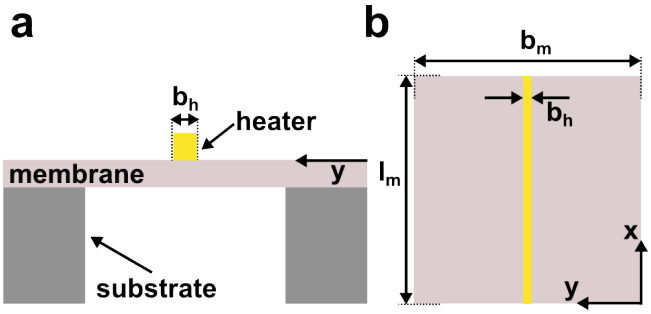


FIGURE D.1: Schematic side (a) and top view (b) of the sample. The heater line of length $l_{mem}$ and width $b_h$ crosses the suspended membrane in the middle, $b_{mem}/2$ distance away from the border of the membrane.

In order to solve Equation D.1, the membrane is separated in two halfs. Only one half is considered. One assumes that on edge of the half-membrane (along the x-axis, see Figure D.1b) the temperature $T(x, y, t)$ will be equal to the bath temperature $T_{bath}$, since there all the heat will flow into the surrounding substrate, the substrate acting as a thermal bath. Therefore, we can formulate the following boundary conditions:

$$T(0,y,t) = T(l_{mem},y,t) = T(x,0,t) = 0,$$
$$\left.\frac{\partial T}{\partial y}\right|_{y=b_{mem}/2} = \frac{I_h^2 \cdot R_h}{2 \cdot \lambda_{mem} \cdot t_{mem} \cdot l_{mem}}, \tag{D.2}$$

where $l_{mem}$ is the length of the membrane, $b_{mem}$ is the width of the membrane, $t_{mem}$ the thickness of the membrane. $T$ is the time and space dependent temperature function. $I_h$ is the current through the heater, $R_h$ is the electrical resistance of the heater. $\lambda_{mem}$ is the thermal conductivity of the membrane.

By solving Equation D.1, one obtains two different components of $T(x,y,t)$, one independent of the angular frequency $\omega$ and the second one proportional to $2\omega$, as consistent with Equation 4.17:

$$\Delta T_{av} = \sum_{n=1}^{\infty} = \frac{I_0^2 \cdot R_0}{2 \cdot \lambda_{mem} \cdot t_{mem} \cdot (n \cdot \pi)^3} \cdot [1 - \cos(n \cdot \pi)]^2 \cdot \tanh(\frac{n \cdot \pi \cdot b_{mem}}{2 \cdot l_{mem}}), \tag{D.3}$$

$$\Delta T_h = \sum_{n=1}^{\infty} \sum_{m=1}^{\infty} -\frac{\xi_{m,n}}{2 \cdot \sqrt{\gamma_{m,n}^2 + 4\omega^2}} \cdot \frac{\sin([m - 1/2] \cdot \pi) \cdot [1 - \cos(n \cdot \pi)]}{n \cdot \pi}, \tag{D.4}$$

with $\Delta T_{av}$ is the average temperature difference due to Joule heating and $\Delta T_h$ the oscillating temperature rise proportional to $2\omega$. $t_{mem}$ is the thickness of the membrane,$b_{mem}$ is the width of the membrane, $l_{mem}$ the length of the membrane. $\lambda_{mem}$ the thermal conductivity and $I_0$ and $R_0$ the amplitude of the oscillating current through the heater and the electrical resistance of the heater, respectively.

The variables $\xi_{m,n}$ and $\gamma_{m,n}$ are defined in the following way:

$$\xi_{m,n} = (-1)^{m+1} \cdot (1 - (-1)^n) \cdot \frac{8 \cdot D}{n \cdot \pi \cdot b_{mem}} \cdot \frac{I_0^2 \cdot R_0}{2 \cdot \lambda_{mem} \cdot t_{mem} \cdot l_{mem}}, \tag{D.5}$$

$$\gamma_{m,n} = D \cdot \pi^2 \cdot \left[ \left( 4 \cdot \frac{m - 1/2}{b_{mem}} \right)^2 + \left( \frac{n}{l_{mem}} \right)^2 \right], \tag{D.6}$$

with $b_{mem}$ and $l_{mem}$ being the width and the length of the membrane respectively, and $m$ and $n$ being the simultaniously running indexes of the two infinite sums.

Note, that according to our calculations, the original paper [111] contains a small error in the Equations D.4 and D.6. The part $m - 1/2$ is both times written as $m + 1/2$ which would give a wrong outcome. In the equations above the formula's are represented with our corrections applied.

One can use the solutions provided by Equations D.3 and D.4 to obtain an expression for the voltage measured across the heater:

$$V_\omega = I_0 \cdot R_0 + I_0 \cdot \frac{dR_h}{dT_h} \cdot \Delta T_{av}, \tag{D.7}$$

$$V_{3\omega} = 2 \cdot I_0 \cdot \frac{dR_h}{dT_h} \cdot \Delta T_h. \tag{D.8}$$

Since the solution contains two infinite sums, an analytical solution is not possible, but we have found that a numerical approximation with $n, m = 10,000$ already reaches convergence and shows no difference with higher limits of $n$ and $m$.

# Appendix E

# Effusion model for the thermal contact resistance

We use the effusion model to approximate our thermal resistance values: we take as a basis a box with phonons, where they can escape through an orifice. Only in our case we do not have an orifice, but a reflective wall in the box. The phonons inside the box represent the phonons in the heater, the reflective wall represents the layer of adsorbates between the heater and the h-BN flake and the escaped phonons are the phonons that went through the barrier into the flake.

We take the expression for thermal current $I_{th}$ from the work by Bartsch et al. [146] and modify it to obtain the needed thermal resistance $R_c$ expression.

In the original work Bartsch et al. study ballistic thermal point contacts, where the phonon mean free path is bigger than the sample size. Yet, the approach they use is relatively universal and can be applied to our samples, if we modify the dispersion relation.

We start with the original expression for the thermal current $I_{th}$ [146]:

$$I_{th} = A \sum_{p=1}^{3} \int_0^{k_{max}} \frac{1}{(2\pi)^3} \cdot [f(k, T_{hot}) - f(k, T_{cold})] \cdot \hbar\omega_p(k) \cdot v_p(k) \cos(\theta) \cdot d^3k, \quad \text{(E.1)}$$

with $A$ the cross-section, in the case of Bartsch et al. it is the cross-section of the point contact and in our case it is the cross-section of the interface between the heater and the flake. $k$ is the wave number, $f(k, T)$ is the Bose-Einstein distribution, $T_{hot}$ is the the temperature on the hot end, $T_{cold}$ is the the temperature on the cold end, $\hbar\omega_p(k)$ is the phonon energy and $v_p(k)$ is the group velocity of the phonons. The sum sign indicates the summation over three phonon modes: one longitudinal and two transversal acoustic modes. The $\cos(\theta)$ is a factor relevant in case we presume that only part of the incoming phonons will get through the interface, depending on the incoming angle. For example, if the interface is a circular hole in a box, like in the case of Bartsch et al. [146]. In our case we can neglect this factor, since our heater is the same size as the interface below it.

If we make a Taylor expansion of the Bose-Einstein distribution, we can write the following for $\Delta T = T_{hot} - T_{cold} << T_{hot}$:

$$\frac{[f(k, T_{hot}) - f(k, T_{cold})]}{\Delta T} = \frac{df}{dT} = \frac{1}{T} \cdot \frac{\epsilon}{k_B T} \cdot \frac{e^{\epsilon/k_B T}}{(e^{\epsilon/k_B T} - 1)^2}, \quad \text{(E.2)}$$

with $f(k, T)$ the Bose-Einstein distribution, $\Delta T$ the difference in temperature between the hot and cold end, $k_B$ the Boltzmann constant, $T$ the temperature and $\epsilon = \hbar\omega_p$ the phonon energy.

We can also express the group velocity $v_p(k)$ and the integral differential $d^3k$ in the following way [147]:

$$v_p(k) = \frac{\partial \omega_p}{\partial k} = \frac{1}{\hbar} \cdot \frac{\partial \epsilon}{\partial k}, \tag{E.3}$$

and

$$d^3k = 4\pi k^2 dk. \tag{E.4}$$

If we assume that all the phonon modes contribute equally, the sum will result in a factor 3. Then we can rewrite Equation E.1 as:

$$\begin{aligned} K_{th} &= \frac{I_{th}}{\Delta T} \\ &= \frac{3A\Delta T}{\hbar T} \int_0^{k_{max}} \frac{\epsilon}{(2\pi)^3} \cdot \frac{e^{\epsilon/k_B T}}{(e^{\epsilon/k_B T} - 1)^2} \cdot \left[\frac{\epsilon}{k_B T}\right] \cdot \frac{\partial \epsilon}{\partial k} \cdot 4\pi k^2 dk \\ &= \frac{3A\Delta T}{2\pi^2 \hbar T} \int_0^{\epsilon_{max}} k^2 \cdot \frac{e^{\epsilon/k_B T}}{(e^{\epsilon/k_B T} - 1)^2} \cdot \left[\frac{\epsilon^2}{k_B T}\right] \cdot d\epsilon, \end{aligned} \tag{E.5}$$

with $A$ the cross-section, $T$ the temperature, $\Delta T$ the temperature difference between hot and cold, $\epsilon$ the phonon energy, $k_B$ the Boltzmann constant, $\hbar$ the reduced Planck constant and $k$ the wave number.

We can write the wave number $k$ in the following way [147]:

$$k = \frac{\omega_p}{u} = \frac{\epsilon}{\hbar u}, \tag{E.6}$$

with $u$ the phonon sound velocity, $\hbar$ the reduced Planck constant and $\epsilon$ the phonon energy.

If we then introduce a variable $x = \epsilon / k_B T$, we can write:

$$K_{th} = \frac{3A}{2\pi^2 u^2} \cdot k_B \cdot \left[\frac{k_B T}{\hbar}\right]^3 \cdot \int_0^{x_{max}} \frac{x^4 e^x}{(e^x - 1)^2} \cdot dx, \tag{E.7}$$

with $K_{th}$ the thermal conductance, $A$ the cross-section, $u$ the phonon speed of sound, $\hbar$ the reduced Planck constant, $k_B$ the Boltzmann constant and $x_{max} = (\hbar\omega_D)/(k_B T) = T_D/T$, with $\omega_D$ the Debye frequency and $T_D$ the Debye temperature.

Now if use the definition of the Debye temperature $T_D$ [130], we can write:

$$\left[\frac{T}{T_D}\right]^3 = \left[\frac{k_B T}{\hbar}\right]^3 \cdot \frac{V}{N} \cdot \frac{1}{6\pi^2 u^3}, \tag{E.8}$$

with $T_D$ the Debye temperature, $k_B$ the Boltzmann constant, $\hbar$ the reduced Planck's constant, $u$ the phonon speed of sound, $V$ the volume and $N$ the amount of atoms.

Within the Debye model, the specific heat (per volume) is written as:

$$c_V(T) = 9k_B \left[\frac{N}{V}\right] \left[\frac{T}{T_D}\right]^3 \int_0^{T_D/T} \frac{x^4 e^x}{(e^x - 1)^2} dx, \tag{E.9}$$

therefore we can now re-write Equation E.7 as:

$$K_{th} = A \cdot u \cdot c_V(T) \tag{E.10}$$

Now Equation E.10 assumes a total transparency of the interface, which is not the case for our samples. Therefore we introduce a transparency coefficient $\mathcal{T}$ (between 0 and 1):

$$R_c = (A \cdot \mathcal{T} \cdot u \cdot c_V(T))^{-1} \tag{E.11}$$

# Bibliography

[1] Moore, G. E.

Cramming more components onto integrated circuits.

*Electronics* 38.114 (1965)

[2] Moore, G.E.,

Progress in digital integrated electronics.

*In Electron devices meeting* 21 (1975), 11-13.

[3] Thompson, S. E., and Parthasarathy, S.

Moore's law: the future of Si microelectronics.

*Materials Today* 9.6 (2006), 20-25.

[4] Novoselov, K. S., Geim, A. K., Morozov, S. V., Jiang, D., Zhang, Y., Dubonos, S. V., Grigorieva, I. V., and Firsov, A. A.

Electric field effect in atomically thin carbon films. *Science* 306.5696 (2004), 666-669.

[5] Novoselov, K. S., Geim, A. K., Morozov, S. V., Jiang, D., Katsnelson, M. I., Grigorieva, I. V., Dubonos, S. V., and Firsov, A. A.

Two-dimensional gas of massless Dirac fermions in graphene. *Nature* 438.7065 (2005), 197-200

[6] Buscema, M., Island, J. O., Groenendijk, D. J., Blanter S. I., Steele G. A., van der Zant, H. S., Castellanos-Gomez, A.

Photocurrent generation with two-dimensional van der Waals semiconductors.

*Chemical Society Reviews* 44.11 (2015), 3691-3718.

[7] Wang L, Meric I, Huang PY, Gao Q, Gao Y, Tran H, Taniguchi T, Watanabe K, Campos LM, Muller DA, Guo J.

One-dimensional electrical contact to a two-dimensional material.

*Science* 342.6158 (2013), 614-617.

[8] Ovchinnikov D, Allain A, Huang YS, Dumcenco D, Kis A.

Electrical transport properties of single-layer WS2.

*ACS nano* 8.8 (2014), 8174-8181.

[9] Baugher BW, Churchill HO, Yang Y, Jarillo-Herrero P.

Intrinsic electronic transport properties of high-quality monolayer and bilayer MoS2.

*Nano letters* 13.9 (2013), 4212-4216.

[10] Radisavljevic B, Kis A.

Mobility engineering and a metal–insulator transition in monolayer MoS 2.

*Nature materials* 12.9 (2013), 815.

[11] Neto AC, Guinea F, Peres NM, Novoselov KS, Geim AK.

The electronic properties of graphene.

*Reviews of modern physics* 81.1 (2009), 109.

[12] Cao Y, Fatemi V, Fang S, Watanabe K, Taniguchi T, Kaxiras E, Jarillo-Herrero P.

Unconventional superconductivity in magic-angle graphene superlattices.

*Nature* 556.7699 (2018), 43.

[13] Yin Z, Li H, Li H, Jiang L, Shi Y, Sun Y, Lu G, Zhang Q, Chen X, Zhang H.

Single-layer MoS2 phototransistors.

*ACS nano* 6.1 (2011), 74-80.

[14] Buscema M, Groenendijk DJ, Blanter SI, Steele GA, Van Der Zant HS, Castellanos-Gomez A.

Fast and broadband photoresponse of few-layer black phosphorus field-effect transistors.

*Nano letters* 14.6 (2014), 3347-3352.

[15] Splendiani A, Sun L, Zhang Y, Li T, Kim J, Chim CY, Galli G, Wang F.

Emerging photoluminescence in monolayer MoS2.

*Nano letters* 10.4 (2010), 1271-1275.

[16] Rivera P, Seyler KL, Yu H, Schaibley JR, Yan J, Mandrus DG, Yao W, Xu X.

Valley-polarized exciton dynamics in a 2D semiconductor heterostructure.

*Science* 351.6274 (2016), 688-691.

[17] Shi H, Yan R, Bertolazzi S, Brivio J, Gao B, Kis A, Jena D, Xing HG, Huang L.

Exciton dynamics in suspended monolayer and few-layer MoS2 2D crystals.

*ACS nano* 7.2 (2013), 1072-1080.

[18] Ciarrocchi A, Unuchek D, Avsar A, Watanabe K, Taniguchi T, Kis A.

Polarization switching and electrical control of interlayer excitons in two-dimensional van der Waals heterostructures.

*Nature photonics* 13.2 (2019), 131-136.

[19] Chen C, Chen F, Chen X, Deng B, Eng B, Jung D, Guo Q, Yuan S, Watanabe K, Taniguchi T, Lee ML.

Bright Mid-Infrared Photoluminescence from Thin-Film Black Phosphorus.

*Nano letters* 19.3 (2019), 1488-1493.

[20] Ferrari AC, Meyer JC, Scardaci V, Casiraghi C, Lazzeri M, Mauri F, Piscanec S, Jiang D, Novoselov KS, Roth S, Geim AK.

Raman spectrum of graphene and graphene layers.

*Physical review letters* 97.18 (2006), 187401.

[21] Tanaka, H., Kawazoe, T. and Ohtsu, M.,

Increasing Si photodetector photosensitivity in near-infrared region and manifestation of optical amplification by dressed photons.

*Applied Physics B* 108.1 (2012), pp.51-56.

[22] Carey, J.E., Crouch, C.H., Shen, M. and Mazur, E.,

Visible and near-infrared responsivity of femtosecond-laser microstructured silicon photodiodes.

*Optics letters* 30.14 (2005), pp.1773-1775.

[23] Feng, W., Wu, J. B., Li, X., Zheng, W., Zhou, X., Xiao, K., Cao, W., Yang, B., Idrobo, J. C., Basile, L., Tian, W.

Ultrahigh photo-responsivity and detectivity in multilayer InSe nanosheets phototransistors with broadband response.

*Journal of Materials Chemistry C* 3.27 (2015), 7022-7028.

[24] Ko, P. J., Abderrahmane, A., Takamura, T., Kim, N. H., Sandhu, A.

Thickness dependence on the optoelectronic properties of multilayered GaSe based photodetector.

*Nanotechnology* 27.32 (2016), 325202.

[25] Yao, J., Deng, Z., Zheng, Z., Yang, G.

Stable, fast UV–Vis–NIR photodetector with excellent responsivity, detectivity, and sensitivity based on $\alpha$-In2Te3 films with a direct bandgap.

*ACS applied materials and interfaces* 8.32 (2016), 20872-20879.

[26] Yin, L., Xu, K., Wen, Y., Wang, Z., Huang, Y., Wang, F., Shifa, T.A., Cheng, R., Ma, H., He, J.

Ultrafast and ultrasensitive phototransistors based on few-layered HfSe2.

*Applied Physics Letters* 109.21 (2016), 213105.

[27] Candini, A., Martini, L., Chen, Z., Mishra, N., Convertino, D., Coletti, C., Narita, A., Feng, X., Mullen, K., Affronte, M.

High photoresponsivity in graphene nanoribbon field-effect transistor devices contacted with graphene electrodes.

*The Journal of Physical Chemistry C* 121.19 (2017), 10620-10625.

[28] Liu, E., Long, M., Zeng, J., Luo, W., Wang, Y., Pan, Y., Zhou, W., Wang, B., Hu, W., Ni, Z., You, Y., 2016.

High responsivity phototransistors based on few-layer ReS2 for weak signal detection.

*Advanced Functional Materials* 26.12 (2016), 1938-1944.

[29] Lee, H., Ahn, J., Im, S., Kim, J., Choi, W.

High-Responsivity Multilayer MoSe 2 Phototransistors with Fast Response Time.

*Scientific reports* 8.1 (2018), 11545.

[30] Huang, M., Wang, M., Chen, C., Ma, Z., Li, X., Han, J., Wu, Y.

Broadband Black-Phosphorus Photodetectors with High Responsivity.

*Advanced Materials* 28.18 (2016), 3481-3485.

[31] Kwon, J., Hong, Y.K., Han, G., Omkaram, I., Choi, W., Kim, S., Yoon, Y.

Giant Photoamplification in Indirect-Bandgap Multilayer MoS2 Phototransistors with Local Bottom-Gate Structures.

*Advanced Materials* 27.13 (2015), 2224-2230.

[32] Jo I, Pettes MT, Kim J, Watanabe K, Taniguchi T, Yao Z, Shi L.

Thermal conductivity and phonon transport in suspended few-layer hexagonal boron nitride.

*Nano letters* 13.2 (2013), 550-554.

[33] Balandin AA, Ghosh S, Bao W, Calizo I, Teweldebrhan D, Miao F, Lau CN.

Superior thermal conductivity of single-layer graphene.

*Nano letters*, 8.3 (2008), 902-907.

[34] Sahoo S, Gaur AP, Ahmadi M, Guinel MJ, Katiyar RS.

Temperature-dependent Raman studies and thermal conductivity of few-layer MoS2.

*The Journal of Physical Chemistry C* 117.17 (2013), 9042-9047.

[35] Zhang X, Sun D, Li Y, Lee GH, Cui X, Chenet D, You Y, Heinz TF, Hone JC.

Measurement of lateral and interfacial thermal conductivity of single-and bilayer MoS2 and MoSe2 using refined optothermal Raman technique.

*ACS applied materials and interfaces* 7.46 (2015), 25923-25929.

[36] Smith B, Vermeersch B, Carrete J, Ou E, Kim J, Mingo N, Akinwande D, Shi L.

Temperature and Thickness Dependences of the Anisotropic In-Plane Thermal Conductivity of Black Phosphorus.

*Advanced Materials* 29.5 (2017), 1603756.

[37] Xu X, Chen J, Li B.

Phonon thermal conduction in novel 2D materials.

*Journal of Physics: Condensed Matter*, 28.48 (2016), 483001.

[38] Kim P, Shi L, Majumdar A, McEuen PL.

Thermal transport measurements of individual multiwalled nanotubes.

*Physical review letters* 87.21 (2001), 215502.

[39] Balandin AA.

Thermal properties of graphene and nanostructured carbon materials.

*Nature materials* 10.8 (2011), 569.

[40] Lee JU, Yoon D, Kim H, Lee SW, Cheong H.

Thermal conductivity of suspended pristine graphene measured by Raman spectroscopy.

*Physical Review B* 83.8 (2011), 081419.

[41] Castellanos-Gomez, A., Buscema, M., Molenaar, R., Singh, V., Janssen, L., van der Zant, H. S., Steele, G. A.

Deterministic transfer of two-dimensional materials by all-dry viscoelastic stamping.

*2D materials* 1.1 (2014), 011002.

[42] Xia, F., Mueller, T., Golizadeh-Mojarad, R., Freitag, M., Lin, Y-m., Tsang, J., Perebeinos, V., Avouris, P.

Photocurrent Imaging and Efficient Photon Detection in a Graphene Transistor

*Nano Letters* 9.3 (2009), 1039-1044.

[43] Xia, F., Mueller T., Lin, Y-m., Valdes-Garcia, A., Avouris, P.

Ultrafast graphene photodetector.

*Nature Nanotechnology* 4.12 (2009), 839-843.

[44] Yin, Z., Li, H., Jiang, L., Shi, Y., Sun, Y., Lu, G., Zhang, Q., Chen, X., Zhang, H.

Single-layer MoS2 phototransistors.

*ACS Nano* 6.1 (2012), 74-80.

[45] Alkis, S., Oztas, T., Aygun, L., Bozkurt, F., Okyay, A., Ortac, B.

Thin film MoS2 nanocrystal based ultraviolet photodetector.

*Optics Express* 20.19 (2012), 21815-21820.

[46] Yin, Z., Li, H., Jiang, L., Shi, Y., Sun, Y., Lu, G., Zhang, Q., Chen, X., Zhang, H.

Single-layer MoS2 phototransistors.

*ACS Nano* 6.1 (2012), 74-80.

[47] Lopez-Sanchez, O., Lembke, D., Kayci, M., Radenovic, A., Kis, A.

Ultrasensitive photodetectors based on monolayer MoS2.

*Nature Nanotechnology* 8.7 (2013), 497-501.

[48] Buscema, M., Barkelid, M., Zwiller, V., van der Zant, H. S., Steele, G. A., Castellanos-Gomez, A.

Large and Tunable Photothermoelectric Effect in Single-Layer MoS2.

*Nano Letters* 13.2 (2013), 358-363.

[49] Wu, C.-C., Jariwala, D., Sangwan, V. K., Marks, T. J., Hersam, M. C., Lauhon, L. J.

Elucidating the Photoresponse of Ultrathin MoS2 Field-Effect Transistors by Scanning Photocurrent Microscopy.

*The Journal of Physical Chemistry Letters* 4.15 (2013), 2508-2513.

[50] Furchi, M. M., Polyushkin, D. K., Pospishil, A., Mueller, T.

Mechanisms of Photoconductivity in Atomically Thin MoS2.

*Nano Letters* 14.11 (2014), 6165-6170.

[51] Mak, K.F., Lee, C., Hone, J., Shan, J., Heinz, T.F.

Atomically thin MoS 2: a new direct-gap semiconductor. *Physical review letters* 105.13 (2010), 136805

[52] Mak, K.F., He, K., Shan, J., Heinz, T.F.,

Control of valley polarization in monolayer MoS 2 by optical helicity. *Nature nanotechnology* 7.8 (2012), 494

[53] Mak, K.F., He, K., Lee, C., Lee, G.H., Hone, J., Heinz, T.F., Shan, J.

Tightly bound trions in monolayer MoS 2. *Nature materials* 12.3 (2013), 207

[54] Ayari, A., Cobas, E., Ogundadegbe, O., Fuhrer, M.S.

Realization and electrical characterization of ultrathin crystals of layered transition-metal dichalcogenides. *Journal of Applied Physics* 101.1 (2007), 014507

[55] Radisavljevic, B., Radenovic, A., Brivio, J., Giacometti, V., and Kis, A.

Single-layer MoS2 transistors.

*Nature nanotechnology* 6.3 (2011), 147-150.

[56] Splendiani, A., Sun, L., Zhang, Y., Li, T., Kim, J., Chim, C.Y., Galli, G., Wang, F.

Emerging photoluminescence in monolayer MoS2. *Nano letters*, 10.4 (2010), 1271-1275

[57] Eda, G., Yamaguchi, H., Voiry, D., Fujita, T., Chen, M., Chhowalla, M.

Photoluminescence from chemically exfoliated MoS2. *Nano letters* 11.12 (2011), 5111-5116

[58] Marcio Fontana, T. D., Boyd, A. K., Rinzan, M., Liu, A. Y., Paranjape, M., Barbara, P.

Electron-hole transport and photovoltaic effect in gated MoS2 Schottky junctions.

*Scientific reports* 3 (2013), 1634.

[59] Choi, W., Cho, M. Y., Konar, A., Lee, J. H., Cha, G. B., Hong, S. C., Kim, S., Kim, J., Jena, D., Joo, J., Kim, S.

High-detectivity multilayer MoS2 phototransistors with spectral response from ultraviolet to infrared.

*Advanced Materials* 24.43 (2012), 5832-5836.

[60] Wang, Q. H., Kalantar-Zadeh, K., Kis, A., Coleman, J. N., Strano, M. S.

Electronics and optoelectronics of two-dimensional transition metal dichalcogenides.

*Nature Nanotechnology* 7.11 (2012), 699-712.

[61] Mukherjee, B., Cai, Y., Tan, H. R., Feng, Y. P., Tok, E. S., Sow, C. H.

NIR Schottky photodetectors based on individual single-crystalline GeSe nanosheet.

*ACS Applied Material Interfaces* 5.19 (2013), 9594-9604.

[62] Island, J. O., Buscema, M., Barawi, M., Clamagirand, J. M., Ares, J. R., Sanchez, C., Ferrer, I. J., Steele, G. A., van der Zant, H. S., Castellanos-Gomez A.

Ultrahigh Photoresponse of Few-Layer TiS3 Nanoribbon Transistors.

*Advanced Optical Materials* 2.7 (2014), 641-645.

[63] Marsillac, S., Combot-Marie, A., Bernede, J., Conan, A.

Experimental evidence of the low-temperature formation of $\gamma$-In2Se3 thin films obtained by a solid-state reaction.

*Thin Solid Films* 288.1 (1996), 14-20.

[64] Yu, X., Hou, T., Sun, X., Li, Y.

Atomistic structures and phase transition of In2Se3 nanowires studied by DFT calculations and synchrotron radiation X-ray diffraction.

*Solid State Communications* 162 (2013), 28-33.

[65] Ho, C.-H., Lin, C.-H., Wang, Y.-P., Chen, Y.-C., Chen, S.-H., Huang, Y.-S.

Surface Oxide Effect on Optical Sensing and Photoelectric Conversion of $\alpha$-In2Se3 Hexagonal Microplates.

*ACS Applied Materials and Interfaces* 5.6 (2013), 2269-2277.

[66] Julien, C., Hatzikraniotis, E., Kambas, K.

Electrical transport properties of impurity-doped In2Se3.

*Physica status solidi (a)* 97.2 (1986), 579-585.

[67] Lewandowska, R., Bacewicz, R., Filipowicz, J., Paszkowicz, W.

Raman scattering in $\alpha$-In2Se3 crystals.

*Materials Research Bulletin* 36.15 (2001), 2577-2583.

[68] Kim, W., Javey, A., Vermesh, O, Wang, Q., Li, Y., Dai, H.

Hysteresis caused by water molecules in carbon nanotube field-effect transistors.

*Nano Letters* 3.2 (2003), 193-198.

[69] Late, D. J., Liu, B., Matte, H. R., Dravid, V. P., Rao, C.

Hysteresis in Single-Layer MoS2 Field Effect Transistors.

*ACS Nano* 6.6 (2012), 5635-5641.

[70] Luan, S., Neudeck, G. W.

An experimental study of the source/drain parasitic resistance effects in amorphous silicon thin film transistors.

*Journal of Applied Physics* 72.2 (1992), 766-772.

[71] Weis, M., Lin, J., Taguchi, D., Manaka, T., Iwamoto, M.

Insight into the contact resistance problem by direct probing of the potential drop in organic field-effect transistors.

*Applied Physical Letters* 97.26 (2010), 263304.

[72] Cui, J., Wang, L., Du, Z., Ying, P., Deng, Y.

High thermoelectric performance of a defect in $\alpha$-In2Se3-based solid solution upon substitution of Zn for In.

*Journal of Materials Chemistry C* 3.35 (2015), 9069-9075.

[73] Sze, S. M., Ng, K. K.

Physics of Semiconductor Devices.

*John Wiley and Sons*: Hoboken, NJ, 2006.

[74] Kang, H.-S., Choi, C.-S., Choi, W.-Y., Kim, D.-H., Seo K.-S.

Characterization of phototransistor internal gain in metamorphic high-electron-mobility transistors.

*Applied Physical Letters* 84.19 (2004), 3780-3782.

[75] Takanashi, Y., Takahata, K., Muramoto, Y.

Characteristics of InAlAs/InGaAs high-electron-mobility transistors under illumination with modulated light.

*IEEE Transactions on electron devices* 46.12 (1996), 2271-2277.

[76] Zhang, W., Huang, J. K., Chen, C. H., Chang Y. H., Cheng, Y. J., Li, L. J.

High-Gain Phototransistors Based on a CVD MoS2 Monolayer.

*Advanced Materials* 25.25 (2013), 3456-3461.

[77] Soci, C., Zhang, A., Xiang, B., Dayeh, S. A., Aplin, D., Park, J., Bao, X., Lo, Y.-H., Wang, D.

ZnO Nanowire UV Photodetectors with High Internal Gain.

*Nano Letters* 7.4 (2007), 1003-1009.

[78] Gonzalez-Posada, F., Songmuang, R., Den Hertog, M., Monroy, E.

Room-temperature photodetection dynamics of single GaN nanowires.

*Nano Letters* 12.1 (2012), 172-176.

[79] Konstantos, G., Clifford, J., Levina, L., Sargent, E. H.

Sensitive solution-processed visible-wavelength photodetectors.

*Nature photonics* 1.9 (2007), 531-534.

[80] Zhang, E., Jin, Y., Yuan, X., Wang, W., Zhang, C., Tang, L., Liu, S., Zhou, P., Hu, W., Xiu, F.

ReS2-Based Field-Effect Transistors and Photodetectors.

*Advanced Functional Materials* 25 (2015), 4076.

[81] Island, J.O., Blanter, S.I., Buscema, M., van der Zant, H.S., Castellanos-Gomez, A.

Gate controlled photocurrent generation mechanisms in high-gain In2Se3 phototransistors.

*Nano letters* 15.12 (2015), 7853-7858.

[82] Kulig M, Zipfel J, Nagler P, Blanter S, Schüller C, Korn T, Paradiso N, Glazov MM, Chernikov A.

Exciton diffusion and halo effects in monolayer semiconductors.

*Physical review letters* 120.20 (2018), 207401.

[83] Fugallo G, Cepellotti A, Paulatto L, Lazzeri M, Marzari N, Mauri F.

Thermal conductivity of graphene and graphite: collective excitations and mean free paths.

*Nano letters* 14.11 (2014), 6109-6114.

[84] Huberman S, Duncan RA, Chen K, Song B, Chiloyan V, Ding Z, Maznev AA, Chen G, Nelson KA.

Observation of second sound in graphite at temperatures above 100 K.

*Science*, 364.6438 (2019), 375-379.

[85] Ghosh S, Bao W, Nika DL, Subrina S, Pokatilov EP, Lau CN, Balandin AA.

Dimensional crossover of thermal transport in few-layer graphene.

*Nature materials*, 9.7 (2010), 555.

[86] Scuracchio P, Michel KH, Peeters FM.

Phonon hydrodynamics, thermal conductivity, and second sound in two-dimensional crystals.

*Physical Review B* 99.14 (2019), 144303.

[87] Cepellotti A, Fugallo G, Paulatto L, Lazzeri M, Mauri F, Marzari N.

Phonon hydrodynamics in two-dimensional materials.

*Nature communications* 6.6 (2015), 6400.

[88] Simpson A, Stuckes AD.

The thermal conductivity of highly oriented pyrolytic boron nitride.

*Journal of Physics C: Solid state physics* 4.13 (1971), 1710.

[89] Ouyang T, Chen Y, Xie Y, Yang K, Bao Z, Zhong J.

Thermal transport in hexagonal boron nitride nanoribbons.

*Nanotechnology* 21.24 (2010), 245701.

[90] Tabarraei A.

Thermal conductivity of monolayer hexagonal boron nitride nanoribbons.

*Computational Materials Science* 108 (2015), 66-71.

[91] Mahdizadeh SJ, Goharshadi EK, Akhlamadi G.

Thermo-mechanical properties of boron nitride nanoribbons: A molecular dynamics simulation study.

*Journal of Molecular Graphics and Modelling* 68 (2016), 1-3.

[92] Malekpour H, Balandin AA.

Raman-based technique for measuring thermal conductivity of graphene and related materials.

*Journal of Raman Spectroscopy*, 49.1 (2018), 106-120.

[93] Cahill DG.

Thermal conductivity measurement from 30 to 750 K: the $3\omega$ method.

*Review of scientific instruments* 61.2 (1990), 802-8.

[94] Lee SM, Cahill DG.

Heat transport in thin dielectric films.

*Journal of applied physics* 81.6 (1997), 2590-2595.

[95] Sikora A, Ftouni H, Richard J, Hébert C, Eon D, Omnes F, Bourgeois O.

Highly sensitive thermal conductivity measurements of suspended membranes (SiN and diamond) using a $3\omega$-Völklein method.

*Review of Scientific Instruments* 83.5 (2012), 054902.

[96] Fourier, J. B. J.

Theorie analytique de la chaleur. (Analytical theory of heat)

*Chez Firmin Didot, père et fils*, 1822

[97] Dubi, Y. and Di Ventra, M.

Reconstructing Fourier's law from disorder in quantum wires.

*Physical Review B*, 79.11 (2009), 115415.

[98] Li B and Wang J.

Anomalous heat conduction and anomalous diffusion in one-dimensional systems.

*Physical review letters* 91.4 (2003), 044301.

[99] Rashidi-Huyeh, M., Volz, S. and Palpant, B.,

Non-Fourier heat transport in metal-dielectric core-shell nanoparticles under ultrafast laser pulse excitation.

*Physical Review B* 78.12 (2008), 125408.

[100] Zhang, X.P. and Bao, J.D.,

Anomalous heat conductivity induced by finite size and non-Markovian dynamics.

*Physical Review E*, 73.6 (2006), 061103.

[101] Chang, C.W., Okawa, D., Garcia, H., Majumdar, A. and Zettl, A.

Breakdown of Fourier's law in nanotube thermal conductors.

*Physical review letters* 101.7 (2008), 075903.

[102] Yang, N., Zhang, G. and Li, B.

Violation of Fourier's law and anomalous heat diffusion in silicon nanowires.

*Nano Today*, 5.2 (2010), 85-90.

[103] Hippalgaonkar, K., Huang, B., Chen, R., Sawyer, K., Ercius, P. and Majumdar, A.

Fabrication of microdevices with integrated nanowires for investigating low-dimensional phonon transport.

*Nano letters* 10.11 (2010), 4341-4348.

[104] Roh, J.W., Hippalgaonkar, K., Ham, J.H., Chen, R., Li, M.Z., Ercius, P., Majumdar, A., Kim, W. and Lee, W.

Observation of anisotropy in thermal conductivity of individual single-crystalline bismuth nanowires.

*Acs Nano* 5.5 (2011), 3954-3960.

[105] Bae, M.H., Li, Z., Aksamija, Z., Martin, P.N., Xiong, F., Ong, Z.Y., Knezevic, I. and Pop, E.

Ballistic to diffusive crossover of heat flow in graphene ribbons.

*Nature communications* 4 (2013), 1734.

[106] Wang, M., Yang, N. and Guo, Z.Y.

Non-Fourier heat conductions in nanomaterials.

*Journal of Applied Physics*, 110.6 (2011), 064310.

[107] Dubi, Y. and Di Ventra, M.

Fourier's law: Insight from a simple derivation.

*Physical Review E* 79.4 (2009), 042101.

[108] Incropera, F.P., Lavine, A.S., Bergman, T.L. and DeWitt, D.P.,

Fundamentals of heat and mass transfer.

*Wiley* (2007)

[109] Marín, E.

Characteristic dimensions for heat transfer.

*Latin-American Journal of Physics Education* 4.1 (2010), 56-60.

[110] Cahill, David G., and Robert O. Pohl.

Thermal conductivity of amorphous solids above the plateau.

*Physical review B* 35.8 (1987), 4067.

[111] Jain A. and Goodson K.E.

Measurement of the thermal conductivity and heat capacity of freestanding shape memory thin films using the $3\omega$ method.

*Journal of Heat Transfer*, 130.10 (2008), 102402.

[112] Sultan, R., Avery, A.D., Underwood, J.M., Mason, S.J., Bassett, D. and Zink, B.L.,

Heat transport by long mean free path vibrations in amorphous silicon nitride near room temperature.

*Physical review B*, 87.21 (2013), 214305.

[113] Kubota, Y., Watanabe, K., Tsuda, O., Taniguchi, T.,

Hexagonal Boron Nitride Single Crystal Growth at Atmospheric Pressure Using Ni-Cr Solvent.

*Chemistry of Materials* 20.5 (2008), 1661-1663.

[114] https://nanoscience.oxinst.com

[115] Birge, N.O., Dixon, P.K. and Menon, N.,
Specific heat spectroscopy: Origins, status and applications of the 3ω method.
*Thermochimica acta*, 304 (1997), 51-66.

[116] Geballe, T.H. and Giauque, W.F.,
The Heat Capacity and Entropy of Gold from 15 to 300 °K.
*Journal of the American Chemical Society*, 74.9 (1952), 2368-2369.

[117] Solozhenko et al., J.Phys.Chem. 61, 1480 (1987)

[118] Ftouni, H., Tainoff, D., Richard, J., Lulla, K., Guidi, J., Collin, E. and Bourgeois, O.,
Specific heat measurement of thin suspended SiN membrane from 8 K to 300 K using the 3ω-Volklein method.
*Review of Scientific Instruments*, 84.9 (2013), 094902.

[119] Kaestle, G., Boyen, H.G., Schroeder, A., Plettl, A. and Ziemann, P.
Size effect of the resistivity of thin epitaxial gold films.
*Physical Review B*, 70.16 (2004), p.165414.

[120] Sichel, E.K., Miller, R.E., Abrahams, M.S. and Buiocchi, C.J.,
Heat capacity and thermal conductivity of hexagonal pyrolytic boron nitride.
*Physical review B*, 13.10 (1976), 4607.

[121] Ftouni, H., Blanc, C., Tainoff, D., Fefferman, A.D., Defoort, M., Lulla, K.J., Richard, J., Collin, E. and Bourgeois, O.,
Thermal conductivity of silicon nitride membranes is not sensitive to stress.
*Physical Review B*, 92.12 (2015), 125439.

[122] Queen, D.R. and Hellman, F.,
Thin film nanocalorimeter for heat capacity measurements of 30 nm films.
*Review of Scientific Instruments*, 80.6 (2009), 063901.

[123] Bosak, A., Serrano, J., Krisch, M., Watanabe, K., Taniguchi, T. and Kanda, H.,
Elasticity of hexagonal boron nitride: Inelastic x-ray scattering measurements.
*Physical Review B*, 73.4 (2006), 041402.

[124] Mao, R., Kong, B.D., Gong, C., Xu, S., Jayasekera, T., Cho, K., Kim, K.W.,
First-principles calculation of thermal transport in metal/graphene systems.
*Physical Review B*, 87.16 (2013), 165410.

[125] Jauregui, L.A., Yue, Y., Sidorov, A.N., Hu, J., Yu, Q., Lopez, G., Jalilian, R., Benjamin, D.K., Delkd, D.A., Wu, W., Liu, Z.
Thermal transport in graphene nanostructures: Experiments and simulations.
*Ecs Transactions*, 28.5 (2010), 73-83.

[126] Dolleman, R.J., Houri, S., Davidovikj, D., Cartamil-Bueno, S.J., Blanter, Y.M., van der Zant, H.S., Steeneken, P.G.

Optomechanics for thermal characterization of suspended graphene.

*Physical Review B* 96.16 (2017), 165421.

[127] Dolleman, R.J., Blanter, Y.M., van der Zant, H.S., Steeneken, P.G., Verbiest, G.J.,

Phonon Scattering at Kinks in Suspended Graphene.

*arXiv preprint* (2019) arXiv: 1909.11615.

[128] Jaber, W., Chapuis, P.O.

Non-idealities in the 3 omega method for thermal characterization in the low- and high-frequency regimes.

*AIP Advances*, 8.4 (2018), 045111.

[129] Assael, M.J., Botsios, S., Gialou, K. and Metaxa, I.N.,

Thermal conductivity of polymethyl methacrylate (PMMA) and borosilicate crown glass BK7.

*International Journal of Thermophysics*, 26.5 (2005), 1595-1605.

[130] Schroeder, D.V.,

An introduction to thermal physics.

*Addison Wesley Longman* (2000)

[131] Kittel, Charles

Introduction to Solid State Physics.

*John Wiley & Sons* (2004)

[132] Wang, C., Guo, J., Dong, L., Aiyiti, A., Xu, X., Li, B.,

Superior thermal conductivity in suspended bilayer hexagonal boron nitride.

*Scientific reports*, 6 (2016), 25334.

[133] Lindsay, L. and Broido, D.A., 2012.

Theory of thermal transport in multilayer hexagonal boron nitride and nanotubes.

*Physical Review B* 85.3 (2012), 035436.

[134] McDonald, R.A. and Stull, D.R.,

The heat content and heat capacity of boron nitride from 298 to 1698 K.

*The Journal of Physical Chemistry*, 65.10 (1961), 1918.

[135] Ashcroft, N.W. and Mermin, N.D.,

Solid state physics

*Harcourt College Publishers* (1976)

[136] Lindsay, L. and Broido, D.A.,

Enhanced thermal conductivity and isotope effect in single-layer hexagonal boron nitride.

*Physical Review B* 84.15 (2011), p.155421.

[137] Jaeger, J.C. and Carslaw, H.S.,

Conduction of heat in solids.

*Clarendon P.* (1969), 64-70

[138] Zhang, X., Grigoropoulos, C.P.

Thermal conductivity and diffusivity of free-standing silicon nitride thin films.

*Review of scientific instruments* 66.2 (1995), 1115-1120.

[139] Morikawa, J. and Hashimoto, T.,

Analysis of high-order harmonics of temperature wave for Fourier transform thermal analysis.

*Japanese journal of applied physics*, 37.12A (1998), L1484.

[140] Morikawa, J., Hashimoto, T. and Maesono, A.,

Simultaneous measurement of thermal diffusivity, heat capacity, and thermal conductivity by Fourier transform thermal analysis.

*HIGH TEMPERATURES HIGH PRESSURES*, 33.4 (2001), 387-396.

[141] Maesono, A., Takasaki, Y., Maeda, Y., Tye, R.P., Morikawa, J. and Hashimoto, T., 2002.

A new apparatus for thermal diffusivity and specific heat measurements of films and liquids by means of Fourier transform thermal analysis.

*HIGH TEMPERATURES HIGH PRESSURES*, 34.2 (2002), 127-134.

[142] Morikawa, J., Tan, J. and Hashimoto, T.,

Study of change in thermal diffusivity of amorphous polymers during glass transition.

*Polymer*, 36.23 (1995), 4439-4443.

[143] Takahashi, F., Ito, K., Morikawa, J., Hashimoto, T. and Hatta, I.,

Characterization of heat conduction in a polymer film.

*Japanese journal of applied physics*, 43.10R (2004), 7200.

[144] Morikawa, J., Leong, C., Hashimoto, T., Ogawa, T., Urata, Y., Wada, S., Higuchi, M. and Takahashi, J.I.,

Thermal conductivity/diffusivity of Nd 3+ doped Gd VO 4, YVO 4, Lu VO 4, and Y 3 Al 5 O 12 by temperature wave analysis.

*Journal of Applied Physics*, 103.6 (2008), 063522.

[145] Morikawa, J. and Hashimoto, T.,

Thermal diffusivity of aromatic polyimide thin films by temperature wave analysis.

*Journal of Applied Physics*, 105.11 (2009), 113506.

[146] Bartsch, T., Schmidt, M., Heyn, C. and Hansen, W.,

Thermal conductance of ballistic point contacts.

*Physical review letters*, 108.7 (2012), 075901.

[147] Hook, J.R. and Hall, H.E.,
Solid state physics.
*John Wiley & Sons* (2013)